A MODEL FOR DISSIPATION OF SOLAR WIND TURBULENCE WITH DAMPING BY KINETIC ALFVÉN WAVES:

COMPARISON WITH OBSERVATIONS AND IMPLICATIONS FOR THE DISSIPATION PROCESS IN THE SOLAR WIND

INAUGURAL-DISSERTATION
ZUR
ERLANGUNG DES DOKTORGRADES
DER MATHEMATISCH-NATURWISSENSCHAFTLICHEN FAKULTÄT
DER UNIVERSITÄT ZU KÖLN

vorgelegt von
ANNE SCHREINER
aus Daun

Köln 2017

Berichterstatter: Prof. Dr. Joachim Saur

Prof. Dr. Yaping Shao

Tag der mündlichen Prüfung: 27. Juni 2017

Abstract

The aim of this work is to improve the characterization of small scale processes in the solar wind, particularly, the dissipation process of the turbulent energy. Although some statistical properties of solar wind turbulence are comparable to those of hydrodynamic turbulence, the presence of the interplanetary magnetic field and the composition of the solar wind of charged particles result in important differences. We present a dissipation model, which is based on a combination of the nonlinear energy transport from large to small scales and the damping process, which becomes important at small scales. We assume that damping is caused by interactions between kinetic Alfvén waves (KAW) and solar wind particles. The first part of this thesis presents a one-dimensional model in wavenumber space, which is compared with solar wind observations. With the help of this model, the following conclusions can be drawn about the dissipation process: assuming an anisotropic energy transport, which follows the critical balance theory, the background turbulence is driven by KAWs and not by whistler waves. This KAW driven cascade results in a quasi-exponentially shaped dissipation range and a dissipation length which corresponds to the electron gyroradius. The model provides an answer to the question as to why the dissipation length in the solar wind is independent of the energy injected at large scales, which is a clear difference compared to hydrodynamic turbulence. The anisotropic nature of the solar wind turbulence influences the transport of energy in such a way that the damping becomes more effective with a larger amount of injected energy. The expansion of the one-dimensional dissipation model to three dimensions and the thereon based calculation of reduced power spectra in the frequency space lead to the following conclusions: Damping due to KAW is able to explain the steep spectral index in the sub-ion range, which is observed in the solar wind plasma but could not be explained by any theory. However, a direct comparison with a set of solar wind observations shows that the spectral index is still steeper in the observations than the spectral index in the model. We conclude that the KAW driven cascade is present in all the observed spectra, but that other effects or wave modes can additionally influence the slope.

Zusammenfassung

Das Ziel dieser Arbeit ist es, die kleinskaligen Prozesse und insbesondere die Dissipation turbulenter Energie im Sonnenwind Plasma zu charakterisieren. Obwohl einige statistische Eigenschaften der Sonnenwind Turbulenz vergleichbar sind mit denen hydrodynamischer Turbulenz, resultieren die Anwesenheit des interplanetaren Magnetfeldes und die Zusammensetzung des Sonnenwindes aus geladenen Teilchen in deutlichen Unterschieden. Wir präsentieren ein Dissipationsmodell, welches auf einer Kombination aus nicht-linearem Energie Transport von großen zu kleinen Skalen und dem Dämpfungsprozess, der auf kleinen Skalen einsetzt, basiert. Es wird angenommen, dass die Dämpfung durch Interaktionen zwischen kinetischen Alfvén Wellen (KAW) und den Sonnenwind Teilchen hervorgerufen wird. Der erste Teil dieser Arbeit präsentiert ein eindimensionales Modell im Wellenzahl-Raum, welches mit Sonnenwind Beobachtungen verglichen wird. Mit Hilfe dieses Modells können folgende Rückschlüsse auf den Dissipationsprozess gezogen werden: Unter der Annahme eines anisotropen Enegietransports, welcher der Critical Balance Theorie folgt, wird die Hintergrund Turbulenz von KAW und nicht von Whistler Wellen getrieben. Diese KAW Kaskade resultiert in einem quasi-exponentiell geformten Dissipationsbereich und einer Dissipationslänge, die dem Elektronen Gyroradius entspricht. Das Modell gibt eine Antwort auf die Frage, warum die Dissipationslänge im Sonnenwind unabhängig von der Energie ist, die auf großen Skalen injiziert wird, was einen deutlichen Unterschied im Vergleich zu hydrodynamischer Turbulenz darstellt. Die anisotrope Natur der Sonnenwind Turbulenz beeinflusst den Energietransport in der Art, dass bei einer größeren Menge an injizierter Energie die Dämpfung effektiver wird. Die Erweiterung des eindimensionalen Dissipationsmodells auf drei Dimensionen und die darauf basierende Berechnung reduzierter Energiespektren im Frequenz-Raum führt zu folgenden Rückschlüssen: Die Dämpfung aufgrund von KAW ist in der Lage, den steilen spektralen Index im Bereich zwischen Ionen und Elektronen Skalen zu erklären, welcher im Sonnenwind Plasma beobachtet wird, aber bisher durch keine Theorie erklärt werden konnte. Allerdings zeigt sich im direkten Vergleich mit einem Set aus Sonnenwind Beobachtungen, dass der spektrale Index in den Beobachtungen weiterhin steiler ist als der spektrale Index im Modell. Wir schließen daraus, dass die KAW getriebene Kaskade in allen beobachteten Spektren anwesend ist, dass allerdings andere Effekte oder Wellenmoden die Steigung zusätzlich beeinflussen können.

Contents

1 Introduction **1**

2 Turbulence Theory and Observations of Solar Wind Turbulence **7**

2.1 Hydrodynamic Turbulence and Dissipation 7
2.2 Turbulence and Dissipation in the Solar Wind Plasma 12
  2.2.1 MHD Description of Plasma Turbulence 12
  2.2.2 Dispersion Relation of Kinetic Alfvén Waves 16
  2.2.3 Observational Evidence of Turbulence and Associated Theories 20

3 One-Dimensional Dissipation Model in Wavenumber Space **37**

3.1 Idea and Derivation of the One-Dimensional Dissipation Model 37
3.2 Damping Rates of Kinetic Alfvén Waves 43
3.3 Theoretical Implications for the Solar Wind Dissipation Process . . . 46
3.4 Comparison with Solar Wind Observations 52
  3.4.1 Comparison with Exemplary Magnetic Power Spectrum 52
  3.4.2 Statistical Analysis 54
3.5 Discussion 56

4 Model for Reduced Power Spectra in Frequency Space **61**

4.1 Calculation of Reduced Power Spectra 61
4.2 Extension of One-Dimensional Dissipation Model to Three Dimensions 65
4.3 Comparison with Solar Wind Observations 72
  4.3.1 Data Set 72
  4.3.2 Calculation of Reduced Power Spectra 74
  4.3.3 Comparison with Exemplary Data Intervals and Analysis of the Spectral Index 76
4.4 Discussion 83

5 Summary and Conclusions **87**

A Appendix **91**
A.1 All 93 Observed Solar Wind Spectra 91
A.2 Modeled Power Spectral Densities for Different Energy Distributions . 103

List of Figures **105**

Bibliography **113**

1 Introduction

The word *turbulence* describes a phenomenon of fluid dynamics where eddies of all sizes interact nonlinearly with each other resulting in chaotic and unpredictable flows. Characteristic features of turbulent flows are a self-similar behavior of eddies at all scales, non predictable spatial temporal trajectories of single particles and extremely sensitive dependencies on initial and boundary conditions. A particular feature of turbulence is that it transports energy loss-free from large scales, where the energy is injected, up to the smallest scales, where dissipation becomes effective and transfers the energy into particle heating. Although turbulence can be observed and experienced in our every-day life going from the milk in your cup of coffee to large scale turbulence in the oceans and the Earth's atmosphere, a complete description of turbulence remains one of the unsolved problems in physics. The difficulty in predicting turbulent flows arises due to the fact that the Navier-Stokes equation, which is the governing equation of fluid motions, can not be solved in general but only for a few particular initial and boundary conditions. However, a statistical description of turbulence without prediction of single trajectories but statistical properties is able to help better understand the evolution of turbulence. The first statistical theory of turbulence was proposed by Andrey Kolmogorov in 1941 (Kolmogorov, 1941a,b,c,d). The two main concepts of this work are that the eddies interact only locally[1]and that the whole amount of injected energy at large scales will be dissipated into heat eventually at the dissipation scale. With the help of these two concepts in combination with scaling analysis, one can derive the characteristic scaling of the one-dimensional velocity power spectrum $E(k) \propto k^{-5/3}$, which is a universal feature of hydrodynamic turbulence.

The problem of describing turbulent flows gets even more complicated when we look at magnetized plasmas, which appear in astrophysical environments such as the interstellar medium, the solar wind, or planetary magnetospheres. In these environments, the presence of the magnetic field influences the turbulent flow enormously. The largest laboratory to study turbulence in magnetized plasmas based on in situ measurements of the magnetic and electric field and the plasma parameters that we have up to now is the solar wind. The solar wind is a steady stream of low density plasma released from the Sun's corona filling the whole interplanetary space up to the heliopause, which is the boundary of solar wind and the interstellar medium. The solar wind consists mainly of electrons, protons, and a smaller part of alpha particles and heavier ions. Since the first spacecrafts set out for their journey to the planets of our solar system in the early 1970s, in situ measurements of the solar wind took place and served as basis for the first studies of solar wind turbulence. It became clear that the solar wind develops turbulent features similar to hydrodynamic turbulence with the characteristic slope of -5/3 for magnetic fluctuations in the inertial range. Most studies back than and now analyze turbulent properties based on magnetic field fluctuations because the magnetic field can be measured with higher time resolution and higher accuracy compared to the other turbulent fields. Therefore, the theoretical description of solar wind turbulence in this thesis will also be restricted to magnetic field fluctuations.

---

[1] Note that the term 'local' refers to scales and not to positions.

Although magnetic fluctuations in the solar wind show, in a statistical sense, a similar behavior to hydrodynamic fluctuations, three main differences occur when looking at plasma turbulence. First, the solar wind consists of charged particles which bring different characteristic scales into the system such as the gyrofrequency, the gyroradius or the inertial length of both protons and electrons, whereas the dissipation scale is the only characteristic scale in a hydrodynamic flow. Second, fluctuations of the magnetic fields are dissipated by a different mechanism than the viscosity in hydrodynamic turbulence, namely the resistivity. Owing to the extremely low resistivity, and viscosity when looking at the velocity fluctuations, of the solar wind plasma, classical mechanisms for dissipation and heating are ruled out leading to the outstanding problem how the turbulent energy is dissipated in the solar wind. The third difference of solar wind turbulence is the presence of the magnetic field which establishes a preferred direction, which results in different dynamics in the parallel and perpendicular direction with respect to the magnetic field. In addition, the magnetic field with its magnetic pressure and magnetic tension gives rise to new wave modes, namely the magnetosonic waves and the Alfvén wave, respectively. The latter modifies the turbulent nature of plasma turbulence from interacting hydrodynamic eddies to interacting magnetohydrodynamic (MHD) waves. Together, the magnetic field and the Alfvénic nature of fluctuations result in the anisotropy of plasma turbulence, which implies that the turbulent energy is transferred more rapidly to smaller perpendicular scales than to smaller parallel scales.

However, despite these remarkable differences, the self-similar behavior of magnetic fluctuations in the inertial range indicates that the qualitative picture of plasma turbulence is comparable to that of hydrodynamic turbulence, at least at scales where the MHD approximation is valid. In the inertial range, the considered scales are much larger than the characteristic plasma length scales and the wave frequencies are much smaller than the characteristic frequencies; therefore, a fluid description in the framework of magnetohydrodynamics is possible. It is well established that nonlinear interactions of Alfvén waves lead to the formation of the turbulent energy cascade to smaller scales. In this MHD limit, the scales can be seen as the diameter of an eddy which interacts nonlinearly with other eddies, analogously to hydrodynamic turbulence. Thus, it is no surprise that magnetic field fluctuations show the same spectral index of $5/3$ as hydrodynamic spectra.

At scales comparable to the ion scales, namely the ion gyroradius and the ion inertial length, the MHD approximation breaks down and it becomes necessary to apply a kinetic description for the dynamics of the ions and electrons. These scales are usually referred to as the kinetic range of solar wind turbulence. In the past decade, high time resolution magnetic field measurements taken by spacecraft such as ACE, Cluster, or ARTEMIS led to a flurry of research activity to determine the characteristics of kinetic scale processes. But despite the growing number of observed data sets, there is still insufficient information to fully establish the properties of electron scale processes. Additionally, due to the requirement for a kinetic description at these scales, the interpretation of observations with the help of simulations and theoretical considerations remains particularly difficult. Therefore, a number of fundamental physical aspects of small-scale solar wind turbulence are still poorly understood. Improved characterization of these small-scale processes, especially the dissipation and heating mechanism, could give answers to outstanding questions such as how the solar corona is heated and how the solar wind is heated and accelerated.

A widely accepted picture of what happens to the turbulent energy at kinetic scales can be described as follows: When the energy reaches scales comparable to the ion gyroradius, the Alfvén wave undergoes a transition to the dispersive kinetic Alfvén wave (KAW), which generates another turbulent cascade down to the electron scales. In the vicinity of the electron gyroradius or the electron inertial length, the KAW is subject to strong Landau damping via wave-particle interactions (e.g., Howes et al., 2006; Schekochihin et al., 2009; Sahraoui et al., 2009). However, since the properties of the whistler wave, another prominent candidate for damping of turbulent fluctuations via wave-particle interactions, are similar to those of the KAW, it is difficult to distinguish these waves in observations. Hence, there is still an ongoing debate whether the small-scale fluctuations consist of whistler waves or KAWs. Another open question is whether the turbulent cascade and the dissipation mechanism is as universal as in hydrodynamic turbulence, where a flow with the same Reynolds number and the same amount of injected energy results in the same power spectrum and where the turbulent energy is dissipated at a universal dissipation scale. In the case of solar wind turbulence, one could speculate that the behavior of turbulent fluctuations depends strongly on the current plasma parameters. Please note that similar to common terminology in the literature, the term 'dissipation' refers in this thesis to the transfer of energy from the magnetic field into perturbations of the particle distribution function via wave–particle interactions. The final transfer of this non-thermal free energy in the distribution function to thermal energy, i.e., the irreversible thermodynamic heating of the plasma, can only be achieved by collisions (Schekochihin et al., 2009; Howes, 2015; Schekochihin et al., 2016).

In this thesis, we focus on the description and analysis of kinetic range turbulence, especially on the dissipation processes at the smallest observed scales, the electron scales. In order to constrain the underlying physical mechanism of dissipation, we present a one-dimensional 'quasi'-analytical dissipation model in wavenumber-space, which describes magnetic power spectra at kinetic scales. Our model combines the energy transport from large to small scales and collisionless damping, which removes energy from the magnetic fluctuations in the kinetic regime. We assume wave–particle interactions of kinetic Alfvén waves to be the main damping process.

Wave frequencies and damping rates of KAWs are obtained from the general hot plasma dispersion relation for waves in magnetized plasmas. A problem in comparing the one-dimensional spectrum in wavenumber space to observed power spectra arises when the field-to-flow angle between magnetic field and the solar wind direction is less than 90°. In this case different wavevectors map to the power spectrum at a certain frequency. To overcome this problem, we extend the one-dimensional model to three dimensions and use a forward modeling approach by von Papen & Saur (2015) to calculate reduced power spectra in frequency space, which can be compared directly with measurements. By doing so, we analyze the question whether KAW damping at electron scales can explain the sub-ion range of magnetic fluctuations, which is steeper than a theoretical description of KAW turbulence without damping predicts.

In order to create a theoretical basis for the studies in this thesis, we present relevant theories concerning solar wind turbulence and dissipation in more detail in Chapter 2. Additionally, linear theory of dispersion relations and the corresponding plasma wave modes will be presented. In Chapter 3, we describe the general idea and derivation of the one-dimensional dissipation model, show theoretical implications for the dissipation process that arise from our theoretical description, and compare the model to observed power spectra at electron scales. The results indicate that solar wind turbulence develops a universal character in a way that the electron gyroradius acts as a universal dissipation scale independently of the amount of injected energy at large scales, which is a remarkable difference compared to hydrodynamic turbulence. Part of this chapter has already been published in Schreiner & Saur (2017). In Chapter 4, we present the extension to three dimensions and the idea of the forward modeling approach, as well as comparisons of the reduced power spectra with a set of solar wind observations. In general, the sampling effect, which arises due to the mapping of different wavevectors to the power spectrum at one certain frequency, in combination with KAW damping is able to explain the steep spectral index in the sub-ion range. However, additional effects, such as intermittency and other wave modes might lead to additional steepening. Finally, in Chapter 5 we summarize our findings and discuss the limitations of our approach and the resultant implications for the solar wind dissipation process.

2 Turbulence Theory and Observations of Solar Wind Turbulence

In order to create a basis for the understanding of the main concepts of our dissipation model, we give a short introduction to hydrodynamic turbulence in the framework of Kolmogorov's phenomenology in the next section. Turning to solar wind turbulence, we present the theory of MHD turbulence, which shows that the concepts of hydrodynamic turbulence are in a sense transferable to plasma turbulence. Following, we introduce the concept of dispersion relations for the description of plasma waves, which play a main role in understanding the turbulent energy cascade as well as the the dissipation process in the solar wind plasma. The main part of this chapter gives an overview of solar wind observations and related theories concerning primarily the dissipation process of magnetic fluctuations. Finally, we summarize outstanding questions that arise from these observations and that create the prime motivation for the derivation of our dissipation model.

2.1 Hydrodynamic Turbulence and Dissipation

As was mentioned in the Introduction, the solar wind flow develops turbulent features similarly to hydrodynamic turbulent flows. Andrey Kolmogorov's 1941 theory has therefore been a widely used starting point for solar wind turbulence theory. As we will see in Chapter 3 and 4, Kolmogorov's theory on the energy cascade process and the associated dissipation scale is also one of the basis concepts in our solar wind dissipation model. On this account, we present a phenomenological description of turbulence and dissipation based on Kolmogorov's 1941 theory in this section.

The underlying equation for the description of motions of viscous fluid substances is the Navier-Stokes equation, which principally allows a mathematical description of turbulent motions. The Navier-Stokes equation for an incompressible fluid can be written as

$$\frac{\partial \mathbf{v}}{\partial t} + \mathbf{v} \cdot \nabla \mathbf{v} = -\frac{1}{\rho} \nabla p + \nu \Delta \mathbf{v} + \mathbf{F}, \tag{2.1}$$

$$\nabla \cdot \mathbf{v} = 0, \tag{2.2}$$

where $\mathbf{v}$ defines the fluid velocity, ρ the mass density, p the pressure, ν the kinematic viscosity, and $\mathbf{F}$ external forces. Here and in all following equations, upright boldface letters represent vector quantities. On the basis of the Navier-Stokes equation, a dimensionless quantity to characterize a turbulent flow, the Reynolds number R_e, can be estimated by the ratio of the nonlinear term $\mathbf{v} \cdot \nabla \mathbf{v}$ to the viscous term $\nu \Delta \mathbf{v}$,

$$R_e = \frac{\mathbf{v} \cdot \nabla \mathbf{v}}{\nu \Delta \mathbf{v}} \sim \frac{LV}{\nu}, \tag{2.3}$$

where L and V represent a characteristic length scale and a characteristic velocity, respectively. For similar Reynolds numbers, two flows behave in a similar way independently of the actual size or velocity of the fluid. For small Reynolds numbers, a laminar flow occurs with a smooth and constant fluid motion. With increasing Reynolds numbers, eddies start to form, and symmetries that are given by the Navier-Stokes equation start to break. In this thesis, we will consider only high Reynolds number flows ($R_e \gg 1000$), where the symmetries are restored in a statistical sense, which is known as fully developed turbulence.

Up to now, it has not been possible to derive a complete turbulence theory based on the Navier-Stokes equation in a deductive way. Therefore, a phenomenological theory is frequently applied to predict statistical properties of fully developed turbulence. Lewis Fry Richardson was one of the early pioneers in this research area who introduced the modern concept of an energy cascade from large to small scales and its dissipation at the smallest scales for the first time (Richardson, 1922). This idea of energy transport is called Richardson cascade, which is illustrated schematically in Figure 2.1. Here, l_0 is the characteristic length scale or outer scale of the system, as it is often referred to in plasma turbulence theory, and η the dissipation scale. With the help of these characteristic scales, the scales of the turbulent process can be

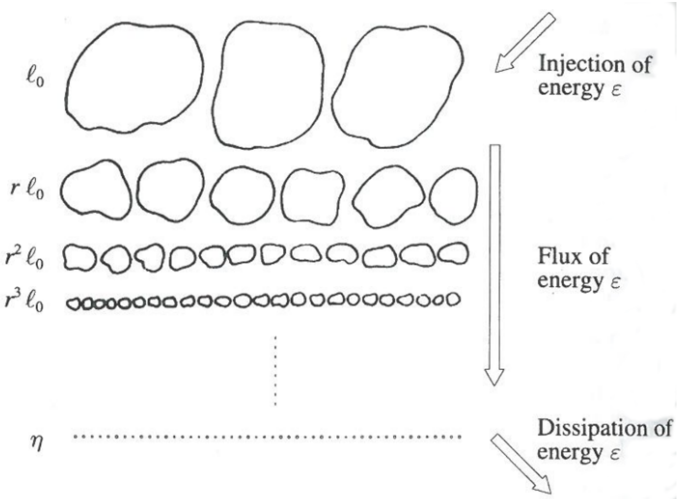
ℓ_0
$r\,\ell_0$
$r^2\,\ell_0$
$r^3\,\ell_0$
η
Injection of energy ε
Flux of energy ε
Dissipation of energy ε

Figure 2.1: Richardson cascade of hydrodynamic turbulence. The energy is transported from large scales/large eddies to the smaller ones. Figure from Frisch (1995) p. 104. Reproduced by permission of the Camebridge University Press.

divided into three ranges: First, the energy injection range for scales $l \sim l_0$, where energy is injected into the system, e.g., by an obstacle in the flow.[2] Second, the inertial range on scales l with $l_0 \gg l \gg \eta$, where the energy is transported loss-free from large to small scales; and third, the dissipation range for scales $l \sim \eta$, where dissipation due to viscosity becomes effective and the turbulent energy is converted to heat.

Based on Richardson's ideas of energy transport, Kolmogorov developed his famous 1941 phenomenological theory. This theory is presented here very briefly following Frisch (1995), who revisited Kolmogorov's theory in the light of newly developed theories and observations. The schematic picture of energy transport shown in Figure 2.1 brings out the two main assumptions of Kolmogorov's phenomenology: First, the self-similarity of eddies at all scales within the inertial range. One example of phenomenon in turbulent motions which is not self-similar is intermittency, which would result in eddies that are less and less space-filling with decreasing scale. Second, the localness of interactions which implies that only eddies of similar size interact with each other. Under these assumptions, Kolmogorov's 1941 theory can be described as follows. At the energy injection scale l_0, eddies with diameter $d \sim l_0$ are generated and start to decompose into smaller eddies. Eddies at scale l, with l between the injection scale l_0 and the dissipation scale η, have a characteristic velocity v_l, which is defined as the root-mean-square (rms) value of the velocity in a bandpass filtered interval around the wavenumber l^{-1}. The time, in which an eddy of size l undergoes a significant distortion, or in simple terms, in which one eddy decomposes into two smaller eddies, is referred to as the 'eddy turnover time',

---

[2] Within this phenomenological description and in the remainder of this thesis, the symbol $\sim$ means equal apart from constant factors on the order of unity.

$$t_l \sim \frac{l}{v_l}. \tag{2.4}$$

In the picture of eddy decomposition, t_l is also the time in which the energy is transferred from one scale to the next smaller one. Therefore, the energy flux Π_l from one scale l to smaller scales can be estimated by

$$\Pi_l \sim \frac{v_l^2}{t_l} \sim \varepsilon. \tag{2.5}$$

Owing to the constant flux of energy without direct energy injection or dissipation in the inertial range, the energy flux is independent of scale l and equal to the mean energy dissipation rate ε. Insertion of (2.4) into (2.5) results in

$$v_l \sim \varepsilon^{1/3} l^{1/3}. \tag{2.6}$$

The one-dimensional power spectrum $E_k(k)$ as a function of the wavenumber $k \sim l^{-1}$ is related to the mean kinetic energy $1/2\langle v^2 \rangle$ via

$$\frac{1}{2}\langle v^2 \rangle = \int_0^\infty E_k(k) \mathrm{d}k. \tag{2.7}$$

With (2.6) and dimensional analysis of (2.7), the power spectrum can be written as

$$E_k(k) \sim \varepsilon^{2/3} k^{-5/3}. \tag{2.8}$$

Relation (2.8) reveals that the power spectrum follows a power-law $k^{-\kappa}$ with a characteristic spectral index $\kappa = 5/3$, which is often referred to as the Kolmogorov spectral index. The existence of this power-law in the inertial range has been widely confirmed by observations and simulations (Frisch, 1995, and references within). A more general form of relation (2.8), which describes both the inertial range and the dissipation range, is given by

$$E_k(k) \sim \varepsilon^{2/3} k^{-5/3} F(\eta k), \tag{2.9}$$

where $F(\cdot)$ is a universal dimensionless function of a dimensionless argument that tends towards the Kolmogorov constant C_K for small wavenumbers and becomes effective when $\eta k \sim 1$. A review on different approaches to determine the functional form of $F(\cdot)$ can be found in Monin & Yaglom (1975). Kolmogorov postulated in his first hypothesis of similarity that the statistical properties of small scales are uniquely and universally determined by the kinematic viscosity ν, the mean energy dissipation rate ε and the scale l. On the basis of this hypothesis in combination with dimensional analysis, the characteristic Kolmogorov dissipation scale,

$$\eta = \left(\frac{\nu^3}{\varepsilon}\right)^{1/4} \tag{2.10}$$

can be derived. The dissipation scale marks the end of the inertial range, in which energy dissipation is negligible. For scales smaller than the dissipation scale, the energy input at scale l due to nonlinear interactions and the energy drain due to viscous dissipation are equal. At these scales, the turbulent energy is converted to particle heat via collisions. The presented picture of turbulent energy transport is based on the idea of decaying eddies, which transport the energy from large to small scales until the viscosity becomes effective. The next section deals with the question to what extend these ideas can be transferred to the solar wind plasma with its low viscosity and resistivity.

2.2 Turbulence and Dissipation in the Solar Wind Plasma

In the following, we present an introduction to the theory of MHD turbulence, which results in the equation of motion for a magnetized plasma in terms of Elsässer variables. Leaving the MHD framework, we describe the concept of dispersion relations for plasma waves, especially the kinetic Alfvén wave, which we assume to generate turbulence in the kinetic regime. Based on these theoretical descriptions, we give an overview of solar wind observations concerning kinetic scale turbulence and the dissipation process and theories that arise from these observations.

2.2.1 MHD Description of Plasma Turbulence

As mentioned in the previous section, hydrodynamic, i.e., non-magnetized fluids, are known to be in a fully developed turbulent state for sufficiently high Reynolds numbers R_e. For a magnetized plasma, e.g., the solar wind, one can derive an analogous dimensionless quantity, the magnetic Reynolds number R_m, to characterize the turbulent flow. In the following, we derive the general induction equation for the magnetic field, which we use to define the magnetic Reynolds number in a similar way as was done for the hydrodynamic Reynolds number. Combining the induction equation with the MHD equation of motion leads to an equation which is in its form similar to the Navier-Stokes equation for hydrodynamic flows.

A plasma is a gas consisting of charged particles with a quasi-neutral behavior; i.e, on average, a plasma looks electrically neutral to the outside. This quasi-neutrality is a result of having roughly the same number of positive and negative charges in a plasma. Due to their electrical charges, the particles in a plasma are coupled to the electromagnetic field, i.e, their motion is affected by the electromagnetic field. The influence of the electric field **E** and the magnetic field **B** on the particle motion and vice versa is described by Maxwell's equations,

$$\nabla \times \mathbf{B} = \mu_0 \mathbf{j} + \epsilon_0 \mu_0 \frac{\partial \mathbf{E}}{\partial t}, \tag{2.11}$$

$$\nabla \times \mathbf{E} = -\frac{\partial \mathbf{B}}{\partial t}, \tag{2.12}$$

$$\nabla \cdot \mathbf{B} = 0, \tag{2.13}$$

$$\nabla \cdot \mathbf{E} = \frac{\rho_c}{\epsilon_0}, \tag{2.14}$$

where $\mathbf{j} = e(n_i \mathbf{v}_i - n_e \mathbf{v}_e)$ is the electric current and $\rho_c = e(n_i - n_e)$ the electric charge density for singly charged ions with electron and ion number densities and velocities n_s and $\mathbf{v}_s$, respectively[3]. e defines the electron charge, and ϵ_0 and μ_0 are the vacuum permittivity and susceptibility, respectively. Starting with Faraday's law in (2.12), and eliminating the electric field by insertion of the generalized Ohm's law,

$$\mathbf{j} = \sigma_0(\mathbf{E} + \mathbf{v} \times \mathbf{B}) \tag{2.15}$$

leads to

$$\frac{\partial \mathbf{B}}{\partial t} = \nabla \times (\mathbf{v} \times \mathbf{B} - \frac{\mathbf{j}}{\sigma_0}), \tag{2.16}$$

with the plasma conductivity

$$\sigma_0 = \frac{n_e e^2}{m_e \nu_c}. \tag{2.17}$$

Here, m_e is the electron mass and ν_c is the collision frequency of Coulomb or neutral collisions. The displacement current $\epsilon_0 \mu_0 \partial \mathbf{E}/\partial t$ in Ampère's law in (2.11) can be dropped for slow oscillating electric fields, which is a valid assumption in a plasma as long as we do not consider electromagnetic waves. Using Ampère's law without displacement current and $\nabla \cdot \mathbf{B} = 0$, one obtains the general induction equation for the magnetic field

$$\frac{\partial \mathbf{B}}{\partial t} = \nabla \times (\mathbf{v} \times \mathbf{B}) + \frac{1}{\mu_0 \sigma_0} \Delta \mathbf{B}. \tag{2.18}$$

Thus, the magnetic field can be changed either by motion of the plasma with velocity $\mathbf{v}$ (first term on right hand side) or by diffusion (second term on right hand side). Similarly to the hydrodynamic Reynolds number, the magnetic Reynolds number is defined as the ratio of the convection term $\nabla \times (\mathbf{v} \times \mathbf{B})$ to the diffusion term $(\mu_0 \sigma_0)^{-1} \Delta \mathbf{B}$. In simple dimensional form, the magnetic Reynolds number R_m can be written as

$$R_m = \mu_0 \sigma_0 L V = \frac{LV}{\eta_m}, \tag{2.19}$$

---

[3] Subscript s stands for different species, i.e., ions or electrons.

with $\eta_m = (\mu_0 \sigma_0)^{-1}$ being the magnetic diffusivity, and L and V again characteristic length scales and velocities, respectively. For $R_m \gg 1$, the diffusion term in the induction equation can be neglected and the magnetic field is frozen-in into the flow, i.e., it moves together with the flow. Only in high magnetic Reynolds number plasma flows, turbulence is generated. For $R_m \sim 1$, diffusion starts to become important and the magnetic field is no longer frozen-in into the plasma. Similar to a large viscosity in a hydrodynamic flow, a large diffusivity smooths out any local magnetic inhomogeneity resulting in a non-turbulent magnetic field. In the solar wind plasma, the magnetic Reynolds number is about $R_m \approx 7 \times 10^{16}$ (Frisch, 1995); therefore, the assumption of fully developed turbulence should be valid at least at sufficiently large distances to the Sun ($\sim 0.3\,\mathrm{AU}$).

Due to the coupling of charged particles to the electromagnetic field, the Lorentz force

$$\mathbf{F} = q(\mathbf{E} + \mathbf{v} \times \mathbf{B}), \tag{2.20}$$

with particle charge q has to be taken into account in the equation of motion

$$\frac{\partial \mathbf{v}}{\partial t} + \mathbf{v} \cdot \nabla \mathbf{v} = -\frac{1}{\rho} \nabla p + \nu \Delta \mathbf{v} + \frac{q}{\rho}(\mathbf{E} + \mathbf{v} \times \mathbf{B}). \tag{2.21}$$

Adding up Equation (2.21) for ions and electrons with number density n_s, mass m_s, thermal pressure p_s and velocity $\mathbf{v}_s$, and applying a single fluid description ($n = n_i = n_e$, $\rho = n(m_e + m_i)$, $p = p_i + p_e$, $\mathbf{v} = (m_i \mathbf{v}_i + m_e \mathbf{v}_e)/(m_i + m_e)$), one obtains the MHD equation of motion for an incompressible plasma,

$$\frac{\partial \mathbf{v}}{\partial t} + \mathbf{v} \cdot \nabla \mathbf{v} = -\frac{1}{\rho} \nabla p + \nu \Delta \mathbf{v} + \frac{1}{\rho} \mathbf{j} \times \mathbf{B}, \tag{2.22}$$

$$\nabla \cdot \mathbf{v} = 0. \tag{2.23}$$

Within the MHD framework, the plasma is described as a single fluid, in which the dynamics of electrons and ions do not decouple. Hence, the MHD picture is valid for frequencies that are much smaller than the gyrofrequencies $\Omega_s = q_s B_0 / m_s$ of ions and electrons, and for scales that are much larger than the ion and electron gyroradius $\rho_s = v_s / \Omega_s$. B_0 is the mean magnetic field and $v_s = \sqrt{2 k_B T_s / m_s}$ the thermal velocity of species s with the Boltzmann constant k_B and temperature T_s.

For slow variations, i.e., when the displacement current in Ampère's law in (2.11) can be neglected, the Lorentz force term $\mathbf{j} \times \mathbf{B}$ can be written as

$$\mathbf{j} \times \mathbf{B} = -\nabla \left(\frac{B^2}{2\mu_0} \right) + \frac{1}{\mu_0} (\mathbf{B} \cdot \nabla) \mathbf{B}, \tag{2.24}$$

where the first term describes the magnetic pressure $p_B = B^2/2\mu_0$, which simply adds to the thermal pressure, and the second term describes the magnetic tension. By separating the magnetic field $\mathbf{B} = \mathbf{B}_0 + \mathbf{b}$ into the background component $\mathbf{B_0}$ and fluctuations $\mathbf{b}$, and introducing the Elsässer variables $\mathbf{z}^{\pm} = \mathbf{v} \pm \mathbf{b}/\sqrt{\mu_0 \rho}$ (first introduced by Elsässer (1950)), the equation of motion in terms of Elsässer variables can be obtained by adding up (2.18) and (2.22) with the Lorentz force term as written in (2.24),

$$\frac{\partial \mathbf{z}^{\pm}}{\partial t} \mp (\mathbf{v}_A \cdot \nabla) \mathbf{z}^{\pm} + (\mathbf{z}^{\mp} \cdot \nabla) \mathbf{z}^{\pm} = -\frac{1}{\rho} \nabla P + \frac{1}{2} (\nu + \eta_m) \Delta \mathbf{z}^{\pm} + \frac{1}{2} (\nu - \eta_m) \Delta \mathbf{z}^{\mp}. \tag{2.25}$$

$\mathbf{v}_A = \mathbf{B_0}/\sqrt{\mu_0 \rho}$ defines the Alfvén velocity and $\nabla P = \nabla p + \nabla p_B$ is the sum of thermal and magnetic pressure. Equation (2.25) reveals two important implications: First, if the Elsässer variables are defined in a way that $\mathbf{z}^{+}$ refers to outgoing waves and $\mathbf{z}^{-}$ to ingoing waves, the nonlinear term $(\mathbf{z}^{\mp} \cdot \nabla) \mathbf{z}^{\pm}$ is only effective for oppositely propagating Alfvén wave packets. Second, the equation of motion for Elsässer variables is in its form similar to the hydrodynamic Navier-Stokes equation indicating that similar assumptions concerning the cascade and dissipation process as shown in Section 2.1 can be made in the solar wind. However, the question remains how the turbulent fluctuations are dissipated in the low viscosity and low resistivity solar wind plasma. A mechanism for dissipation that is commonly presented in the literature is damping by wave-particle interactions, by which energy can be transferred from the turbulent fluctuations into perturbations of the particle distribution function leading eventually to particle heating. These wave-particle interactions can be described within the framework of kinetic dispersion relations. Owing to the non-dispersive propagation of MHD plasma waves, dissipation processes can not be described within the framework of MHD, but a kinetic description is needed. In the next section, we present the general kinetic dispersion relation of plasma waves with special attention to kinetic Alfvén waves, which we assume to transport the energy in the kinetic regime from large to small scales.

2.2.2 Dispersion Relation of Kinetic Alfvén Waves

For the derivation of the general dispersion relation, it is necessary to express the plasma current in terms of the electric field. One way to do so is to introduce a dielectric tensor $\boldsymbol{\epsilon}$. In the following, we linearize Maxwell's equations by assuming $\mathbf{B} = \mathbf{B}_0 + \delta\mathbf{B}$, $\mathbf{E} = \mathbf{E}_0 + \delta\mathbf{E}$ with $\mathbf{B}_0 = \text{const.}$ and $\mathbf{E}_0 = 0$. The first order quantities are assumed to vary as $\exp[\mathrm{i}(\mathbf{k}\cdot\mathbf{r} - \omega t)]$ with position vector $\mathbf{r}$ and frequency ω. The symbol δ for first order quantities is dropped in the following derivation. According to the first of Maxwell's equations in (2.11), the electric displacement $\mathbf{D}$ consists of the vacuum displacement plus the plasma current

$$\nabla \times \mathbf{B} = \mu_0 \mathbf{j} + \epsilon_0 \mu_0 \frac{\partial \mathbf{E}}{\partial t} = \epsilon_0 \mu_0 \frac{\partial \mathbf{D}}{\partial t}. \tag{2.26}$$

Fourier transformation in time and space of (2.26) leads to

$$\mathbf{D}(\omega, \mathbf{k}) = \mathbf{E}(\omega, \mathbf{k}) + \frac{\mathrm{i}}{\epsilon_0 \omega} \mathbf{j}(\omega, \mathbf{k}) = \boldsymbol{\epsilon}(\omega, \mathbf{k}) \cdot \mathbf{E}(\omega, \mathbf{k}), \tag{2.27}$$

with the dielectric tensor $\boldsymbol{\epsilon}(\omega, \mathbf{k})$. Together with the Fourier transformed Faraday's law (2.12)

$$\mathbf{B} = \frac{1}{\omega} \mathbf{k} \times \mathbf{E}, \tag{2.28}$$

(2.26) can be written as

$$\mathbf{k} \times (\mathbf{k} \times \mathbf{E}) + \frac{\omega^2}{c^2} \boldsymbol{\epsilon} \cdot \mathbf{E} = 0, \tag{2.29}$$

where $c^2 = (\epsilon_0 \mu_0)^{-1}$ defines the speed of light. After some vector algebra, the general dispersion relation for waves in a hot plasma

$$\left[\mathbf{k} \otimes \mathbf{k} - k^2 \mathbb{1} + \frac{\omega^2}{c^2} \boldsymbol{\epsilon}\right] \cdot \mathbf{E} = 0, \tag{2.30}$$

is found, which has only non-trivial solutions for

$$\det\left[\mathbf{k}\otimes\mathbf{k}-k^2\mathbb{1}+\frac{\omega^2}{c^2}\boldsymbol{\epsilon}\right]=0. \tag{2.31}$$

$\mathbb{1}$ denotes the identity matrix and $\otimes$ the tensor product. Assuming that the wavevector is in the xz plane, the dispersion relation can be written in the form

$$\det\begin{pmatrix}\epsilon_{xx}-n_{\|}^2 & \epsilon_{xy} & \epsilon_{xz}+n_{\|}n_{\perp}\\ -\epsilon_{xy} & \epsilon_{yy}-n^2 & \epsilon_{yz}\\ \epsilon_{xz}+n_{\|}n_{\perp} & -\epsilon_{yz} & \epsilon_{zz}-n_{\perp}^2\end{pmatrix}=0, \tag{2.32}$$

with the parallel, perpendicular and total index of refraction $n_{\|}=k_{\|}c/\omega$, $n_{\perp}=k_{\perp}c/\omega$ and $n=k\omega/c$, respectively, where $k_{\|}$ is the parallel wavenumber and $k_{\perp}$ the perpendicular wavenumber with respect to the mean magnetic field. Equation (2.31) describes in general the propagation of linear waves with frequency $\omega=\omega(\mathbf{k})$. To determine the solution of (2.31), one must first find the dielectric tensor $\boldsymbol{\epsilon}$.

The most general way to obtain $\boldsymbol{\epsilon}$ is to make use of kinetic plasma theory. The kinetic theory describes the properties of the particle distribution function and its evolution. Hence, a kinetic description takes into account kinetic effects that are carried by single plasma components, such as gyromotions of electrons and ions. The set of fluid equations for mass, momentum and energy conservation have to be replaced by the set of Vlasov equations for every plasma component. The Vlasov equation describes the evolution of the distribution function f in a collisionless plasma according to

$$\frac{\partial f}{\partial t}+\mathbf{v}\frac{\partial f}{\partial \mathbf{x}}+\frac{q}{m}(\mathbf{E}+\mathbf{v}\times\mathbf{B})\frac{\partial f}{\partial \mathbf{v}}=0. \tag{2.33}$$

Starting from the linearization of the Vlasov equation, one can obtain the tensor elements of the dielectric tensor. The equation set of general dispersion relation and dielectric tensor obtained from the Vlasov equation is therefore often referred to as the linear Maxwell-Vlasov system. The derivation of the tensor elements involves a lengthy calculation, which we do not show here, but which can be found in Stix (1992). The tensor elements for a nonrelativistic plasma with Maxwellian distributed electrons and protons with no zero-order drift velocities can be cast in the form (e.g., Chen, 1974; Stix, 1992; Baumjohann & Treumann, 2012)

$$\begin{aligned}
\epsilon_{xx} &= 1+\sum_s \frac{\omega_{ps}^2}{\omega^2}\xi_{0s}\sum_{n=-\infty}^{\infty} n^2\frac{\Gamma_n(\mu_s)}{\mu_s}Z(\xi_{ns}), && (2.34)\\
\epsilon_{yy} &= 1+\sum_s \frac{\omega_{ps}^2}{\omega^2}\xi_{0s}\sum_{n=-\infty}^{\infty}\left\{n^2\frac{\Gamma_n(\mu_s)}{\mu_s}-2\mu_s\Gamma_n'(\mu_s)\right\}Z(\xi_{ns}), && (2.35)\\
\epsilon_{zz} &= 1-\sum_s \frac{\omega_{ps}^2}{\omega^2}\xi_{0s}\sum_{n=-\infty}^{\infty}\xi_{ns}\Gamma_n(\mu_s)Z'(\xi_n s), && (2.36)\\
\epsilon_{xy} &= i\sum_s \frac{\omega_{ps}^2}{\omega^2}\xi_{0s}\sum_{n=-\infty}^{\infty}\Gamma_n'(\mu_s)nZ(\xi_{ns}), && (2.37)\\
\epsilon_{xz} &= -\sum_s \operatorname{sgn}(q_s)\frac{\omega_{ps}^2}{\omega^2}\xi_{0s}\sum_{n=-\infty}^{\infty}\frac{1}{\sqrt{2\mu_s}}n\Gamma_n(\mu_s)Z'(\xi_{ns}), && (2.38)\\
\epsilon_{yz} &= i\sum_s \operatorname{sgn}(q_s)\frac{\omega_{ps}^2}{\omega^2}\xi_{0s}\sum_{n=-\infty}^{\infty}\Gamma_n'(\mu_s)Z'(\xi_{ns})\sqrt{\frac{\mu_s}{2}}, && (2.39)
\end{aligned}$$

where $\omega_{ps}=(n_s q_s^2/\epsilon_0 m_s)^{1/2}$ is the plasma frequency of species s, $\Omega_s=q_sB/m_s$ is the gyrofrequency of species s (negative for electrons), $\xi_{ns}=(\omega-n\Omega_s)/k_{\|}v_s$, $v_s=(2k_BT_s/m_s)^{1/2}$ is the thermal speed of species s, and $\mu_s=0.5k_\perp^2\rho_s^2$ with the gyroradius $\rho_s=v_s/\Omega_s$. The function $Z(\xi)$ is the plasma dispersion function, which was introduced by Fried & Conte (1961). Its derivative is given by $Z'(\xi)=-2-2\xi Z(\xi)$. $\Gamma_n(\mu_s)=e^{-\mu_s}I_n(\mu_s)$, where I_n is the modified Bessel function of the first kind of order n. Note that the derivative of Γ_n is given by $\Gamma_n'(\mu_s)=\left(I_n'(\mu_s)-I_n(\mu_s)\right)e^{-\mu_s}$.

After insertion of the dielectric tensor into the general dispersion relation (2.31), one can obtain the wave frequency as a complex number $\omega=\omega_r+\mathrm{i}\gamma$, where ω_r describes the dispersion of the wave mode and γ its damping. The validity of applying linear theory of dispersion relations to the nonlinear turbulent energy transport is discussed in the discussion part of Chapter 3. In the limits of MHD, wave frequencies of plasma waves do not have an imaginary part. Hence, only kinetic waves can be responsible for damping of turbulent fluctuations. The most prominent candidates for damping presented in the literature are kinetic Alfvén waves and whistler waves, which are both extensions of the MHD Alfvén wave with dispersion relation

$\omega_A = \pm k_{\parallel} v_A$ into the kinetic regime. The difference of KAW and whistler waves is

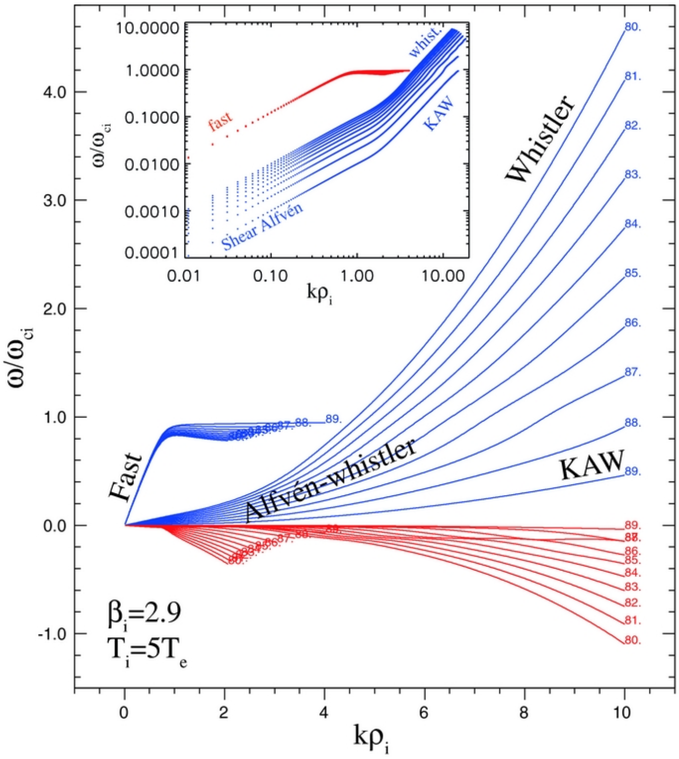

Figure 2.2: Solution ω/Ω_i of linear Maxwell-Vlasov equations as a function of $k\rho_i$: Real part of wave frequency is shown in blue, damping rate γ in red for different angles of propagation $\theta_{\mathbf{kB}}$. The inset shows the same plot with double-logarithmic axes to illustrate the transition from non-dispersive to kinetic regime at wavenumbers $\sim k\rho_i = 1$. Figure from Sahraoui et al. (2012). Reproduced by permission of the American Astronomical Society.

shown in Figure 2.2. KAWs propagate at quasi-perpendicular propagation angles $\theta_{\mathbf{kB}}$ with frequencies $\omega_{\mathrm{KAW}} < \Omega_i$, whereas whistler waves are defined as the extension of Alfvén waves with $\omega_w \geq \Omega_i$. As we will show in Chapter 3, wave frequencies in the solar wind under the assumption of critical balance (a model for the anisotropy of energy transfer in the solar wind with respect to the magnetic field, which is introduced in Section 2.2.3) do not exceed the ion gyrofrequency. Therefore, we refer to the solution of the general dispersion relation in our model as KAWs. Extensions of the MHD magnetosonic modes into the kinetic regime are not considered to carry the energy down to the scales of dissipation, i.e., the electron scales, because the slow magnetosonic mode is heavily damped at ion scales and the fast magnetosonic mode undergoes resonances at the ion gyrofrequency (Sahraoui et al., 2012). Against this background, we present observations of power spectral densities of magnetic fluctuations in the solar wind and associated theoretical descriptions in the following section.

2.2.3 Observational Evidence of Turbulence and Associated Theories

In the following, we present observations of magnetic power spectra in the solar wind going from observations at MHD and sub-ion scales to observations at electron scales. On the basis of these observations, the differences of whistler wave and KAW turbulence are introduced, as well as the concept of a critically balanced energy cascade.

Observations from MHD to Sub-Ion Scales

Owing to the extremely high (magnetic) Reynolds numbers of the solar wind plasma at 1 AU, the turbulence is assumed to be highly developed. This turbulent state of fluctuations is evidenced by magnetic field measurements, which show very broadband power spectral densities $P(f)$ or $P(k)$ illustrating the amount of energy per frequency or wavenumber, respectively (e.g., Coleman JR., 1968). This indication of the turbulent cascade is shown in Figure 2.3. We focus in this section on the magnetic power spectral density because it is the focal point of most solar wind turbulent studies, and it gives a simple overview of the scales of interest and the associated physical mechanism. Due to the high speed of the solar wind flow larger than most of the dynamics of the system, Taylor's hypothesis (Taylor, 1938) can be applied to relate temporal and spatial scales via $f = k_\perp v_{SW}/2\pi$ with the solar wind velocity v_{SW}. The time series measured by the spacecraft therefore corresponds to one-dimensional spatial measurements along a straight line in the plasma frame. As is shown in Chapter 4, this relation is valid only for measurements with high angles between the magnetic field and the solar wind flow direction $\theta_{\mathbf{vB}}$. For solar wind measurements close to Earth, where measurements with field-to-flow angles $\theta_{\mathbf{vB}}$ of

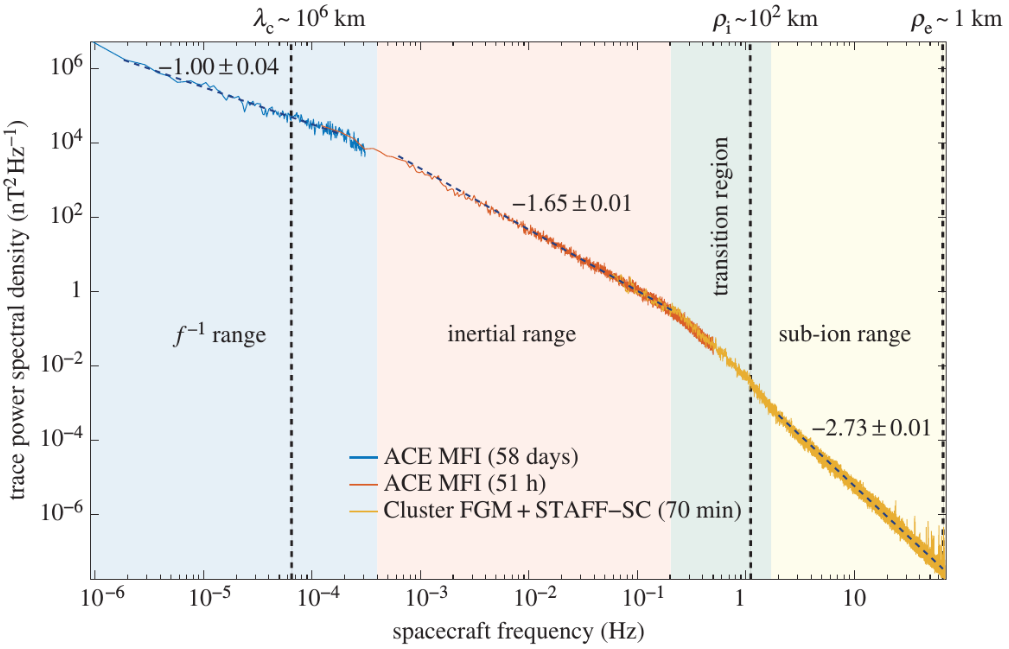

Figure 2.3: Power spectral density of the magnetic field fluctuations for typical solar wind parameters at 1 AU. Blue and red lines are calculated from ACE measurements; yellow line from Cluster measurements. Instruments and interval lengths are given in the legend. The vertical dashed lines indicate the correlation length λ_c, the ion gyroradius ρ_i, and the electron gyroradius ρ_e. Figure from Kiyani et al. (2015). Reproduced by permission of the Royal Society.

less than 50° are often related to the Earth's foreshock, and therefore not considered in the analysis of solar wind turbulence, this assumption is sufficiently fulfilled.

In Figure 2.3, four distinct regions of interest are marked by different background colors: the f^{-1} range, the inertial range, the transition region at ion scales, and the sub-ion range. In the f^{-1} range, the temporal variability of the Sun and its corona, the source of the solar wind, is visible (Matthaeus & Goldstein, 1986). This connection to the Sun breaks down for scales smaller (frequencies higher) than the correlation length λ_c. Hence, below this scale, the fluctuations are a product of the in situ dynamics in the solar wind flow (Kiyani et al., 2015). The correlation length also defines the size of the largest energy containing 'eddies' of the turbulent flow. In the inertial range the MHD energy cascade from large to small scales takes place. It is well established that the power spectral density follows approximately the Kolmogorov index $f^{-5/3}$ in this range (e.g., Matthaeus et al., 1982; Denskat et al., 1983; Horbury et al., 1996; Leamon et al., 1998a; Bale et al., 2005). Although the hydrodynamic phenomenology of neutral fluids can partially be transferred to inertial range plasma turbulence, additional physics of the anisotropy of the energy transport have to be taken into account, which are introduced in Section 'Anisotropy and Critical Balance'. The inertial range ends when the turbulent energy reaches the ion scales, where the fluid picture of MHD breaks down. At these scales, the physical mechanisms change leading to a modification of the cascading process possibly including dissipation, which results in a steepening of the spectral slope (Leamon et al., 1999; Alexandrova & Carbone, 2008; Chen et al., 2014). At scales smaller than ion scales, a second cascade range up to electron scales with a steeper slope of about -2.9 to -2.3 is observed (Alexandrova et al., 2009; Kiyani et al., 2009; Chen et al., 2010; Sahraoui et al., 2010), which is called the sub-ion range. Between the inertial range and the sub-ion range, a transition region is observed, where the spectra exhibit a power-law with a variable spectral slope of -4 to -2 (Leamon et al., 1998a; Smith et al., 2006; Roberts et al., 2013) or a smooth non-power-law behavior (Bruno & Trenchi, 2014).

These observations appear to be consistent with an important role of KAWs. The following picture of KAW-generated turbulent cascade is presented in the literature: In the inertial range nonlinear interactions between Alfvén waves are responsible for the generation of the turbulent cascade. The steeping in the transition region has been associated with ion dissipation (Denskat et al., 1983; Smith et al., 2012) or with the presence of coherent structures (Lion et al., 2016). However, the process that leads to a steepening of the spectrum in the sub-ion range, i.e., between ion and electron scales, is the transformation from the non-dispersive Alfvén wave to the dispersive KAW (Howes et al., 2006). The energy in Alfvénic fluctuations generates a dispersive KAW cascade down to the electron scales, which again can be described in fluid-like terms (Schekochihin et al., 2009). Whether the kinetic scale fluctuations have the characteristics of KAW (Leamon et al., 1998b, 2000; Bale et al., 2005; Howes et al., 2008; Schekochihin et al., 2009) or whistler waves (Stawicki et al., 2001; Gary & Smith, 2009; Podesta et al., 2010), is still a much debated topic. Recent observations concerning this question are presented in the next section.

Whistler Waves versus Kinetic Alfvén Waves

Knowledge of the nature of kinetic fluctuations is essentially needed to unravel the physical mechanism by which the turbulent energy is dissipated at small scales. The problem in identifying the wave mode that generates turbulent fluctuations is that it is not possible to distinguish uniquely between the fluctuations due to the sweeping of spatial structures past the spacecraft and temporal fluctuations in the plasma frame in single-point spacecraft measurements. As mentioned in Section 2.2.2, dispersion relations of KAW and whistler waves are similar, therefore, turbulent energy spectra derived from dimensional analysis are the same for both wave modes. However, two quantities that differ for KAW and whistler waves are the ratio of electric to magnetic fluctuations and the ratio of the amplitude of parallel magnetic fluctuations to perpendicular magnetic fluctuations. By calculating these properties for kinetic Alfvén waves and whistler waves and comparing them directly to spacecraft measurements, Salem et al. (2012) find that small scale fluctuations are not consistent with whistler waves. Weakness of their analysis is that they calculate the mentioned ratios based on the cold plasma dispersion relation for whistler waves and not from linear Maxwell-Vlasov theory. Due to the dependence of this approach on the chosen model for dispersion relations of KAW and whistler waves, various authors came to different conclusions (Sahraoui et al., 2012; Gary & Smith, 2009; Smith et al., 2012; He et al., 2012; Kiyani et al., 2013).

A more recent study of Chen et al. (2013) analyses small scale fluctuations based on the difference in frequencies of KAW and whistler waves. As shown in Section 2.2.2, KAWs are low-frequency waves with $\omega \ll \Omega_i$, or $\omega \ll k_\perp v_i$ at scales comparable to the ion gyroradius. Hence, the ions, along with the electrons, are fast enough to be involved in the dynamics. On the contrary, whistler waves are high-frequency waves, where ion density fluctuations, and therefore, due to quasi-neutrality also electron density fluctuations, can be neglected. Figure 2.4 shows power spectral densities of the normalized magnetic field in red and the normalized density in blue. Between ion and electron scales, both spectra show similar amplitudes suggesting that the fluctuations consist of kinetic Alfvén waves, rather than whistler waves. The observed mean value of $\delta\tilde{n}^2/\delta\tilde{b}_\perp^2 = 0.75^{+0.22}_{-0.17}$ is close to a value of 0.786 ± 0.004 obtained in kinetic Alfvén wave simulations and much larger than the expected

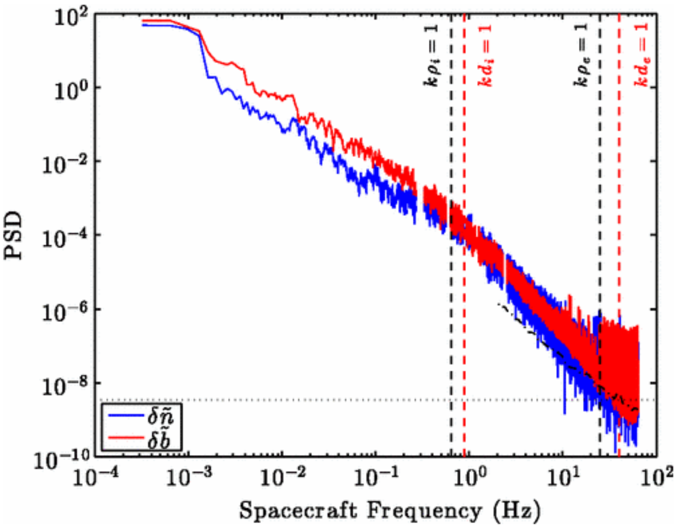

Figure 2.4: Power spectral densities of the normalized magnetic field $\delta\tilde{\mathbf{b}} = \delta\mathbf{B}/B_0$ in red and the normalized electron density $\delta\tilde{n} \sim \delta n/n_0$ in blue measured by ARTEMIS-P2 on October 11, 2010 from 00:21 to 01.14 UT. Vertical dashed lines mark ion and electron gyroradius and inertial length. Figure from Chen et al. (2013). Reproduced by permission of the American Physical Society.

value for whistler waves of ≤ 0.03. The obtained absence of whistler waves in solar wind fluctuations justifies applying Taylor's hypothesis, which is valid for low-frequency dynamics, to relate temporal and spatial scales. Besides the question, which wave mode transports the energy to smaller scales, the answer to the question how the presence of the magnetic field influences this energy transport is crucial for understanding the dissipation mechanism.

Anisotropy and Critical Balance

In the following, we present the concept of anisotropic turbulence and the problems in analyzing the anisotropy in spacecraft measurements, followed by a brief overview of observations that show evidence of anisotropic turbulence. The presence of a local magnetic field results in a breaking of the isotropy in the properties of turbulent fluctuations as it is the case in non-magnetized fluids. The result is the existence of various anisotropies with respect to the magnetic field: First, the anisotropy of the energy transfer rate, i.e., the energy of turbulent fluctuations is transferred more rapidly to smaller perpendicular scales than to smaller parallel scales, which results in a power anisotropy in wavevector space, which is called wavevector anisotropy (e.g., Shebalin et al., 1983; Goldreich & Sridhar, 1995). This anisotropic energy cascade leads secondly to the power anisotropy in frequency space, that is, different levels of power at a certain frequency in the spacecraft frame for different field-to-flow angles (e.g., Bieber, 1996; Horbury et al., 2008). And third, the anisotropic energy cascade results in an anisotropy of the spectral index, i.e., the scaling of the turbulent power is different for different field-to-flow angles (e.g., Horbury et al., 2008).

Difficulties in extracting information regarding these anisotropies from solar wind measurements arise due to the measurement geometry of spacecraft measurements. The spacecraft measures the so-called reduced power spectrum (Fredricks & Coroniti, 1976)

$$P(f) = \int P(\mathbf{k}) \cdot \delta(\mathbf{k} \cdot \mathbf{v}_{SW} - 2\pi f) \mathrm{d}^3\mathbf{k}, \tag{2.40}$$

which contains contributions of various wavevectors with different orientations and wavelengths. In order to make progress in analyzing anisotropic properties, assumptions about the underlying energy distribution in wavenumber space have to be made. In so-called 'weak' turbulence, the energy is transported to larger perpendicular wavenumbers, whereas the parallel wavenumber is preserved. For large wavenumbers, the power is consequently associated with wavevectors at very large field-to-flow angles, which is called '2D' turbulence. This picture led to theories, that solar wind fluctuations consist of mainly '2D' fluctuations combined with 'slab' fluctuations, where the power lies only in parallel wavevectors (e.g., Matthaeus et al., 1990; Tu & Marsch, 1993; Bieber, 1996). When the power in weak turbulent fluctuations cascades to smaller scales, the nonlinear timescale decreases, whereas the Alfvén timescale remains constant because there is no change in the parallel wavenumber. Therefore, these timescales will become equal eventually, which is called 'strong' turbulence. Goldreich & Sridhar (1995) proposed that this equality will remain within the energy cascade to smaller scales, which is called 'critical balance'. By equating the nonlinear timescale at which the energy is transferred to smaller scales with the linear Alfvén timescale, one finds the ratio of parallel to perpendicular wavenumbers $k_\parallel \sim k_\perp^{2/3}$ (detailed derivation of this ratio in both the

MHD and the kinetic regime is given in Chapter 3). Hence, the turbulence becomes more anisotropic for high wavenumbers, and the energy is cascaded mainly in the perpendicular direction. In the kinetic regime, where the turbulence is driven by KAWs or whistler waves, a modified critical balance can be derived, where the nonlinear timescales are equated with the linear timescales of the kinetic wave modes, which leads to a wavenumber ratio of $k_{\parallel} \sim k_{\perp}^{1/3}$ (Cho & Lazarian, 2004; Schekochihin et al., 2009). Based on critical balance, a spectral index in the inertial range of 5/3 for $\theta_{\mathbf{vB}} = 90°$ and of 2 for $\theta_{\mathbf{vB}} = 0°$ and in the kinetic regime of 7/3 for $\theta_{\mathbf{vB}} = 90°$ and of 5 for $\theta_{\mathbf{vB}} = 0°$ (for both KAW and whistler wave driven turbulence) can be derived by dimensional analysis.

The first clear observational evidence of wavevector anisotropy is presented in Matthaeus et al. (1990), who calculated the correlation function of magnetic field fluctuations as a function of distance parallel and perpendicular to the magnetic field, which is shown in Figure 2.5. The results show that the turbulence is not consistent with a purely isotropic wavevector distribution, which would have circular contours. Evidence of the power anisotropy in the spacecraft frame in the inertial range, i.e., higher levels of power for large field-to-flow angles than for small field-to-flow angles is found in Bieber (1996), Narita et al. (2006), Horbury et al. (2008), Podesta (2009), Osman & Horbury (2009), and Luo & Wu (2010). An exemplary observation of the power anisotropy is shown in Figure 2.6 (Wicks et al., 2010). The magnetic power spectrum obtained by Fourier transform is shown in black, the spectrum obtained by wavelet analysis for $\theta_{\mathbf{vB}} = 0°$ (filled dots) and for $\theta_{\mathbf{vB}} = 90°$ (filled squares) is shown in blue. The power is isotropic at large scales and becomes more and more anisotropic with decreasing scale. Additionally, Figure 2.6 reveals that the anisotropic power can only be achieved by having different scalings in different directions to the magnetic field. The observed spectral index anisotropy in the inertial range with a spectral index of 5/3 for $\theta_{\mathbf{vB}} = 90°$ and of 2 for $\theta_{\mathbf{vB}} = 0°$ has been commonly reported (e.g., Horbury et al., 2008; Podesta, 2009; Luo & Wu, 2010; Chen et al., 2011), when using the local magnetic field in a scale-dependent way. This scaling is in agreement with critical balance theory. In studies that take the mean magnetic field as the mean of the entire length of the observed interval, no spectral index anisotropy is seen (Tessein et al., 2009).

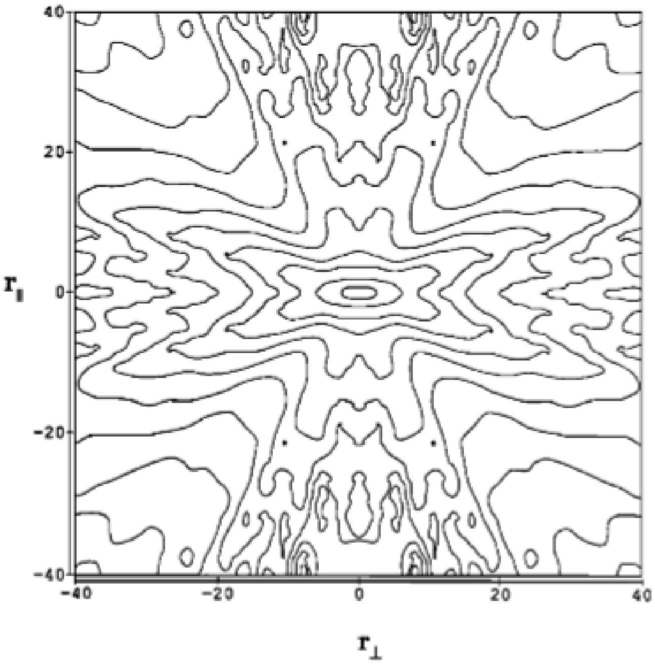

Figure 2.5: Contour plot of the two-dimensional correlation function as a function of distance parallel and perpendicular to the magnetic field obtained from 463 intervals of ISEE 3 magnetometer data. The original data in the $r_{\|} > 0$ and $r_{\perp} > 0$ quadrant has been reflected to fill all four quadrants. $r_{\|}$ and $r_{\perp}$ is shown in units of 10^{10} cm. Figure from Matthaeus et al. (1990). Reproduced by permission of the American Geophysical Union.

Power anisotropy in the kinetic regime was first reported by Leamon et al. (1998a), who find a lower level of anisotropy in the kinetic range than in the inertial range, whereas more recent studies by Chen et al. (2010) and Sahraoui et al. (2010), using multi-spacecraft techniques, find higher levels of anisotropy in the kinetic range, which are comparable to or even higher than the observed levels of anisotropy in the inertial range. Figure 2.7 shows the spectral index anisotropy in the kinetic regime of magnetic field fluctuations both parallel (red) and perpendicular (blue) to the local magnetic field. The spectral index for perpendicular fluctuations $\delta B_{\perp}^2$ varies from around 2.6 for large field-to-flow angles to 3.2 for small angles. The authors mention that their method of obtaining the spectral index from the second order structure function can measure spectral indices up to a value of 3. Therefore, the spectrum in the parallel direction is $\sim k_{\|}^{-3}$ or steeper. Although the spectral indices at large field-to-flow angles are steeper than the theoretical prediction of 7/3, the

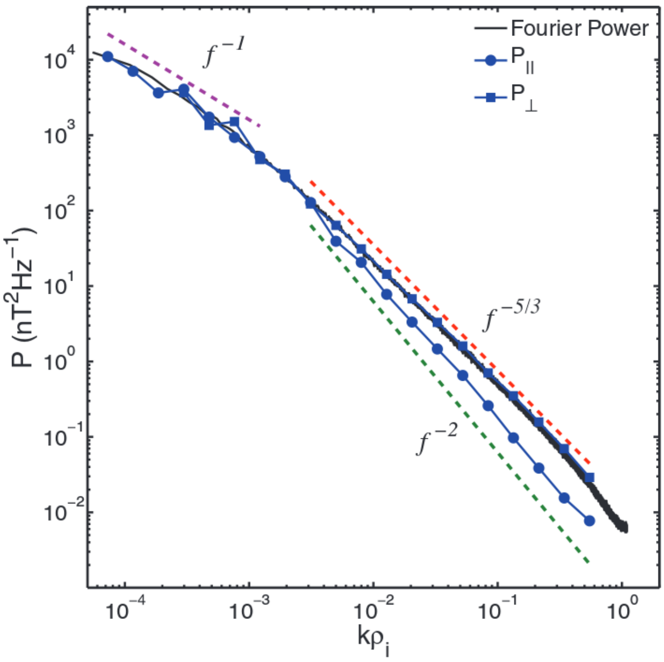

Figure 2.6: Wavelet (blue) and Fourier (black) spectrum of magnetic fluctuations obtained from Ulysses data of day 100-200 of 1995. Figure from Wicks et al. (2010). Reproduced by permission of the Oxford University Press.

steepening of the spectral index towards small angles suggests that the picture of a critically balanced energy cascade is correct. However, the observed values of $\delta B_{\|}^2$ are less consistent with the theoretical predictions because $\delta B_{\|}^2$ is expected to scale in the same way as $\delta B_{\perp}^2$ for a KAW energy cascade (Schekochihin et al., 2009). This result suggests that the KAW picture might be incomplete and other wave modes or cascade mechanisms might contribute to the energy transport. Although recent observations and simulations are consistent with the critical balance assumption (TenBarge & Howes, 2012; He et al., 2013; von Papen & Saur, 2015), its applicability to solar wind turbulence is still subject of debate, and other models are proposed to explain the anisotropy (Narita et al., 2010; Li et al., 2011; Horbury et al., 2012; Wang et al., 2014; Narita, 2015).

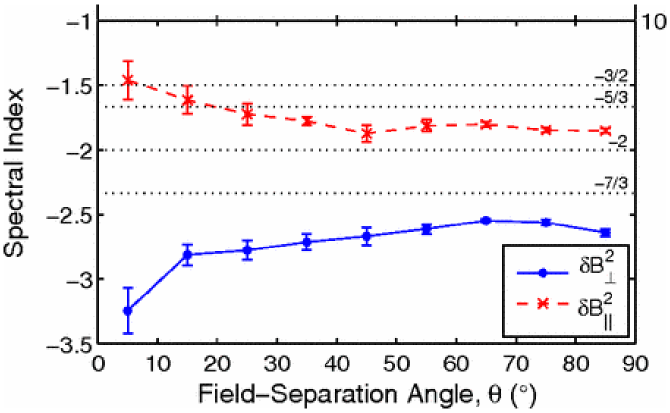

Figure 2.7: Spectral index of magnetic power spectral densities in the kinetic regime for fluctuations parallel (red) and perpendicular (blue) with respect to the magnetic field obtained by Chen et al. (2010) from Cluster data. Figure from Chen et al. (2010). Reproduced by permission of the American Physical Society.

Observations of Electron Scale Turbulence

The turbulent energy, which is transported in a KAW generated cascade from ion to smaller scales, finally reaches the electron scales, i.e., the electron gyroradius ρ_e and the electron inertial length λ_e. These scales are typically $\sim 1\,\mathrm{km}$ in the solar wind at 1 AU (Alexandrova et al., 2009; Sahraoui et al., 2009), and hence, they are convected past the spacecraft in a couple of milliseconds at typical solar wind velocities. Therefore, observations that are able to resolve the fluctuations at these scales must be made at cadences of the order of 100 Hz, which requires high time resolved magnetic field and plasma data measurements. Although Denskat et al. (1983) obtained high resolution magnetic spectra from Helios measurements up to 50 Hz at 1 AU and up to 470 Hz at 0.3 AU, the characteristic electron scales were not reached. It was only with the Cluster STAFF instrument, which consists of a search coil magnetometer and a spectrum analyzer instrument, that these scales were resolved for the first time.

The first direct determination of the dissipation range at electron scales in solar wind turbulence is reported in Sahraoui et al. (2009); their results are shown in Figure 2.8. The parallel (black, green) and perpendicular (red, blue) magnetic power spectral densities follow a power-law with a spectral index close to the Kolmogorov

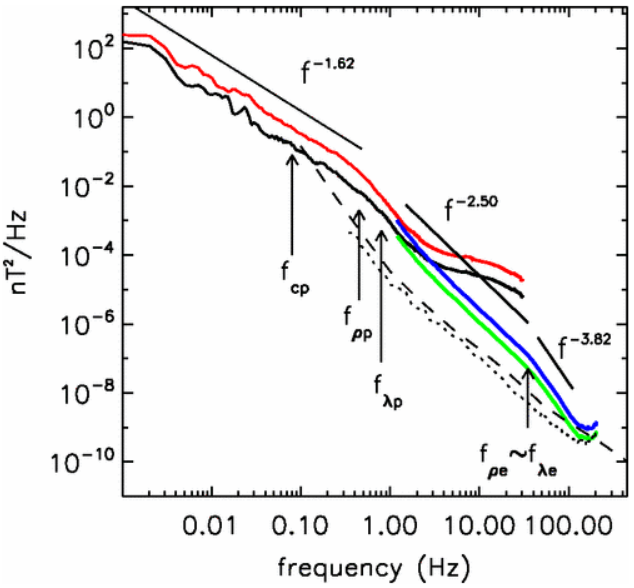

Figure 2.8: Parallel (black, green) and perpendicular (red, blue) magnetic power spectral densities of Cluster FGM data up to 33 Hz and STAFF-SC data for frequencies between 1.5 Hz and 225 Hz measured on 19 March 2006 from 20h30 to 23h20 UT. Dashed and dotted lines give the noise level, respectively. Black arrows indicate characteristic frequencies. Figure from Sahraoui et al. (2009). Reproduced by permission of the American Physical Society.

index in the inertial range, and a power-law with a spectral index of 2.5 in the sub-ion range, which is in agreement to the observations shown in Section 'Observations from MHD to Sub-Ion Scales'. These observations show, for the first time, that the turbulent energy cascade at ion scales continues at least for about two more decades in spacecraft frequency. This result suggests that the turbulent energy is at the most slightly damped at ion scales and undergoes another turbulent cascade down to electron scales (marked by f_{ρ_e} and f_{λ_e}). At these scales, a second breakpoint is seen followed by a steeper spectrum of $\sim f^{-3.8}$. The observation appears consistent with the KAW theory, were strong electron Landau damping at electron scales removes energy from the turbulent cascade, which may explain the strong steepening of the spectrum to $f^{-3.8}$. Landau damping is one kind of wave-particle interaction, where the particles gain energy from the turbulent fluctuations when the resonance condition $\omega_r \sim k_\| v_s$ is fulfilled. By equating the Landau resonance condition and an approximate KAW frequency $\omega_r = \pm k_\| v_A k_\perp \rho_i / \sqrt{\beta_i + 2/(1 + T_e/T_i)}$ (Howes et al., 2008), Sahraoui et al. (2009) obtain a dissipation scale $k\rho_e \sim 0.8$. For a KAW cascade the cyclotron resonance $\omega_r - k_\parallel v_s = \pm\Omega_s$ is not as important as Landau damping due to the low-frequency nature of KAWs.

Contrary results are presented in Alexandrova et al. (2009) and Alexandrova et al. (2012), who observe an exponential decay in the electron dissipation range. In both studies, they find that magnetic power spectra have a similar shape for different plasma conditions and different solar wind velocities, which indicates a certain universality of solar wind turbulence at electron scales. The most intense spectrum of Alexandrova et al. (2012) is shown in Figure 2.9. The magnetic power spectrum in green and red is in good agreement with the proposed exponential model that is defined by an exponential function with the dissipation scale $l_d = \rho_e$ and a power-law pre-factor

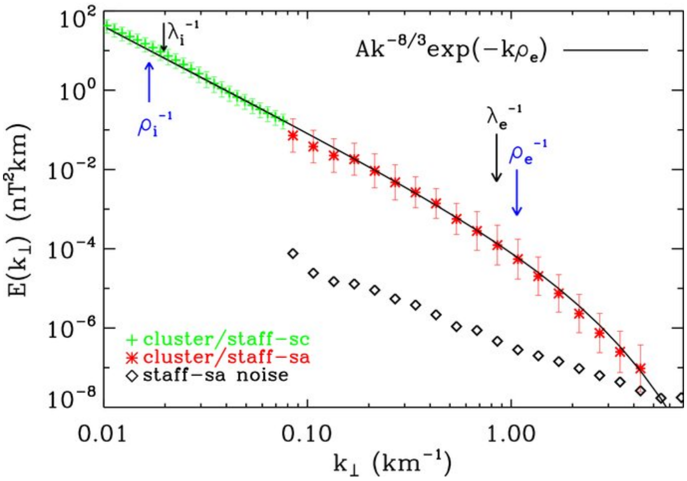

Figure 2.9: Magnetic power spectral densities of Cluster STAFF-SC data (green) and STAFF-SA data (red) measured on 2004 January 22. Diamonds mark the STAFF-SA noise level. Blue and black arrows indicate characteristic ion and electron scales. The exponential model $Ak^{-8/3}\exp(-k\rho_e)$ is shown in the black solid line. Figure from Alexandrova et al. (2012). Reproduced by permission of the American Astronomical Society.

$$E(k_\perp) = Ak_\perp^{-\alpha}\exp(-k_\perp l_d). \tag{2.41}$$

Summarized results of fitting (2.41) to 100 observed magnetic power spectra in the free solar wind at 1 AU are shown in Figure 2.10. Panel (a) shows a histogram of the spectral index $\alpha = 2.63 \pm 0.15$, panel (b) the dissipation length as a function

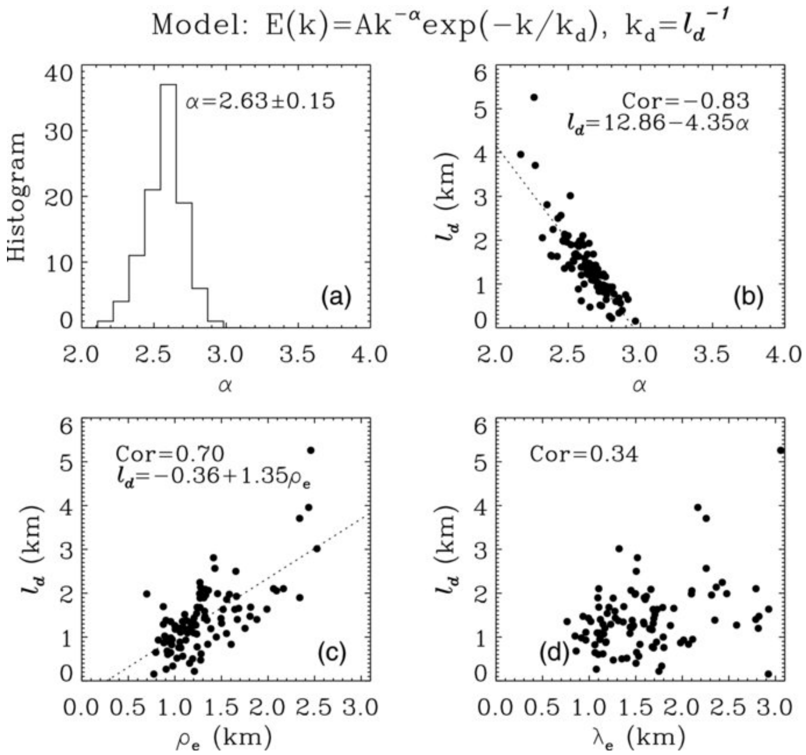

Figure 2.10: Results of fitting (2.41) to 100 observed magnetic power spectra. (a) spectral index α in sub-ion range; (b) dissipation length l_d as a function of the spectral index α; (c) dissipation length l_d as a function of the electron gyro radius ρ_e; (d) dissipation length l_d as a function of the electron inertial length. Figure from Alexandrova et al. (2012). Reproduced by permission of the American Astronomical Society.

of $\alpha = 2.9 - l_d/4.4$, and panel (c) and (d) the dissipation length as a function of the electron gyroradius $l_d = -0.36 + 1.35\rho_e$ and the electron inertial length, respectively. Owing to the high correlation of the dissipation length and the electron gyroradius and the much weaker correlation with the electron inertial length, the authors conclude that the electron gyroradius plays the role of the dissipation length in solar wind turbulence.

A surprising result in the observations by Alexandrova et al. (2012) is the independence of the dissipation length from the amplitude of the turbulent spectra P_0 at a fixed wavenumber k_0. Figure 2.11 shows the superposition of all analyzed spectra in Alexandrova et al. (2009) and Alexandrova et al. (2012). The spectra are only shifted vertically by a parameter E_0 and not horizontally, which indicates that the

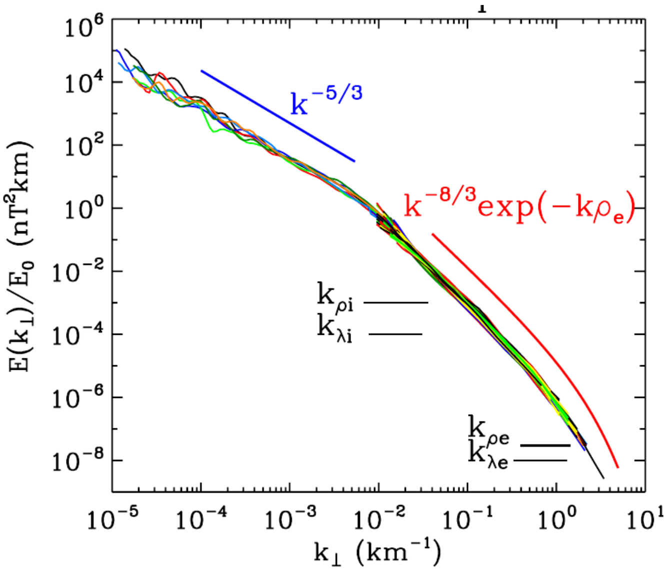

Figure 2.11: Superposition of 107 solar wind spectra analyzed in Alexandrova et al. (2009, 2012). The spectra are shifted vertically by a parameter $E_0 = \langle E_j(k)/E_1(k)\rangle$, where $\langle ... \rangle$ defines the mean over wavenumbers and $E_1(k)$ a reference spectrum. Characteristic ion and electron scales are marked in black. The blue line gives a power-law $\sim k^{-5/3}$ and the red line shows $\sim k^{-8/3} exp(-k\rho_e)$. Figure from Alexandrova et al. (2012). Reproduced by permission of the American Astronomical Society.

dissipation length does not depend on the amplitude of the turbulent spectrum P_0 and therefore also not on the energy cascade rate $\varepsilon_0 \sim P_0^{3/2} k_0^{5/2}$. This independence is a remarkable difference compared to hydrodynamic turbulence, where the dissipation length $l_{d,\mathrm{Kolm}} = (\nu^2/\varepsilon_0)^{1/4}$ is given by the energy cascade rate ε_0 and the kinematic viscosity ν. Accordingly, in hydrodynamic turbulence, the more energy is injected per unit mass, the more the turbulence is driven to smaller scales to dissipate the larger energy flux. This difference of solar wind turbulence is indeed surprising under the assumption that the energy is not fully dissipated at a resonance, but that the dissipation rate γ is a smooth function of wavenumber k such as, e.g., for Landau damping of KAWs (Lysak & Lotko, 1996; Howes et al., 2006; Sahraoui et al., 2012; Narita & Marsch, 2015). In this case, one would still expect that a larger energy flux drives the turbulence to smaller scales before the energy is dissipated.

Although the finding of Alexandrova et al. (2009, 2012) that the electron gyroradius is the dissipation scale of solar wind turbulence is in agreement with the study by Sahraoui et al. (2009), the question whether the dissipation range follows a power-law or a exponential decay is still under debate. In a comment on Sahraoui et al. (2009), Alexandrova et al. (2013) argued that the observed interval in Sahraoui et al. (2009) is contaminated by electron beams because the spacecraft was located in the electron foreshock region, which might result in the observed power-law in the electron dissipation range. However, in a subsequent study by Sahraoui et al. (2012) with a large number of intervals that are not contaminated by foreshock electrons, they still find that the double power-law model fits best to the observations. The broad distribution of spectral indices in the electron dissipation range $\sim [3.5, 5.5]$ suggests a lack of universality of electron scale turbulence, which contradicts to the findings in Alexandrova et al. (2009, 2012). A possible explanation for this contradiction might be that Alexandrova et al. (2012) discard intervals that show presence of quasi-parallel propagating whistler waves. These wave modes invalidate Taylor's hypothesis and can change the spectral shape in the dissipation range, which is a well observed feature in Earth's magnetosheath turbulence (e.g., Alexandrova et al., 2008). Particularly due to the controversial findings in the electron dissipation range, the small-scale cascade of turbulent energy and its dissipation is still not sufficiently understood. Open questions that were presented above and that form the basis for the motivation of our dissipation model are summarized in the next section.

Outstanding Questions

In Chapter 3, we present a one-dimensional model of dissipation at electron scales with damping by KAWs in wavenumber space, which we compare with observed power spectra by applying Taylor's hypothesis. With the help of that model, we aim to answer the question if a KAW generated turbulent energy cascade can explain the observed power spectral densities in the solar wind. Or, in more detail: Do the kinetic scale fluctuations have the characteristics of whistler waves or KAWs? What damping mechanisms result in a exponentially shaped or a power-law dissipation range? What is the dissipation length of KAW generated turbulence? And what is the cause for the observed independence of the dissipation length from the energy cascade rate? With the extension of the one-dimensional model to three dimensions and the calculation of the reduced power spectra in Chapter 4, we additionally intend to answer the questions whether critical balance theory is in agreement with the observations in both the MHD and the kinetic regime; and whether KAW damping can explain the observed spectra in the sub-ion range, which are steeper than the predicted spectral index of 7/3.

3 One-Dimensional Dissipation Model in Wavenumber Space

In the following, we present the idea and derivation of the one-dimensional dissipation model, the numerical evaluation of the dispersion relation for KAWs, and theoretical implications for the dissipation process on the basis of our model. In the second part of this chapter, we compare the dissipation model with an observed exemplary magnetic power spectrum, followed by a statistic analysis that aims to determine the dissipation length of KAW driven turbulence. In the discussion part, we discuss the limitations of the assumptions made in the derivation of the dissipation model. Most ideas and figures of this chapter are published in Schreiner & Saur (2017). The basic idea of the dissipation model was developed in my Master's thesis presented to the University of Cologne in 2013 with the title 'Dissipation des Sonnenwindes durch kinetische Alfvén Wellen'.

3.1 Idea and Derivation of the One-Dimensional Dissipation Model

In this section, we derive a dissipation model for magnetic power spectral densities of turbulent fluctuations. The model is a linear combination of the nonlinear transport of energy from the large to the small scales, and the dissipation process at small scales. In its general form, the model can in principle describe turbulent spectra in any plasma or fluid. For solar wind turbulence, we assume a critically balanced energy cascade of KAWs up to the highest wavenumbers, where the energy is dissipated by wave-particle interactions. Turbulent dissipation is quantified by the imaginary part of the wave frequency obtained from the dispersion relation for KAWs. The idea of combining the energy transport to smaller scales with linear damping has been previously introduced in Howes et al. (2008) and Podesta et al. (2010). Still, we give a short derivation of our model equation in the following in order to establish a basis for theoretical predictions of the solar wind dissipation process.

Based on Kolmogorov's idea that the turbulent energy cascades self-similarly to higher wavenumbers, we write the energy cascade rate as

$$\varepsilon(k) = C_K^{-3/2} P(k) v_k(k), \tag{3.1}$$

where $P(k)$ defines the power spectral density of magnetic fluctuations and C_K is the dimensionless Kolmogorov constant. We introduce the 'velocity' of the energy transport in wavenumber space or 'eddy-decay velocity' $v_k(k) = \mathrm{d}k/\mathrm{d}t$, with which the energy is cascaded from one wavenumber to the next. In the inertial range, the energy is transported loss-free from large to small scales, therefore the energy cascade rate $\varepsilon(k) = \varepsilon_0$ is constant and can be written as

$$\varepsilon_0 = C_K^{-3/2} P_0 v_{k0}, \tag{3.2}$$

where $P_0 = P(k_0)$ and $v_{k0} = v_k(k_0)$ characterize the spectral properties at a wavenumber k_0 in the inertial range. The fluid velocity v and the eddy-decay velocity of magnetic fluctuations v_k are related by

$$v_k(k) = \frac{\mathrm{d}k}{\mathrm{d}t} = k^2 v(k). \tag{3.3}$$

The ratio of velocity fluctuations to magnetic fluctuations is defined as α (Schekochihin et al., 2009),

$$v(k) = \alpha \sqrt{\frac{P(k)k}{\rho}}, \tag{3.4}$$

with the mass density ρ. Approximated expressions for α in both the MHD and the kinetic regime are given later in this section. From (3.1), (3.3), and (3.4), we obtain an expression for the spectral energy density $P(k)$,

$$P(k) = C_K \rho^{1/3} \varepsilon(k)^{2/3} \alpha(k)^{-2/3} k^{-5/3}. \tag{3.5}$$

Assuming α to follow a power-law of the form $\alpha = \alpha_0 (k/k_0)^\beta$, we can write $P(k)$ as

$$P(k) = P_0 \left(\frac{\varepsilon(k)}{\varepsilon_0} \right)^{2/3} \left(\frac{k}{k_0} \right)^{-\kappa}, \tag{3.6}$$

with $\kappa = 2/3\beta + 5/3$. Equation (3.6) demonstrates the power-law behavior of the power spectral density in the inertial range, where the energy flux is constant, i.e., $\varepsilon_0 = \varepsilon(k)$. At scales, where dissipation becomes effective, the energy flux $\varepsilon(k)$ is reduced by the part of energy that is dissipated, so that the power spectral density does not follow a power-law anymore. With Equations (3.1), (3.2), and (3.6), we write the eddy-decay velocity $v_k(k)$ as

$$v_k(k) = v_{k0} \left(\frac{\varepsilon(k)}{\varepsilon_0} \right)^{1/3} \left(\frac{k}{k_0} \right)^{\kappa}. \tag{3.7}$$

Similar to the power spectral density in (3.6), the eddy-decay velocity follows a power-law until the energy reaches scales where dissipation sets in, which slows down the turbulent energy transport. Due to dissipation, the energy flux at wavenumber $k' = k + \mathrm{d}k$ differs from the energy flux at k by the part of energy $D(k)\mathrm{d}k$ that is dissipated,

$$C_K^{-3/2} P(k) v_k(k) = C_K^{-3/2} P(k') v_k(k') + D(k)\mathrm{d}k. \tag{3.8}$$

The heating rate $D(k) = 2P(k)\gamma(k)$ is defined as the spectral energy times the damping rate $\gamma(k)$. From (3.6)-(3.8), and a Taylor expansion of $P(k')v_k(k')$ for small $\mathrm{d}k$ in Equation (3.8), we obtain a differential equation for the power spectral densities of turbulent fluctuations $P(k)$,

$$\frac{\mathrm{d}P(k)}{\mathrm{d}k} = -P(k) \left(\frac{\kappa}{k} + \frac{4}{3} C_K^{3/2} \frac{\gamma(k)}{v_k(k)} \right). \tag{3.9}$$

The solution of (3.9) for $P(k)$ gives the one-dimensional power spectrum of magnetic fluctuations

$$P(k) = P_0 \left(\frac{k}{k_0} \right)^{-\kappa} \exp \left(-\frac{4}{3} C_K^{3/2} \int_{k_0}^{k} \mathrm{d}k' \frac{\gamma(k')}{v_k(k')} \right). \tag{3.10}$$

Insertion of (3.1) and (3.5) into (3.10) leads to

$$P(k) = P_0 \left(\frac{k}{k_0}\right)^{-\kappa} \exp\left(-\frac{4}{3}C_K \int_{k_0}^{k} \mathrm{d}k' \left(\frac{\varepsilon(k')}{\rho}\right)^{-1/3} \alpha(k')^{-2/3}\gamma(k')k'^{-5/3}\right). \quad (3.11)$$

With (3.6), Equation (3.11) can be written in terms of the energy flux,

$$\varepsilon(k) = \varepsilon_0 \exp\left(-2C_K \int_{k_0}^{k} \mathrm{d}k' \left(\frac{\varepsilon(k')}{\rho}\right)^{-1/3} \alpha(k')^{-2/3}\gamma(k')k'^{-5/3}\right). \quad (3.12)$$

Under the assumption that the eddy-decay velocity is not affected by dissipation,

$$v_k(k) \approx v_{k0} \left(\frac{k}{k_0}\right)^{\kappa}, \quad (3.13)$$

and using (3.2) and (3.5), Equation (3.10) simplifies to

$$\begin{aligned} P(k) = &P_0 \left(\frac{k}{k_0}\right)^{-\kappa} \exp\left(-\frac{4}{3}C_K \left(\frac{\varepsilon_0}{\rho}\right)^{-1/3} \alpha_0^{-2/3}\right. \\ &\left. \times\ k_0^{-5/3} \int_{k_0}^{k} \mathrm{d}k'\gamma(k') \left(\frac{k'}{k_0}\right)^{-\kappa}\right). \end{aligned} \quad (3.14)$$

Turning to hydrodynamic turbulence, we can use our model to calculate the hydrodynamic power spectrum by insertion of a hydrodynamic damping rate $\gamma(k) = \nu k^2$ with the kinematic viscosity ν, which is valid in collisional fluids (e.g., Drake, 2006). When we assume that the eddy-decay velocity is not affected by damping as in (3.13), we find

$$P(k) = P_0 \left(\frac{k}{k_0}\right)^{-5/3} \exp\left(-C_K\nu \left(\frac{\varepsilon_0}{\rho}\right)^{-1/3} k^{4/3}\right), \quad (3.15)$$

where we use $\kappa = 5/3$, $k_0 \ll k$, $\alpha_0 = 1$, and where $P(k)$ denotes the energy density of velocity fluctuations in this case. This spectral form for hydrodynamic turbulence has been found previously by Corrsin (1964) and Pao (1965). Equating the argument of the exponential function in (3.15) with -1, we obtain the dissipation scale for hydrodynamic turbulence

$$l_{d,hd} = C_K^{3/4} \left(\frac{\nu^3 \rho}{\varepsilon_0} \right)^{1/4} , \tag{3.16}$$

which is, apart from constant factors on the order of unity, in agreement with the Kolmogorov dissipation scale $l_{d,\mathrm{Kolm}} \sim (\nu^3/\varepsilon_0^*)^{1/4}$ with the cascade rate per unit mass $\varepsilon_0^* = \varepsilon_0/\rho$. Assuming alternatively that the eddy-decay velocity is slowed down by the damping in the dissipation range according to (3.7), we find an algebraic power spectral density

$$P(k) = P_0 \left(\frac{k}{k_0} \right)^{-5/3} \left(1 - \frac{1}{2} C_K \left(l_{d,hd} k \right)^{4/3} \right)^2 , \tag{3.17}$$

where we again use $\kappa = 5/3$, $k_0 \ll k$, and $\alpha_0 = 1$. $P(k)$ decreases more rapidly compared to the previous case and vanishes at a maximum wavenumber. A similar spectral form has been found by Kovasznay (1948). Expressions (3.15) and (3.17) provide models of how the dissipation and the associated dissipation length depend on the energy flux in hydrodynamic turbulence. Consequences resulting from this fact and differences to solar wind dissipation will be discussed in Section 3.3.

Returning to solar wind turbulence, we include the normalized damping rate for KAWs

$$\gamma(k_\perp, k_\parallel) = k_\parallel v_A \overline{\gamma}(k_\perp, k_\parallel), \tag{3.18}$$

which is the imaginary part of the complex wave frequency in the dispersion relation for KAWs with $\omega = \omega_r + \mathrm{i}\gamma$. Due to the anisotropy of the turbulent cascade, we need to take into account the parallel wavenumber $k_\parallel$ and perpendicular wavenumber $k_\perp$ instead of the absolute value k. Equations (3.1)-(3.14) are also valid for solar wind turbulence, when we replace k by $k_\perp$. We assume that the linear Alfvén timescales and the nonlinear timescales are equal at all scales. This equality is the critical balance assumption of Goldreich & Sridhar (1995), which leads to a relation between $k_\parallel$ and $k_\perp$,

$$v_\perp(k_\perp) k_\perp = k_\parallel v_{ph,A} = k_\parallel v_A \overline{\omega}_r, \tag{3.19}$$

where $v_\perp$ is the plasma velocity perpendicular to the mean magnetic field, which we take in the remainder as the turbulent velocity fluctuations introduced in (3.3) and (3.4). $v_{ph,A} = v_A\overline{\omega}_r$ is the phase velocity of the wave, and $\overline{\omega}_r = \omega_r/k_\parallel v_A$ is the real part of the normalized wave frequency describing the deviations from the MHD shear Alfvén wave. From Equations (3.1), (3.3), (3.5), and (3.19), we obtain an equation for the parallel wavenumber as a function of the perpendicular wavenumber

$$k_\parallel = C_K^{1/2}(v_A\overline{\omega}_r)^{-1}\left(\frac{\varepsilon(k_\perp)}{\rho}\right)^{1/3}\alpha(k_\perp)^{2/3}k_\perp^{2/3}. \tag{3.20}$$

For $\alpha(k_\perp) \approx \overline{\omega}_r$ (Howes et al., 2008) and without dissipation ($\varepsilon(k_\perp) = \varepsilon_0$), (3.20) leads to the typical relations for $k_\parallel$ and $k_\perp$ as discussed in Section 2.2.3 in both the MHD regime ($\overline{\omega}_r \approx 1$) and the kinetic regime ($\overline{\omega}_r \approx k_\perp\rho_i$). Inclusion of (3.18) and (3.20) in Equation (3.11) gives the perpendicular power spectrum of magnetic fluctuations,

$$P(k_\perp) = P_0\left(\frac{k_\perp}{k_0}\right)^{-\kappa}\exp\left(-\frac{4}{3}C_K^{3/2}\int_{k_0}^{k_\perp}\mathrm{d}k'_\perp\frac{\overline{\gamma}(k'_\perp,k_\parallel)}{\overline{\omega}_r(k'_\perp,k_\parallel)}k'^{-1}_\perp\right). \tag{3.21}$$

Equation (3.21) shows that the power spectral density can be described as a combination of the energy cascade, which follows a power-law, and an exponential damping term, which removes more and more energy from the turbulent cascade with increasing damping rate $\overline{\gamma}/\overline{\omega}_r$. Again with Equation (3.6), Equation (3.21) can be expressed in terms of the energy flux

$$\varepsilon(k_\perp) = \varepsilon_0\exp\left(-2C_K^{3/2}\int_{k_0}^{k_\perp}\mathrm{d}k'_\perp\frac{\overline{\gamma}(k'_\perp,k_\parallel)}{\overline{\omega}_r(k'_\perp,k_\parallel)}k'^{-1}_\perp\right). \tag{3.22}$$

The energy flux is constant in the inertial range, where the damping rate is negligible small, and it is reduced in the kinetic regime due to the exponential damping term. From (3.3), (3.10), (3.18), and (3.19), we see that the power spectrum in Equation (3.21) and the associated energy flux in Equation (3.22) are independent of the choice of the eddy-decay velocity in the dissipation range, i.e., Equations (3.7) and (3.13) lead to the same result. The numerical evaluation of the general dispersion relation, from which we obtain $\overline{\gamma}/\overline{\omega}_r$ depending on the plasma parameters, is presented in the following section.

3.2 Damping Rates of Kinetic Alfvén Waves

In this section, we present the details of the numerical evaluation of the general dispersion relation in (2.32) and compare the obtained damping rates with two simplified damping rates for KAWs that are presented in the literature to verify the correct implementation. If we make no assumptions for the wave frequency and the plasma beta $\beta_s = 2k_BT_sn_s\mu_0/B^2$, the full system described by Equation (2.32) needs to be solved numerically to find the wave frequency for given plasma parameters. In contrast to most previous studies, we do not apply the eight-pole approximation (Padé approximation) to evaluate the plasma dispersion function $Z(\xi)$ (e.g., Rönnmark, 1982) but evaluate the Z function directly in the form

$$Z(\xi) = i\sqrt{\pi}\exp(-\xi^2)\ \mathrm{erfc}(\xi) \tag{3.23}$$

with the complementary error function $\mathrm{erfc}(\xi)$ (e.g., Abramowitz & Stegun, 1964). In this way, we make sure that the damping rates are evaluated correctly even for heavily damped waves, i.e., $\mathrm{Im}(\omega) > -k_\parallel$ or $\mathrm{Im}(\omega) > -\mathrm{Re}(\omega - n\Omega)$ (Rönnmark, 1982). A two-dimensional Newton's method root search in the complex frequency plane is used to find the solution of Equation (2.32). To ensure accurate results for high perpendicular wavenumbers, the number of sum elements that are kept is about the same as $k_\perp\rho_i$ (Howes et al., 2006). We implemented an iterative root search to track the required wave mode from small wavenumbers to large wavenumbers. An initial guess of the frequency is set at a given initial wavenumber (e.g., MHD Alfvén wave frequency to track the kinetic Alfvén wave). At neighboring wavenumbers, the solution is then found by using the previously obtained frequency as an initial guess.

In the following, we compare the obtained damping rates with damping rates obtained from the hot dispersion relation with the Padé approximation for the plasma dispersion function $Z(\xi)$, which is used frequently in other dispersion relation solvers (Rönnmark, 1982; Narita & Marsch, 2015), and damping rates obtained from a simplified algebraic dispersion relation presented in Lysak & Lotko (1996), which was derived to describe low-frequency waves in small plasma beta plasmas, e.g., Earth's magnetosphere. The advantage of both methods is much faster computation times of the root finding algorithm in comparison to the hot dispersion relation solver. For low-frequency waves ($\omega \ll \Omega_s$), large parallel wavelength ($k_\parallel v_s \ll \Omega_s$), and small plasma betas ($\beta_s \ll 1$) the full system of the hot dispersion relation reduces to a 2×2 matrix. The determinant of this system gives the simplified dispersion relation for KAWs (Lysak & Lotko, 1996)

$$\frac{\omega^2}{k_\parallel^2 v_A^2} = \frac{k_\perp^2 \rho_i^2}{1 - \Gamma_0(k_\perp^2 \rho_i^2)} + \frac{k_\perp^2 \rho_a^2}{\Gamma_0(k_\perp^2 \rho_e^2)\left[1 + \xi Z(\xi)\right]}, \tag{3.24}$$

with the gyroradius $\rho_s = v_s/\Omega_s$ and the ion acoustic gyroradius $\rho_a^2 = k_B T_e / m_i \Omega_i^2$. Note that $\xi = \xi(\omega)$; thus, Equation (3.24) is an implicit equation for the normalized wave frequency $\overline{\omega} = \overline{\omega}_r + \mathrm{i}\overline{\gamma}$, which can be solved numerically. Figure 3.1

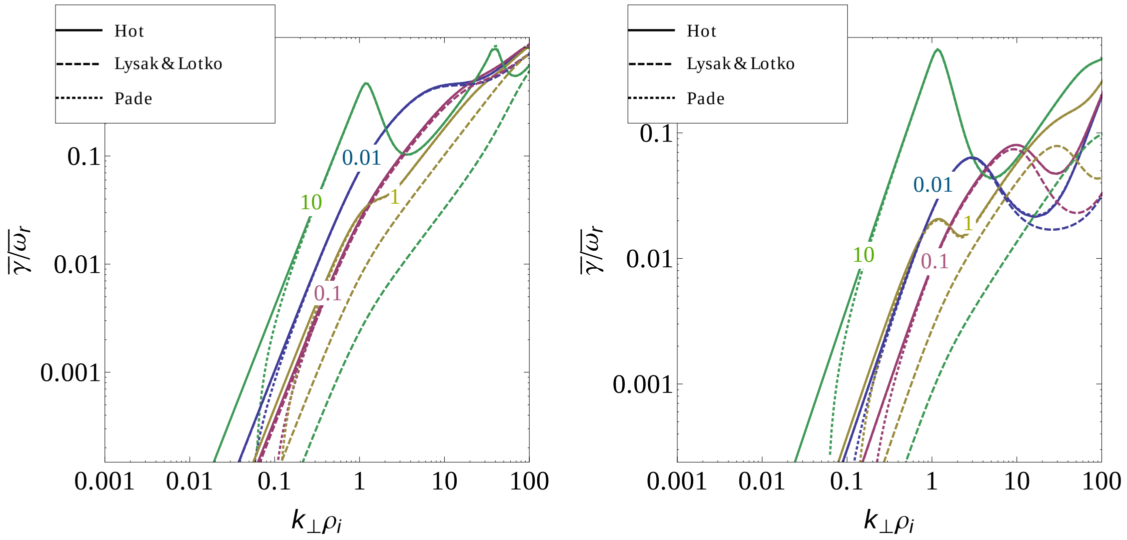

(a) (b)

Figure 3.1: $\overline{\gamma}/\overline{\omega}_r$ for a temperature ratio of $T_i/T_e = 1$ (a) and of $T_i/T_e = 10$ (b) and ion plasma betas of 0.01, 0.1, 1, and 10. Damping rates from the simplified dispersion relation are shown in dashed lines, hot damping rates in solid lines and hot damping rates with Padé approximation in dotted lines. Figure from Schreiner & Saur (2017).

shows normalized damping rates ($\overline{\gamma}/\overline{\omega}_r$) calculated from the hot dispersion relation (solid lines), the hot dispersion relation with Padé approximation (dotted lines), and the Lysak & Lotko (1996) approximation (dashed lines) for temperature ratios of $T_i/T_e = 1$ (a) and $T_i/T_e = 10$ (b) for ion plasma beta values of 0.01, 0.1, 1, and 10. The ratio of $k_\parallel$ to $k_\perp$ is given through the critical balance condition in (3.20). We use typical solar wind values for the magnetic field (10 nT) and the electron number density ($10\,\mathrm{cm}^{-3}$). For all values of β_i, hot damping rates with Padé approximation are in agreement with hot damping rates for $k_\perp \rho_i > 1$, but show small errors when the wave frequency is almost real and γ is nearly negligibly small. Due to critical balance, the real part of the wave frequency does not reach the ion gyrofrequency where differences of the plasma dispersion function and the Padé approximation would occur. The real part of the wave frequency normalized by the ion gyrofrequency ω_r/Ω_i is shown in Figure 3.2 again for temperature ratios of $T_i/T_e = 1$ (a) and $T_i/T_e = 10$ (b) for ion plasma beta values of 0.01, 0.1, 1, and 10. For both temperature ratios and all values of β_i, the wave frequency does not significantly exceed the ion gyrofrequency under the assumption of critical balance.

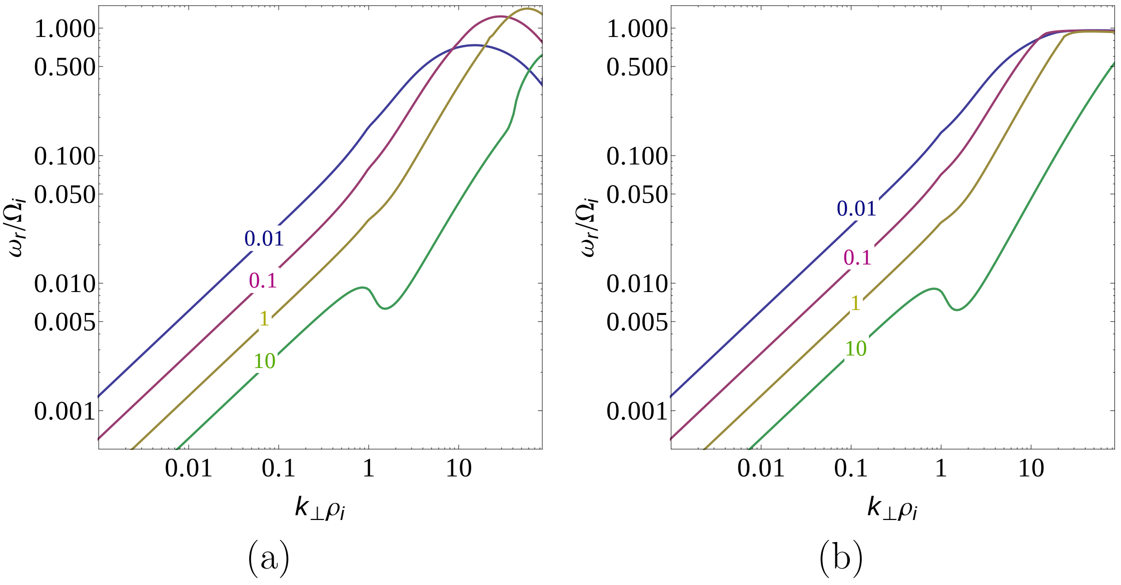

Figure 3.2: Real part of the wave frequency normalized by the ion gyroradius ω_r/Ω_i for a temperature ratio of (a) $T_i/T_e = 1$ and (b) $T_i/T_e = 10$ and ion plasma betas of 0.01, 0.1, 1, and 10.

Therefore, the obtained damping rates can be associated with kinetic Alfvén waves and not whistler waves, as shown in 2.2.2. Returning to Figure 3.1, damping rates calculated with the Lysak & Lotko (1996) approximation (dashed lines) show good agreement with hot damping rates for $\beta_i = 0.01$ and $\beta_i = 0.1$. Small deviations occur at $k_\perp \rho_i \approx 10$, where ω_r approaches the ion gyrofrequency. For $\beta_i \geq 1$, both the amplitude and the general form of the damping rates calculated with the Lysak & Lotko (1996) approximation differ significantly from hot damping rates already for scales $k_\perp \rho_i < 1$. The results confirm that the Lysak & Lotko (1996) dispersion relation can be well applied for $\beta_i \ll 1$, $\beta_e \ll 1$ and $\omega_r \ll \Omega_i$. Although the simplified dispersion relation is valid for a range of solar wind parameters, quantitative conclusions concerning damping at electron scales cannot be drawn. For a complete analysis of dissipation processes under the full parameter space of the solar wind conditions usage of the hot dispersion relation is necessary.

3.3 Theoretical Implications for the Solar Wind Dissipation Process

With our model for the power spectral density in Equation (3.21), we can draw conclusions about the dissipation length and the spectral shape of the solar wind dissipation range. Let us first look at the critical balance assumption in Equation (3.20) again. Equation (3.20) reveals the dependence of the parallel wavenumber on the energy flux $\varepsilon(k_\perp)$. Consequently, $\gamma(k_\perp, k_\parallel)$ depends on $\varepsilon(k_\perp)$ as well. Returning to the general spectral form in Equation (3.11), we see that $\varepsilon(k_\perp)$ cancels under the assumption of critical balance so that the dissipation is not explicitly dependent on $\varepsilon(k_\perp)$. However, $\overline{\omega}_r = \omega_r / k_\parallel v_A$ and $\overline{\gamma} = \gamma / k_\parallel v_A$ in Equation (3.21) can be explicit functions of $k_\parallel$, if $\gamma(k_\perp, k_\parallel)$ and $\omega_r(k_\perp, k_\parallel)$ are nonlinear functions of $k_\parallel$. Damping rates calculated from the Lysak & Lotko (1996) approximation in Equation (3.24) satisfy the condition $\overline{\gamma}(k_\perp) = \gamma(k_\perp, k_\parallel)/k_\parallel v_A$ exactly leading to a dissipation which is independent of the energy flux and hence to the same dissipation scale for different values of the energy flux. For normalized damping rates for KAWs obtained from the hot plasma dispersion relation in (2.31), the independence of $\overline{\gamma}/\overline{\omega}_r$ from the parallel wavenumber cannot be shown analytically but can be estimated numerically. Figure 3.3 shows the parallel wavenumber as a function of the perpendicular

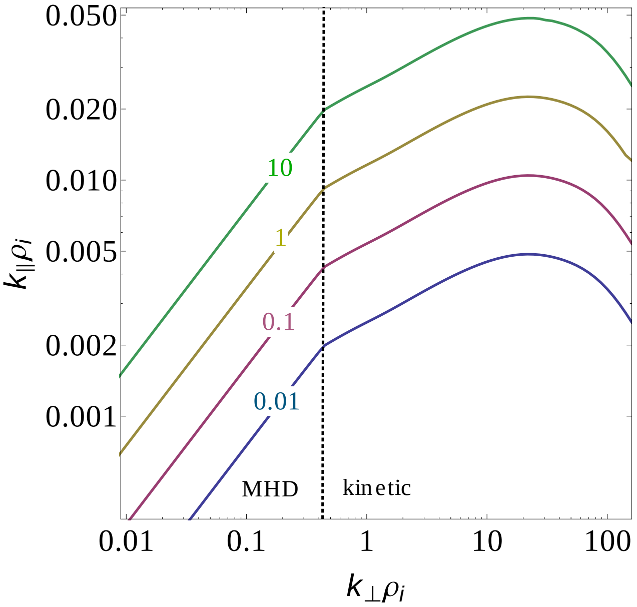

Figure 3.3: Equation (3.20) for $\varepsilon_0 = \{0.01, 0.1, 1, 10\} \times \varepsilon_{0,\mathrm{ref}}$ with $\varepsilon_{0,\mathrm{ref}} = 7 \times 10^{-16}\,\mathrm{Jm^{-3}s^{-1}}$. The dotted line shows the transition from MHD to the kinetic regime. Solar wind parameters ($B = 15.5\,\mathrm{nT}$, $n = 20\,\mathrm{cm^{-3}}$, $T_i = 61\,\mathrm{eV}$, $T_e = 26\,\mathrm{eV}$, and $v_{SW} = 630\,\mathrm{km/s}$), the break frequency, and $\varepsilon_{0,\mathrm{ref}}$ are taken from observation 5 in Alexandrova et al. (2009). Figure from Schreiner & Saur (2017).

wavenumber as derived in Equations (3.20) and (3.12) for four different values of ε_0. The dotted line denotes the spectral break at ion scales. The break frequency and the original value of $\varepsilon_{0,\mathrm{ref}} = 7 \times 10^{-16}\,\mathrm{Jm^{-3}s^{-1}}$ are taken from observation 5 in Alexandrova et al. (2009). The larger ε_0 is, the more the turbulence generates large parallel wavenumbers for the same perpendicular wavenumber. Due to the faster eddy-decay velocity for larger ε_0, the energy can travel smaller distances in the parallel direction in one eddy-turnover time, which is equivalent to larger parallel wavenumbers. Figure 3.4 shows the hot damping rate ($\overline{\gamma}/\overline{\omega}_r$) for all ratios of $k_\parallel$ to $k_\perp$ from Figure 3.3. All damping rates fall approximately on the same dark blue solid line. At least for typical solar wind parameters, the normalized hot damping rate for KAWs are approximately independent of the parallel wavenumber: $\overline{\gamma}(k_\perp, k_\parallel)/\overline{\omega}_r(k_\perp, k_\parallel) \sim \overline{\gamma}(k_\perp)/\overline{\omega}_r(k_\perp)$, which leads to the same dissipation scale for

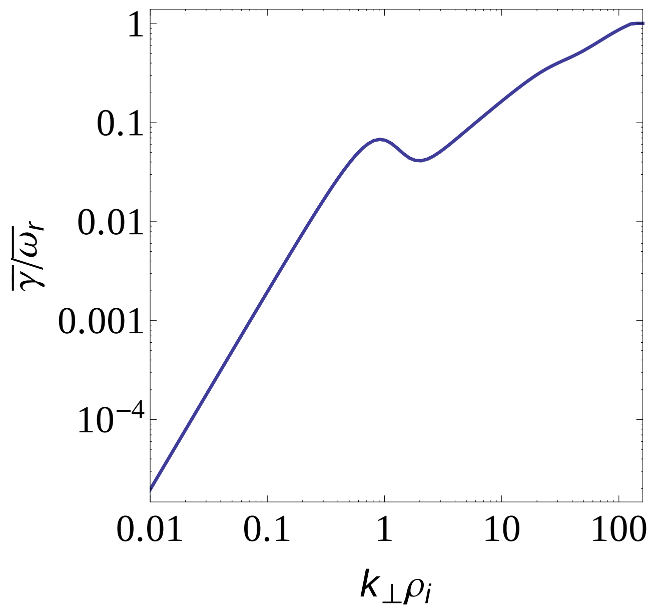

Figure 3.4: Hot damping rate ($\overline{\gamma}/\overline{\omega}_r$) for all ratios of $k_\parallel$ to $k_\perp$ from Figure 3.3 and the same parameters as in Figure 3.3. All damping rates fall approximately on the same dark blue solid line. Figure from Schreiner & Saur (2017).

all spectra independently of the injected energy rate.

We can estimate this dissipation scale for solar wind turbulence similar to the hydrodynamic Kolmogorov dissipation scale by equating the argument of the exponential term in Equation (3.22) with -1, i.e., where the energy flux is reduced by the factor $1/e$ and the difference is converted into heat or other forms of particle acceleration,

$$1 = 2C_K^{3/2} \int_{k_0}^{k_\perp} k_\perp'^{-1} \frac{\overline{\gamma}}{\overline{\omega}_r}(k_\perp') \mathrm{d}k_\perp'. \tag{3.25}$$

Up to this scale, the dissipation term is negligible or small compared to the spectral energy transport. When we assume for mathematical simplicity that the normalized damping rate is in the form of a power-law $\overline{\gamma}/\overline{\omega}_r \propto k_\perp^\zeta$, the integral in Equation (3.25) can be solved analytically,

$$1 = 2C_K^{3/2} \zeta^{-1} \overline{\gamma}/\overline{\omega}_r \tag{3.26}$$

$$\Rightarrow \overline{\gamma}(k_d)/\overline{\omega}_r(k_d) \sim 1. \tag{3.27}$$

Hence, dissipation sets in at a scale $k_d = 1/l_d$, where the damping rate equals the real frequency independently of the energy cascade rate.

The differences of the solar wind dissipation length in comparison to the hydrodynamic dissipation length are sketched in Figure 3.5. The top panels show the hydrodynamic case, and the bottom panels the solar wind case. Panel (a) displays the isotropic energy distribution in hydrodynamic turbulence, and panel (c) shows the anisotropic energy distribution in a magnetized plasma under the assumption of critical balance for different values of ε_0 labeled $\varepsilon_3 > \varepsilon_2 > \varepsilon_1$. Panel (c) shows additionally in red the general intensity of damping for different ε_0 for linear wave mode damping, such as in our KAW model. In a critically balanced turbulence, larger values of ε_0 lead to larger parallel wavenumbers (see (3.18) and (3.20)). The larger parallel wavenumbers at a given perpendicular wavenumber lead to larger damping rates. In contrast, in hydrodynamic turbulence, ε_0 has no influence on the damping rate $\gamma(k) = \nu k^2$. Following Equation (3.12), panels (b) and (d) illustrate schematically the influence of different values of ε_0 ($\varepsilon_2 > \varepsilon_1$) on the energy cascade rate $\varepsilon(k)$ and $\varepsilon(k_\perp)$ for hydrodynamic turbulence and solar wind turbulence, respectively. The dissipation length, marked by the orange dashed lines, is defined as the scale where the energy flux is reduced by a factor of $1/e$. For hydrodynamic turbulence, larger ε_0 leads to a smaller dissipation length, whereas the dissipation length in the solar wind plasma is independent of the energy flux. To explain this difference in detail, we look at the equation that describes the relative change of the energy flux (derived from (3.12)),

$$\frac{1}{\varepsilon(k)} \frac{d\varepsilon(k)}{dk} \propto -\left(\frac{\varepsilon(k)}{\rho}\right)^{-1/3} \gamma(k) k^{-\kappa}. \tag{3.28}$$

For hydrodynamic damping, the relative change of energy flux, i.e., $1/\varepsilon(k)\ d\varepsilon/dk = d/dk\ \ln\varepsilon(k)$ on the left-hand side of (3.28) depends on $\varepsilon(k)^{-1/3}$ and therefore on the energy injection rate ε_0. The energy flux therefore changes depending on how strongly the turbulence is driven. Different ε_0 result in different amplitudes of the power spectrum, as well as in different exponential curves in hydrodynamic turbulence. In the case of solar wind turbulence under the assumption of a critically balanced energy distribution, the situation is different. A larger energy flux leads to

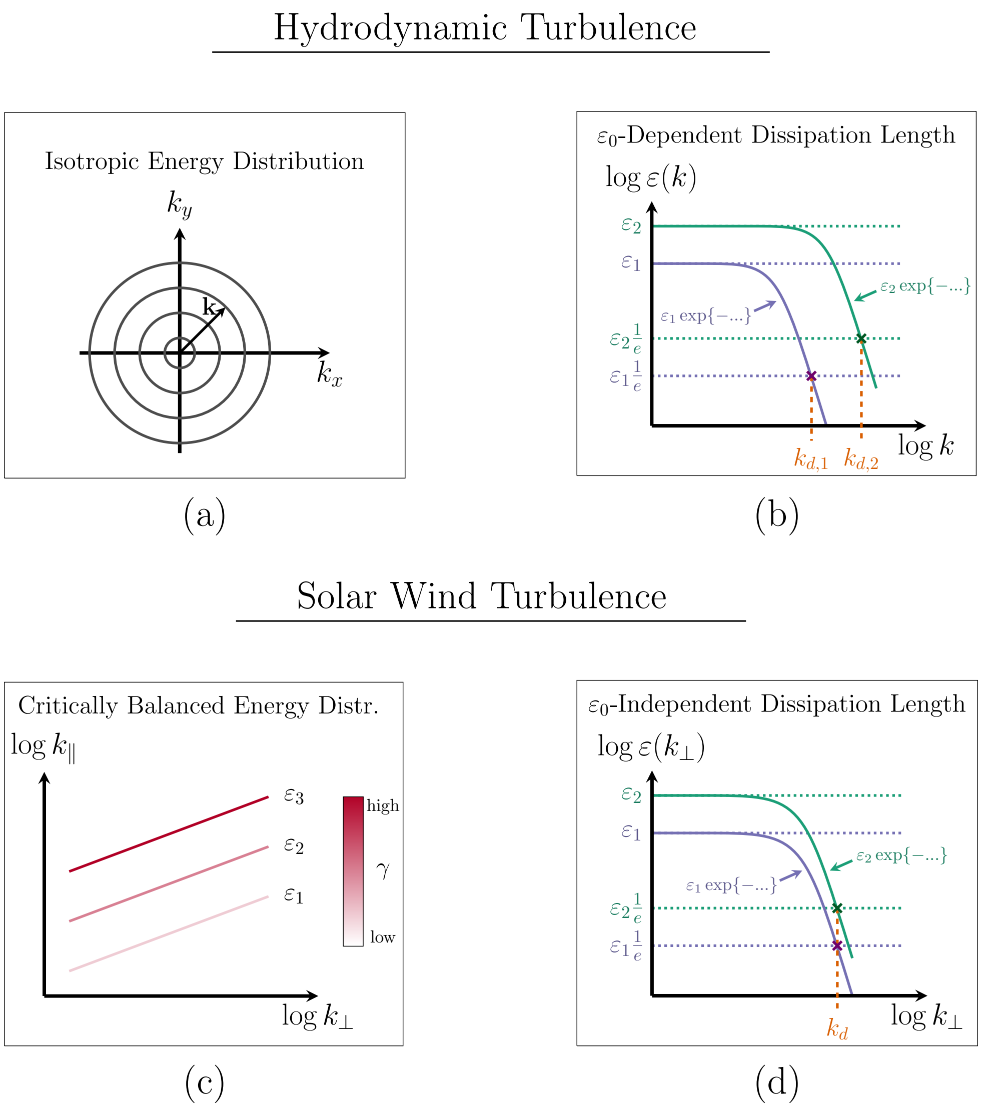
Hydrodynamic Turbulence
Isotropic Energy Distribution
k_y
k
k_x
(a)
ε_0-Dependent Dissipation Length
$\log \varepsilon(k)$
ε_2
ε_1
$\varepsilon_2 \exp\{-...\}$
$\varepsilon_1 \exp\{-...\}$
$\varepsilon_2 \frac{1}{e}$
$\varepsilon_1 \frac{1}{e}$
$k_{d,1}$
$k_{d,2}$
$\log k$
(b)
Solar Wind Turbulence
Critically Balanced Energy Distr.
$\log k_\parallel$
ε_3
ε_2
ε_1
high
γ
low
$\log k_\perp$
(c)
ε_0-Independent Dissipation Length
$\log \varepsilon(k_\perp)$
ε_2
ε_1
$\varepsilon_2 \exp\{-...\}$
$\varepsilon_1 \exp\{-...\}$
$\varepsilon_2 \frac{1}{e}$
$\varepsilon_1 \frac{1}{e}$
k_d
$\log k_\perp$
(d)

Figure 3.5: Sketch of the role of different energy cascade rates on the energy distribution in k-space (left panels) and on the energy flux $\varepsilon(k)$ (right panel) for hydrodynamic turbulence (top panels) and solar wind turbulence (bottom panels). The different values for the energy cascade rate ε_0 are referred to as ε_1, ε_2, ε_3 with $\varepsilon_1 < \varepsilon_2 < \varepsilon_3$. In panel (c), the energy distribution for solar wind turbulence is assumed to follow critical balance, which implies that larger ε_0 result in larger parallel wavenumbers $k_\parallel$. For KAW larger parallel wavenumbers additionally result in larger damping rates γ for the same $k_\perp$. The larger damping rates γ are indicated by the intensity of the red color in panel (c). The dissipation scales k_d shown in orange in panel (b) and (d) are defined as the scales where the energy is reduced by a factor of $1/e$. Figure from Schreiner & Saur (2017).

a modified anisotropic distribution of energy in k-space, i.e., larger parallel wavenumbers $k_\parallel$ for the same perpendicular wavenumber $k_\perp$ (see Figure 3.5 (c)). These larger parallel wavenumbers result in larger damping rates $\gamma \sim k_\parallel v_A \overline{\gamma}(k_\perp) \sim \varepsilon(k_\perp)^{1/3}\overline{\gamma}(k_\perp)$ (see colored lines and related color bar in Figure 3.5 (c)). By insertion of $\gamma(k)$ into Equation (3.28), we see that the right-hand side of (3.28) is independent of the energy flux $\varepsilon(k_\perp)$. Therefore, the relative change of the energy density and the spectral form of the energy density are independent of ε_0. The larger energy flux, which drives the turbulent energy to smaller scales, is compensated by the larger damping rates. This compensation of a larger energy flux by larger damping rates results in the same perpendicular dissipation scale for all values of ε_0 under the assumption $\gamma(k_\perp, k_\parallel) = k_\parallel v_A \overline{\gamma}(k_\perp)$, which is approximately valid in the solar wind (see Figure 3.4). Hence, the independence of the dissipation length from the energy flux, which was observed in Alexandrova et al. (2012), can be explained by KAW damping under the assumption of critically balanced wavenumbers.

In addition to the analysis of dissipation length scales, our model for the power spectral density provides the opportunity to investigate the spectral shape of the dissipation range. There is an ongoing debate whether the dissipation range forms an exponential decay (Alexandrova et al., 2009, 2012) or follows a power-law (Sahraoui et al., 2009, 2012). By looking at Equation (3.14), we formally see that under the assumption of Equation (3.13), any damping rate that is of the form $\gamma = \gamma_0(k_\perp/k_0)^{\kappa-1}$ leads to a power-law dissipation spectrum with a spectral index of $\kappa + 4/3C_K(\varepsilon_0/\rho)^{-1/3}\alpha_0^{-2/3}k_0^{-2/3}\gamma_0$. On the contrary, $\gamma \propto k_\perp^\kappa$ implicates an exact exponential shape of the form $\exp(-l_d k_\perp)$. Note that any deviation of $\gamma \propto k_\perp^{\kappa-1}$ leads to a 'quasi'- exponentially shaped dissipation spectrum. Figure 3.6 shows the damping rates that would result in a power-law (dotted line) or an exact exponentially shaped dissipation range (dashed line) for a spectral index of $\kappa = 7/3$. The KAW damping rate calculated from the hot dispersion relation for plasma parameters from observation 5 in Alexandrova et al. (2009) and for parallel wavenumbers following (3.20) is plotted as a solid line. γ_{KAW} follows approximately $k_\perp^{2.2}$ up to the electron scales and is thus close to the $k_\perp^\kappa$ scaling of the exponentially shaped dissipation spectrum. Hence, we draw the conclusion that damping of KAWs in a KAW driven turbulence leads to a 'quasi'-exponential decay in the dissipation range. At scales

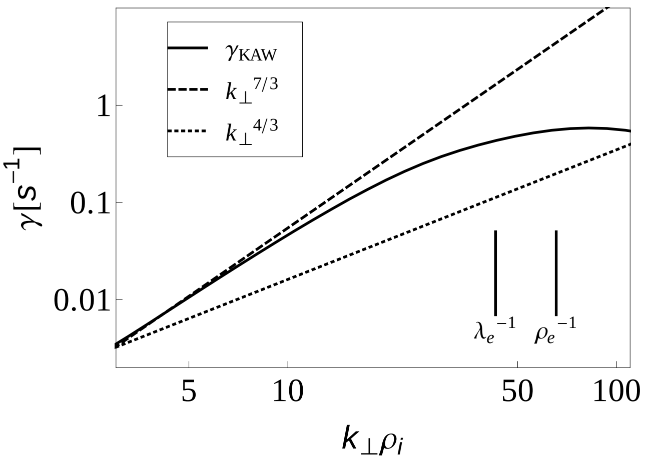

Figure 3.6: The solid line gives the KAW damping rate from Equation (2.32) for the same parameters as in Figure 3.3. $k_\perp^{4/3}$ and $k_\perp^{7/3}$ is shown for comparison. λ_e and ρ_e are marked by the vertical lines. Figure from Schreiner & Saur (2017).

smaller than the electron scales, the damping rate flattens and stays approximately constant. Further observations at sub-electron scales are necessary to see whether the flattening of the KAW damping rate has an influence on the magnetic spectra in this range.

3.4 Comparison with Solar Wind Observations

In this section, first, we quantitatively compare modeled magnetic power spectral densities calculated with hot damping rates and critically balanced wavenumbers with observed solar wind power spectral densities analyzed in Alexandrova et al. (2009). Second, we present a statistical study of modeled power spectral densities for varying solar wind conditions, which we compare with the statistical study of the set of observations analyzed in Alexandrova et al. (2012), with the aim to identify the dissipation length in a KAW driven turbulent cascade.

3.4.1 Comparison with Exemplary Magnetic Power Spectrum

We present the first comparison of a dissipation model with a measured magnetic power spectrum at electron scales. The blue dots in Figure 3.7 show observed power spectral densities analyzed in Alexandrova et al. (2009) with $B = 15.5\,\mathrm{nT}$, $n = 20\,\mathrm{cm}^{-3}$, $T_i = 61\,\mathrm{eV}$, $T_e = 26\,\mathrm{eV}$, $v_{SW} = 630\,\mathrm{km/s}$, and an angle between the mean magnetic field and the solar wind velocity of $\theta_{\mathbf{vB}} = 83°$. For low frequencies the spectrum follows $\sim f^{-1.7}$ in agreement with Kolmogorov's law and steepens on ion scales to $\sim f^{-2.8}$. Around the electron scales, the spectrum follows approximately an exponential function (Alexandrova et al., 2009). Our model spectrum is shown in brown with $\kappa = 2.7$ for scales below ion scales, where we have applied Taylor's hypothesis to convert wavevector spectra into frequency spectra using $f = k_\perp v_{SW}/2\pi$. Apart from the spectral index κ, and the Kolmogorov constant C_K, our model equation has no other free parameters. In the ranges of $\kappa = [2.2, 2.8]$ and $C_K = [1.4, 2.1]$, we find through the calculation of the root-mean-square error that the model with $\kappa = 2.7$ and $C_K = 1.4$ describes the data best, but combinations of $\kappa = [2.5, 2.7]$ and $C_K = [1.4, 1.8]$ lead to similar spectral densities within a root-mean-square error difference of 10%. For the choice of the Kolmogorov constant, we follow Biskamp (1993). We discuss the influence of C_K on energy spectra in Section 3.5. Deviations from the theoretically expected value of $\kappa = 7/3 \approx 2.33$ for KAW (Howes et al.,

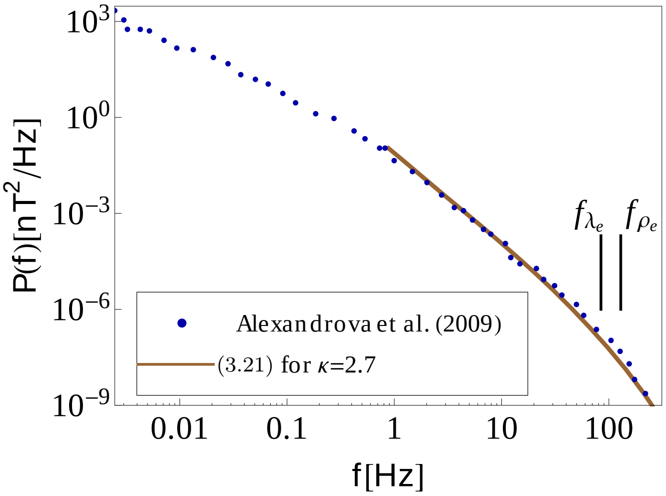

Figure 3.7: Equation (3.21) for the same parameters as in Figure 3.3 in the brown line. Observations from interval 5 in Alexandrova et al. (2009) are shown in blue dots. Vertical lines indicate the electron scales, where f_{λ_e} corresponds to the Doppler-shifted λ_e with $f_{\lambda_e} = v_{SW}/2\pi\lambda_e$, and f_{ρ_e} to ρ_e with $f_{\rho_e} = v_{SW}/2\pi\rho_e$. Figure from Schreiner & Saur (2017).

2006; Schekochihin et al., 2009) may be a result of intermittency effects (Salem et al., 2009; Lion et al., 2016) or superimposition of whistler wave fluctuations (Lacombe et al., 2014). Additionally, damping at electron scales results in spectral indices steeper than 7/3 due to ‘sampling’ effects of one-dimensional spacecraft measurements. Several different wavevectors contribute to the power spectral density at a certain spacecraft frequency, so that the sub-ion range is already affected by electron damping (von Papen & Saur, 2015). This influence is analyzed in Chapter 4, where we compare reduced power spectra obtained with the model presented in von Papen & Saur (2015) with solar wind measurements. In order to take account of the mentioned effects, we use a spectral index which fits best to the data. The model spectrum follows in agreement with the observations a power-law at the large scales and forms a ‘quasi’-exponential decay at electron scales. Hence, the observed exponential form of the dissipation range in the observations seems to be compatible with electron Landau damping of kinetic Alfvén waves at least for this set of observations.

3.4.2 Statistical Analysis

For further insight into the spectral behavior for varying solar wind parameters, we perform a statistical study with our model similar to the statistical study of 100 observed spectra by Alexandrova et al. (2012). As presented in 2.2.3, they fit an exponential function

$$P_A(k_\perp) = A k_\perp^{-\alpha_A} \exp(-k_\perp l_d) \tag{3.29}$$

to the observed power spectral densities. Here we use the same parameter ranges as the observed ones for the magnetic fields, the temperature ratios and the number densities: $B \in [2, 20]$ nT, $T_i/T_e \in [0.5, 5]$ and $n_i = n_e \in [3, 60]$ cm^{-3}. The results of fitting Equation (3.29) to our model through a least mean square fit are shown in Figures 3.8 (a) and 3.8 (b). The dissipation length l_d is shown as a function of (a) the electron gyroradius ρ_e and (b) the electron inertial length λ_e. The red dots show the results for a wide range of ion and electron plasma betas ($\beta_i \in [0.1, 10]$ and $\beta_e \in [0.1, 20]$), the black and blue dots show separated results for small ($\beta_i, \beta_e \in [0.1, 1]$) and large plasma betas ($\beta_i \in [1, 10]$ and $\beta_e \in [1, 20]$), respectively. For every

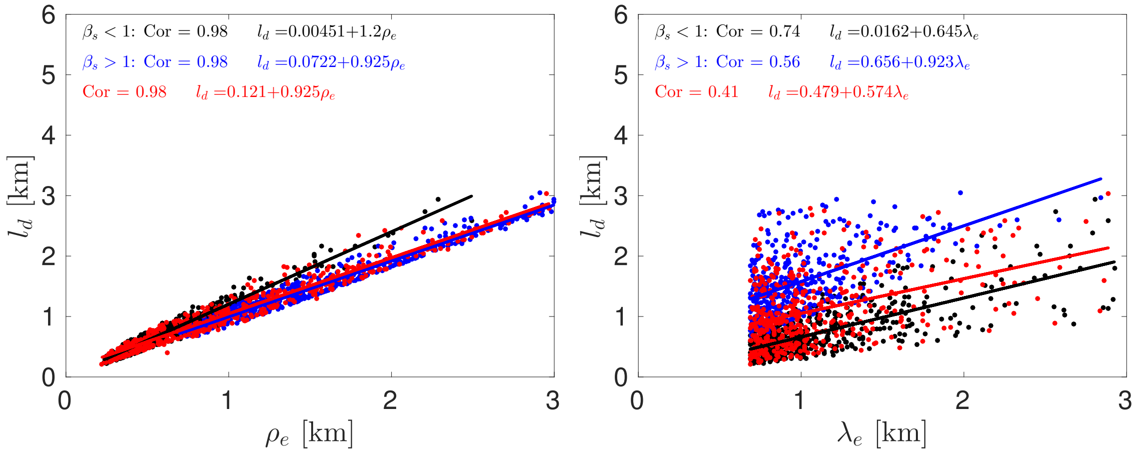

(a) (b)

Figure 3.8: Results of fitting Equation (3.29) to 300 model spectra with hot damping rates. The dissipation length l_d is shown as a function of (a) the electron gyroradius ρ_e, and (b) the electron inertial length λ_e. The red dots show the results for $\beta_i = [0.1, 10]$ and $\beta_e = [0.1, 20]$; the black and blue dots show separated results for small ($\beta_i, \beta_e = [0.1, 1]$) and large plasma betas ($\beta_i = [1, 10]$ and $\beta_e = [1, 20]$), respectively. Figure from Schreiner & Saur (2017).

model spectrum, the parameters are chosen randomly within the given parameter ranges using logarithmic distributed values for the temperature ratio and the plasma beta and linear distributed values for the others. We find a high correlation for the electron gyroradius of 0.98 and a dissipation length $l_d \sim 0.9\rho_e$, which is similar to the observed value by Alexandrova et al. (2012). Also in agreement with the observational study by Alexandrova et al. (2012), Figure 3.8 (b) shows a much weaker correlation of 0.41 between the dissipation length l_d and the electron inertial length λ_e. This correlation is mainly due to intervals, where $\beta_e \approx 1$, which means that the inertial length is comparable to the gyroradius. Another possible explanation is that also the inertial length is related to the dissipation scale for some solar wind conditions. For example, for small electron plasma betas and low temperatures the electron gyroradius is very small. In this case, the turbulence might dissipate on an alternative scale, e.g., the electron inertial length, which is reached first by the turbulent cascade. In order to look into this hypothesis, we analyze the dissipation length separately for small (black line) and large plasma betas (blue line). Indeed, the correlation between the dissipation length and the electron inertial length is higher for small plasma betas with a correlation coefficient of 0.74 than for large plasma betas with a correlation coefficient of 0.56. Additionally, the estimated dissipation length in the case of small plasma betas ($l_d \sim 1.2\rho_e$) is slightly larger than in the large beta case ($l_d \sim 0.9\rho_e$) suggesting that the energy is dissipated at scales larger than the electron gyroradius.

The key results of the study in this chapter are as follows: under the assumption of a critically balanced wavenumber distribution, the real part of the wave frequency does not exceed the ion gyrofrequency due to the influence of the dissipation rate on the parallel wavenumber. Therefore, we conclude that the turbulence is driven by KAWs rather than whistler waves. Additionally, owing to the low-frequency nature of KAWs, Taylor's hypothesis is valid in the solar wind for a KAW driven turbulence. Our dissipation model provides an explanation for the surprising independence of the dissipation scale from the energy flux, which is a remarkable difference compared to hydrodynamic turbulence. This difference is a result of the anisotropic nature of the plasma turbulence, i.e., due to a combination of critically balanced turbulence and a dispersion relation proportional to the parallel wavenumber. The critical balance assumption influences the energy cascade in such a way that the more energy is injected at the turbulence driving scales, the more effective the damping rate gets. Analysis of the KAW damping rate shows that KAW damping leads to a 'quasi'-exponentially shaped dissipation range, which is in agreement with the observations in Alexandrova et al. (2009, 2012). Still, additional wave modes, which change the damping rate or the energy transport could explain the observed power-law dissipation range in Sahraoui et al. (2009, 2013). The statistical study reveals that the electron gyroradius acts as a dissipation scale in a KAW driven turbulent cascade, which is in agreement with the findings in Alexandrova et al. (2012).

3.5 Discussion

Here we discuss a number of assumptions that have been made in the derivation of our solar wind dissipation model. A range of the Kolmogorov constant $C_K = [1.4, 2]$ in the solar wind was determined from experimental data and nonlinear simulations

(Biskamp, 1993). In our study, the Kolmogorov constant is taken to be $C_K = 1.4$ in both the MHD and the kinetic regime. However, the 'constant' may depend on plasma parameters or the wavenumber. For higher values of C_K, the argument of the exponential damping term in Equation (3.21) is larger, and therefore, the effect of damping is increased in comparison to the nonlinear energy transport. This variation of the Kolmogorov constant leads to an uncertainty in the magnetic power spectral density, but without any influence on the general physical description.

We assume critical balance to obtain the anisotropy of the energy cascade to smaller scales. This assumption is valid only for strong turbulence. On the contrary, in the description of weak turbulence, there is no transport of energy in the parallel direction (Sridhar & Goldreich, 1994). However, with increasing $k_\perp$, the nonlinear interactions become so strong that the assumption of weakness is no longer valid. Hence, the turbulence is either already strong from the beginning or will eventually become strong for increasing $k_\perp$. Yet our model is not able to handle a changing from strong to weak turbulence when the collisionless damping reduces the amplitudes of the nonlinear interactions to a limit, where weak turbulence should be applied (see Howes et al. (2011) for a weakened cascade model). This strong turbulence results in a decrease of parallel wavenumbers for large perpendicular wavenumbers where the damping is high as shown in Figure 3.3, although a constant value of the parallel wavenumber would be physically more reasonable in this range. Hence, the dissipation model can not be applied to scales smaller than electron scales.

Our dissipation model is a linear model in the sense that it linearly combines the nonlinear cascade towards smaller length scales and a process transferring magnetic field energy to particle energy. The mutual feedback of these processes might become stronger at small scales, where the dissipation rates become strong. However, we expect our model to still capture important aspects of the physics around electron scales. In our model we neglect physics on scales significantly beyond the electron scales, e.g., a possible third electrostatic turbulent cascade (Schekochihin et al., 2016).

The dissipation model presented here is similar to two earlier models, which also contain a nonlinear energy cascade and collisionless damping. Podesta et al. (2010) computed numerically the damping rate from the hot plasma dispersion relation.

They conclude that a KAW energy cascade is almost completely dissipated before reaching the electron scales due to strong Landau damping. This would imply that the energy cascade to the electron scales must be supported by wave modes other than the KAW. Howes et al. (2011) argued that they underestimated the weight of the nonlinear energy cascade in comparison to the dissipation (here described by C_K), leading to overestimated damping rates. The cascade model in Howes et al. (2008) employs the damping rates obtained from gyrokinetic theory. The authors find in agreement to our results an exponential shaped dissipation range for moderate damping with $\beta_i = 1$ for $T_i/T_e = 1$. For strong damping ($\beta_i = 0.01$ and $T_i/T_e = 1$) the spectra show sharp cut offs. In Howes et al. (2011) it is assumed that in a model with only local interactions the damping dominates over the energy transfer in the case of strong damping. Therefore, they constructed a weakened cascade model with nonlocal interactions. Following Schekochihin et al. (2009), damping can be considered strong if the decay time $1/\gamma$ is shorter or comparable to the wave period $2\pi/\omega_r$. Figure 3.1 shows that damping at $k_\perp \rho_i = 1$ is relatively weak for typical solar wind parameters ($\beta_i \gtrsim 1$, $T_i/T_e \approx [0.5, 5]$); thus, the nonlocal effects should play a minor role in interpreting the observed energy spectra.

For mathematical simplicity, we solve the hot plasma dispersion relation assuming Maxwellian distributions of protons and electrons with no temperature anisotropies. Observations of particle distributions show deviations from a Maxwellian due to the weakly collisional nature of the solar wind (Hundhausen et al., 1970; Feldman et al., 1973; Goodrich & Lazarus, 1976). Measured electron distribution functions are composed of an almost Maxwellian and isotropic core for electrons with energy below 50 eV and a highly anisotropic halo representing electrons of higher energy (Briand, 2009). Likewise, observations of proton distribution functions indicate anisotropies between the temperatures parallel and perpendicular to the magnetic field and bump-like deformations at high energy (Marsch et al., 1982). However, due to instabilities limiting the scope of the deformations, the measured deformation of the thermal distribution function is not as strong as expected (Briand, 2009).

Although turbulence is a nonlinear phenomenon, we assume that turbulent fluctuations are represented by superposition of linear wave modes and that the energy is transported to smaller scales by nonlinear interactions of these linear wave modes.

Consequently, the turbulent dissipation is quantified in our model by the imaginary part of the wave frequency obtained from the linearized Maxwell-Vlasov system. In the case of weak turbulence, the nonlinear term $(\mathbf{z}^{\mp} \cdot \nabla)\mathbf{z}^{\pm}$ in Equation (2.25) is indeed only a small perturbation to the linear system, so that the fluctuations do not significantly change within each interaction. In strong turbulence, due to critical balance, the nonlinear term $(\mathbf{z}^{\mp} \cdot \nabla)\mathbf{z}^{\pm}$ is comparable to the linear term $(\mathbf{v}_A \cdot \nabla)\mathbf{z}^{\pm}$ in Equation (2.25), so that the fluctuations fully decay in one interaction. Hence, the linear term still contributes to the response of the plasma, even in the presence of strong non-linearities (Howes et al., 2014). Therefore, at least some properties of the linear wave modes may be retained within the turbulent cascade. In fact, solar wind observations show that some properties of linear wave modes are still present, even in strong turbulence, which justifies the linear approach (e.g. Belcher & Davis, 1971; Bale et al., 2005; He et al., 2011; Howes et al., 2012).

As mentioned in 3.4.1, we relate wavenumbers and frequencies by $f = k_{\perp} v_s / 2\pi$. Thus, we do not take into account the sampling effect, where different wavevectors contribute to the power spectral density at a given frequency in the spacecraft frame. In the analyzed power spectrum in 3.4.1, the field-to-flow angle is 83° and therefore, the sampling effect is relatively unimportant, at least in the electron dissipation range. In the next chapter, we compare our dissipation model to a set of 93 solar wind observations with field-to-flow angles varying from 50° to 90°. For small field-to-flow angles the sampling effect becomes more important. On this account, we extend our dissipation model to three dimensions and apply the associated energy distribution to the model by von Papen & Saur (2015) aiming to explain the spectral index in the sub-ion range, which is steeper than KAW theory suggests.

4 Model for Reduced Power Spectra in Frequency Space

As Equation (2.40) reveals, in situ observations of magnetic fluctuations are obtained in an one-dimensional form in the spacecraft frame, where several different wavevectors contribute to the power spectral density at a certain spacecraft frequency, which is called sampling effect (von Papen & Saur, 2015). Therefore, it is not possible to derive the three-dimensional energy distribution in wavenumber space uniquely from the measured reduced power spectrum. However, one can obtain the reduced power spectrum numerically based on a given energy distribution in wavenumber space. In this chapter, first, we present the model by von Papen & Saur (2015), which calculates reduced power spectra for any given energy distribution. Second, we derive the extension of the one-dimensional model to three dimensions to obtain the three-dimensional energy distribution under the assumption of critically balanced wavenumbers and damping by KAWs. Based on this energy distribution, we calculate reduced power spectra in frequency space for varying solar wind conditions. We compare the reduced power spectra to a set of 93 solar wind observations analyzed in Alexandrova et al. (2012) to study the influence of KAW damping on the spectral index in the sub-ion range. Finally, we discuss the assumptions and limitations of our approach.

4.1 Calculation of Reduced Power Spectra According to the Forward Modeling Approach by von Papen & Saur (2015)

Here, we present the forward modeling approach by von Papen & Saur (2015) for the calculation of the reduced power spectra from a given three-dimensional energy distribution in k-space. Under the assumption of axisymmetry along the mean magnetic field, passively cascading poloidal fluctuations, i.e., the pseudo-Alfvén mode in the MHD regime, which is the incompressible limit of the slow mode, Taylor's hypothesis, and statistical homogeneity, the reduced power spectral density in frequency space $P(f)$ can be obtained by an integration over a plane perpendicular to the flow direction $\mathbf{v}_{SW}$ of the three-dimensional energy density $E(\mathbf{k})$,

$$P(f) = \int_{-\infty}^{\infty} \mathrm{d}^3 k E(\mathbf{k}) \delta(2\pi f - k_x v_{SW} \sin(\theta_{\mathbf{vB}}) - k_z v_{SW} \cos(\theta_{\mathbf{vB}})), \tag{4.1}$$

in a coordinate system, where the z-axis is aligned with the mean magnetic field, the x-axis is in the plane defined by the mean magnetic field and the solar wind direction, and the y-axis completes the right-handed system. $\theta_{\mathbf{vB}}$ defines the angle between the mean magnetic field and the solar wind direction. Based on a model for the turbulent energy transport by Goldreich & Sridhar (1995) and models for critical balance in the MHD regime $k_\parallel \sim L^{-1/3} k_\perp^{2/3}$ with $k_\perp \rho_i \ll 1$, in the kinetic regime $k_\parallel \sim L^{-1/3} \rho_i^{-1/3} k_\perp^{1/3}$ with $k_\perp \rho_i \geq 1$, and in the electron dissipation regime $k_\parallel \sim L^{-1/3} \rho_i^{-1/3} \rho_e^{-1/3}$ with $k_\perp \rho_e \geq 1$, von Papen & Saur (2015) derive the three-dimensional spectral energy density as follows,

$$E_{\mathrm{MHD}}(\mathbf{k}) = \left(\frac{B_0^2}{L^{1/3}} \right) k_\perp^{-10/3} \exp\left(-L^{1/3} \frac{|k_\parallel|}{k_\perp^{2/3}} \right), \tag{4.2}$$

$$E_{\mathrm{KAW}}(\mathbf{k}) = \left(\frac{B_0^2}{L^{1/3} \rho_i^{1/3}} \right) k_\perp^{-11/3} \exp\left(-L^{1/3} \rho_i^{1/3} \frac{|k_\parallel|}{k_\perp^{1/3}} \right), \tag{4.3}$$

$$E_{\mathrm{ED}}(\mathbf{k}) = \left(\frac{B_0^2}{L^{1/3} \rho_i^{1/3}} \right) k_\perp^{-11/3} \exp\left(-L^{1/3} \rho_i^{1/3} \rho_e^{1/3} |k_\parallel| \right), \tag{4.4}$$

where L defines the outer scale, where the turbulent energy is injected isotropically, and B_0 defines the mean magnetic field. The critical balance in the MHD regime and the kinetic regime is in agreement with the critical balance of our one-dimensional model without dissipation in (3.20). The critical balance in the electron dissipation regime describes the influence of dissipation on the parallel wavenumber phenomenologically. E_{MHD} defines the energy distribution in the MHD regime and satisfies $P(f) \propto f^{-5/3}$ for $\theta_{\mathbf{vB}} = 90^\circ$ and $P(f) \propto f^{-2}$ for $\theta_{\mathbf{vB}} = 0^\circ$. The energy distribution changes at $k_\perp \rho_i = 1$ to the energy distribution in the kinetic regime

E_{KAW}, where the authors assume a KAW driven energy cascade, which scales with $P(f) \propto f^{-7/3}$ for $\theta_{\mathbf{vB}} = 90°$. The energy density changes again at $k_\perp\rho_e$, where the dissipation weakens the turbulent cascade, so that there is no energy transfer in the parallel direction anymore. In 3.3, we show that our model is not able to handle the changing from strong to weak turbulence and that the parallel wavenumber decreases in our model for strong damping. Hence, the calculated damping rates from the hot plasma dispersion relation are not consistent with the calculation of the energy distribution in the electron dissipation regime. However, we expect that the decreasing parallel wavenumber has a negligible effect on the reduced power spectra, because we use damping rates normalized by the parallel wavenumber.

Figure 4.1 shows logarithmically equidistant iso-contours of the resultant energy distribution as a function of k_x, which is one of the perpendicular directions with

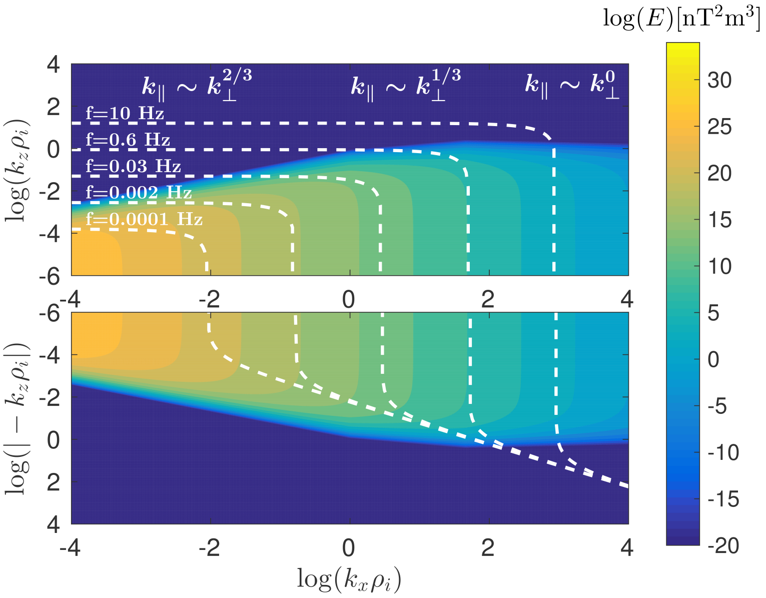

Figure 4.1: Double logarithmic plot of the energy density as logarithmically equidistant iso-contours calculated with Equations (4.2)-(4.4). A very similar figure can be found in von Papen & Saur (2015), however, for better comparison with the energy distribution with damping, we generated the figure with the following parameters: $B = 5.7\,\mathrm{nT}$, $L = 6 \times 10^9\,\mathrm{m}$, $\rho_i = 10^5\,\mathrm{m}$, $\rho_e = 2.2 \times 10^3\,\mathrm{m}$, $v_{SW} = 4 \times 10^5\,\mathrm{m/s}$, $v_A = 2.5 \times 10^4\,\mathrm{m/s}$. Integration planes according to (4.1) are shown as white dashed lines for a field-to-flow angle of 1° for logarithmically equidistant frequencies between $10^{-4}\,\mathrm{Hz}$ and $10\,\mathrm{Hz}$.

respect to the magnetic field, and k_z, which is the parallel direction, normalized by the ion gyroradius ρ_i in a double logarithmic plot. The critical balance path, $k_\parallel = k_\perp^{e_{CB}}$ with the critical balance exponent e_{CB}, in the three different regimes, MHD, KAW, and electron dissipation, can be seen as the boundary where the energy becomes negligibly small. Figure 4.1 demonstrates that the whole area below the critical balance path is filled with energy, which decreases exponentially in the parallel direction. In our one-dimensional model, we assume that the energy is only distributed along the critical balance path. Integration planes according to Equation (4.1) are shown in the white dashed lines for a field-to-flow angle of 1° for different frequencies. The integration planes for a field-to-flow angle of 90° would be vertical; for 0° they would be horizontal.

Power spectral densities calculated with (4.1) for the energy distribution shown in Figure 4.1 for different field-to-flow angles are displayed in Figure 4.2. As expected from theoretical predictions and as seen in many observations, the spectral slope for $\theta_{\mathbf{vB}} = 90°$ follows $f^{-5/3}$ in the MHD regime and transitions to $f^{-7/3}$ in the kinetic regime. In the electron dissipation regime, the spectrum follows $f^{-8/3}$ due to the chosen critical balance $k_\parallel \propto k_\perp^0$. Figure 4.2 demonstrates the so-called sampling

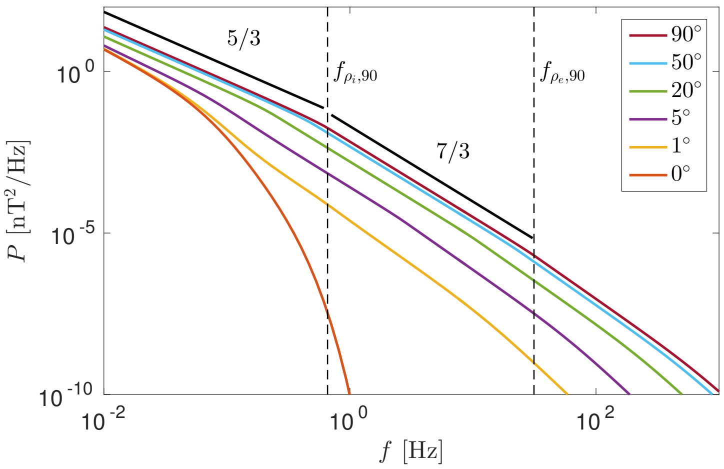

Figure 4.2: Power spectral densities for different field-to-flow angles in the MHD, KAW, and electron dissipation regime. The Doppler-shifted ion gyroradius and electron gyroradius for a field-to-flow angle of 90° are shown in the black dashed vertical lines. Power-laws with a spectral index of 5/3 and 7/3 are shown for comparison.

effect, which is described in detail in von Papen & Saur (2015): The power spectra for field-to-flow angles of 1° to 90° exhibit a power-law close to $f^{-7/3}$ in the KAW regime and $f^{-8/3}$ in the electron dissipation regime. This effect can be explained by looking at the integration planes in Figure 4.1. Already for a field-to-flow angle of 1°, most of the integrated energy stems from the perpendicular part of the integration (vertical lines), especially for high frequencies. Therefore, without dissipation, spectral indices of 7/3 should be observed in the sub-ion range for all field-to-flow angles. However, as presented in 2.2.3, observed power spectral densities in the solar wind show spectral indices between 2.3-2.9 in the sub-ion range. In the following, we extend our one-dimensional dissipation model to three dimensions to obtain the three dimensional energy distribution with damping and analyze the influence of the sampling effect in combination with KAW damping on the spectral slope in the sub-ion range.

4.2 Extension of One-Dimensional Dissipation Model to Three Dimensions

In this section, we derive the equation for the three-dimensional energy density analogously to the equation for the one-dimensional energy density. Although some of the equations are identical to the equations in Chapter 3, we repeat them here for better understanding. A sketch of the energy distribution and the energy transfer in three-dimensional k-space is shown in Figure 4.3. We assume that the energy density is a function of the perpendicular wavenumber only, $E(\mathbf{k}) = E(k_\perp)$, i.e., the energy density is constant over the red shells with radius $k_\perp$ and constant along $k_\parallel$. Following Kolmogorov, we write the energy flux $\varepsilon(k_\perp)$ in the perpendicular direction as

$$\varepsilon(k_\perp) = C_K^{3/2} E(k_\perp) v_k(k_\perp) S_k(k_\perp), \tag{4.5}$$

where $E(k_\perp)$ defines the three-dimensional power spectral density of magnetic fluctuations in $\mathrm{nT^2m^3}$, C_K the Kolmogorov constant, v_k the eddy-decay velocity and $S_k(k_\perp) = 2\pi k_\perp k_\parallel$ the k-space surface of the shell at $k_\perp$. Analogous to the one-dimensional model, the eddy-decay velocity is related to the velocity fluctuations

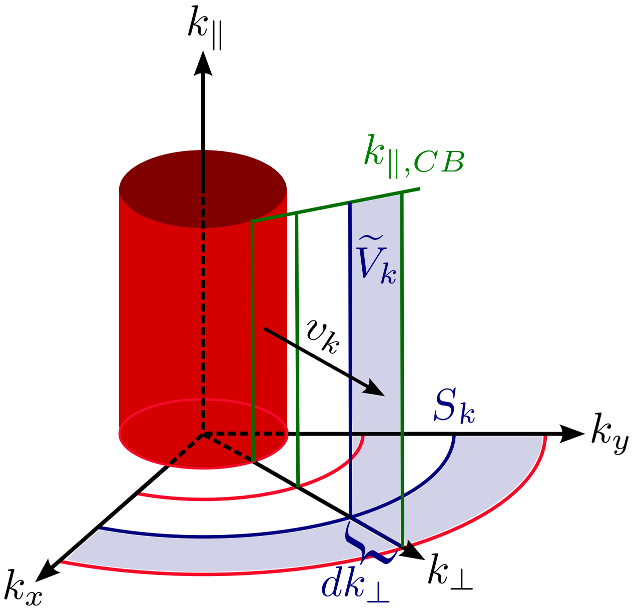

Figure 4.3: Sketch of energy distribution in k-space. The energy is constant over red shells with radius $k_\perp$ and constant along $k_\parallel$. The energy is transported in the perpendicular direction with velocity v_k and distributed in the parallel direction following critical balance. S_k defines the surface of the shell and $\widetilde{V}_k$ the approximate volume between two shells with radius $k_\perp$ and $k'_\perp = k_\perp + \mathrm{d}k_\perp$.

$v_\perp(k_\perp)$ by

$$v_k(k_\perp) = k_\perp^2 v_\perp(k_\perp), \tag{4.6}$$

and the ratio α of magnetic and velocity fluctuations is given by

$$v_\perp(k_\perp) = \alpha\sqrt{\frac{E(k_\perp)S_k(k_\perp)k_\perp}{\rho}}. \tag{4.7}$$

From (4.5), (4.6), and (4.7), we obtain

$$E(k_\perp)S_k(k_\perp) = C_K\rho^{1/3}\varepsilon(k_\perp)^{2/3}\alpha(k_\perp)^{-2/3}k_\perp^{-5/3}. \tag{4.8}$$

Assuming α to follow a power-law, $\alpha = \alpha_0(k/k_0)^\beta$, we write $E(k_\perp)S_k(k_\perp)$ analogously to $P(k_\perp)$ in the one-dimensional model as

$$E(k_\perp)S_k(k_\perp) = E_0 S_{k0} \left(\frac{\varepsilon(k_\perp)}{\varepsilon_0}\right)^{2/3} \left(\frac{k_\perp}{k_0}\right)^{-\kappa}, \tag{4.9}$$

with $\kappa = 2/3\beta + 5/3$. With (4.5) and (4.9), the eddy-decay velocity can be written as

$$v_k(k_\perp) = v_{k0} \left(\frac{\varepsilon(k_\perp)}{\varepsilon_0}\right)^{1/3} \left(\frac{k_\perp}{k_0}\right)^{\kappa}. \tag{4.10}$$

The energy flux at wavenumber $k' = k + \mathrm{d}k$ differs from the energy flux at wavenumber k by the part of energy $D(k_\perp, k_\parallel)\widetilde{V}_k(k_\perp)$ that is dissipated in the k-space volume $\widetilde{V}_k = 2\pi k_\perp k_\parallel \mathrm{d}k_\perp$,

$$C_K^{-3/2} E(k_\perp) v_k(k_\perp) S_k(k_\perp) = C_K^{-3/2} E(k'_\perp) v_k(k'_\perp) S_k(k'_\perp) + D(k_\perp, k_\parallel)\widetilde{V}_k(k_\perp). \tag{4.11}$$

Similar to our one-dimensional model, we write the heating rate $D(k_\perp, k_\parallel)$ as

$$D(k_\perp, k_\parallel) = 2\gamma(k_\perp, k_\parallel) E(k_\perp), \tag{4.12}$$

with the damping rate γ. As shown in 3.3, $\gamma(k_\perp, k_\parallel) = k_\parallel v_A \overline{\gamma}(k_\perp)$ with $\overline{\gamma} = \gamma / k_\parallel v_A$ is a valid assumption for typical solar wind conditions. The maximum value of the parallel wavenumber $k_{\parallel,\mathrm{CB}}$ at a certain perpendicular wavenumber $k_\perp$ is defined by critical balance, which can be derived in the same way as was done in the one-dimensional model by combining (4.5), (4.6), and (4.8),

$$k_{\parallel,\mathrm{CB}}(k_\perp) = C_K^{1/2} (v_A \overline{\omega}_r)^{-1} \left(\frac{\varepsilon(k_\perp)}{\rho}\right)^{1/3} \alpha(k_\perp)^{2/3} k_\perp^{2/3}. \tag{4.13}$$

The mean value of the parallel wavenumber as a function of the perpendicular wavenumber is obtained by an integration over $k_\parallel$,

$$k_\parallel(k_\perp) = \frac{1}{k_{\parallel,\mathrm{CB}} - k_{\parallel,0}} \int_{k_{\parallel,0}}^{k_{\parallel,\mathrm{CB}}} \mathrm{d}k_\parallel. \tag{4.14}$$

With $k_{\|,0} \ll k_{\|,\mathrm{CB}}$, the dissipation term can be written as

$$D(k_\perp) = k_{\|,\mathrm{CB}}(k_\perp) v_A \overline{\gamma}(k_\perp) E(k_\perp). \tag{4.15}$$

In the following, the subscript 'CB' will be dropped. Taylor expansion of (4.11) results in a differential equation for the energy density,

$$\begin{aligned}\frac{\mathrm{d}E(k_\perp)}{\mathrm{d}k_\perp} = -E(k_\perp) \Bigg(& \frac{1}{v_k(k_\perp)} \frac{\mathrm{d}v_k(k_\perp)}{\mathrm{d}k_\perp} + \frac{1}{S_k(k_\perp)} \frac{\mathrm{d}S_k(k_\perp)}{\mathrm{d}k_\perp} \\ & + C_k^{3/2} k_\| v_A \overline{\gamma}(k_\perp) \frac{1}{v_k(k_\perp)} \Bigg), \end{aligned} \tag{4.16}$$

with

$$\frac{1}{v_k(k_\perp)} \frac{\mathrm{d}v_k(k_\perp)}{\mathrm{d}k_\perp} = \frac{3}{2} \frac{\kappa}{k_\perp} + \frac{1}{2} \frac{1}{E(k_\perp)} \frac{\mathrm{d}E(k_\perp)}{\mathrm{d}k_\perp} + \frac{1}{2} \frac{1}{S_k(k_\perp)} \frac{\mathrm{d}S_k(k_\perp)}{\mathrm{d}k_\perp}, \tag{4.17}$$

and

$$\begin{aligned}\frac{1}{S_k(k_\perp)} \frac{\mathrm{d}S_k(k_\perp)}{\mathrm{d}k_\perp} = (1 + \frac{2}{3}) k_\perp^{-1} + \frac{1}{3} \frac{1}{\varepsilon(k_\perp)} \frac{\mathrm{d}\varepsilon(k_\perp)}{\mathrm{d}k_\perp} + \frac{2}{3} \frac{1}{\alpha(k_\perp)} \frac{\mathrm{d}\alpha(k_\perp)}{\mathrm{d}k_\perp} \\ - \frac{1}{\overline{\omega}_r(k_\perp)} \frac{\mathrm{d}\overline{\omega}_r(k_\perp)}{\mathrm{d}k_\perp}. \end{aligned} \tag{4.18}$$

The solution of (4.16) gives an equation for the energy density $E(k_\perp)$

$$\begin{aligned} E(k_\perp) = E_0 \left(\frac{k_\perp}{k_0} \right)^{-\kappa - 5/3} \left(\frac{\varepsilon(k_\perp)}{\varepsilon_0} \right)^{-1/3} \left(\frac{\alpha(k_\perp)}{\alpha_0} \right)^{-2/3} \frac{\overline{\omega}_r(k_\perp)}{\overline{\omega}_{r,0}} \\ \times \exp \left(-\frac{2}{3} C_K^{3/2} \int_{k_0}^{k_\perp} \mathrm{d}k'_\perp \frac{\overline{\gamma}(k'_\perp)}{\overline{\omega}_r(k'_\perp)} k'^{-1}_\perp \right). \end{aligned} \tag{4.19}$$

Equating (4.9) with (4.19) leads to an equation for the energy flux $\varepsilon(k_\perp)$

$$\varepsilon(k_\perp) = \varepsilon_0 \exp \left(-\frac{1}{2} C_K^{3/2} \int_{k_0}^{k_\perp} \mathrm{d}k'_\perp \frac{\overline{\gamma}(k'_\perp)}{\overline{\omega}_r(k'_\perp)} k'^{-1}_\perp \right). \tag{4.20}$$

Combining (4.20) and (4.19) and assuming $\alpha(k_\perp) \approx \overline{\omega}_r$ (Howes et al., 2008) yields

$$E(k_\perp) = E_0 \left(\frac{k_\perp}{k_0}\right)^{-\kappa-5/3} \left(\frac{\overline{\omega}_r(k_\perp)}{\overline{\omega}_{r,0}}\right)^{1/3} \times \exp\left(-\frac{1}{2}C_K^{3/2} \int_{k_0}^{k_\perp} \mathrm{d}k'_\perp \frac{\overline{\gamma}(k'_\perp)}{\overline{\omega}_r(k'_\perp)} k'^{-1}_\perp\right). \tag{4.21}$$

In the MHD regime ($\kappa = 5/3$, $\overline{\omega}_r(k_\perp)/\overline{\omega}_{r,0} = 1$), (4.21) can be written as

$$E_{\mathrm{MHD,D}}(k_\perp) = \frac{B_0^2}{L^{1/3}} k_\perp^{-10/3} \exp\left(-\frac{1}{2}C_K^{3/2} \int_{k_0}^{k_\perp} \mathrm{d}k'_\perp \frac{\overline{\gamma}(k'_\perp)}{\overline{\omega}_r(k'_\perp)} k'^{-1}_\perp\right), \tag{4.22}$$

where $B_0^2/L^{1/3} = E_0 k_0^{10/3}$ with the mean magnetic field B_0 and the outer scale L. We determine the outer scale by $L = 2\pi\rho_i/10^{-4}$ (Howes, 2015). The energy distribution in the kinetic regime $E_{\mathrm{KAW,D}}(k_\perp)$ is equal to the energy distribution in the MHD regime at $k_\perp \rho_i = 1$. From this equality, we obtain

$$E_{0,\mathrm{KAW}} = E_0 \left(\frac{k_\perp}{k_0}\right)^{2/3} \left(\frac{\overline{\omega}_r}{\overline{\omega}_{r,0}}\right)^{-1/3}. \tag{4.23}$$

With (4.23), the energy distribution in the kinetic regime can be written as

$$E_{\mathrm{KAW,D}}(k_\perp) = \frac{B_0^2}{L^{1/3}\rho_i^{1/3}} k_\perp^{-11/3} \exp\left(-\frac{1}{2}C_K^{3/2} \int_{k_0}^{k_\perp} \mathrm{d}k'_\perp \frac{\overline{\gamma}(k'_\perp)}{\overline{\omega}_r(k'_\perp)} k'^{-1}_\perp\right). \tag{4.24}$$

The dependence of the energy distribution in both the MHD and the kinetic regime on $k_\perp$, B_0, L, and ρ_i is equal to the dependences obtained in von Papen & Saur (2015) in (4.2)-(4.3). Therefore, it is possible to combine our dissipation model, which assumes a constant energy distribution along $k_\parallel$, with the exponential energy distribution along $k_\parallel$ suggested by Cho et al. (2002) and applied in von Papen & Saur (2015). This combination leads to the final equations for the energy distribution in the MHD, the KAW, and the electron dissipation regime,

$$E_{\mathrm{MHD,D}}(\mathbf{k}) = \left(\frac{B_0^2}{L^{1/3}}\right) k_\perp^{-10/3} \exp\left(-L^{1/3}\frac{|k_\parallel|}{k_\perp^{2/3}}\right)$$

$$\times \exp\left(-\frac{1}{2}C_K^{3/2}\int_{k_0}^{k_\perp} \mathrm{d}k'_\perp \frac{\overline{\gamma}(k'_\perp)}{\overline{\omega}_r(k'_\perp)}k'^{-1}_\perp\right), \tag{4.25}$$

$$E_{\mathrm{KAW,D}}(\mathbf{k}) = \left(\frac{B_0^2}{L^{1/3}\rho_i^{1/3}}\right) k_\perp^{-11/3} \exp\left(-L^{1/3}\rho_i^{1/3}\frac{|k_\parallel|}{k_\perp^{1/3}}\right)$$

$$\times \exp\left(-\frac{1}{2}C_K^{3/2}\int_{k_0}^{k_\perp} \mathrm{d}k'_\perp \frac{\overline{\gamma}(k'_\perp)}{\overline{\omega}_r(k'_\perp)}k'^{-1}_\perp\right), \tag{4.26}$$

$$E_{\mathrm{ED,D}}(\mathbf{k}) = \left(\frac{B_0^2}{L^{1/3}\rho_i^{1/3}}\right) k_\perp^{-11/3} \exp\left(-L^{1/3}\rho_i^{1/3}\rho_e^{1/3}|k_\parallel|\right)$$

$$\times \exp\left(-\frac{1}{2}C_K^{3/2}\int_{k_0}^{k_\perp} \mathrm{d}k'_\perp \frac{\overline{\gamma}(k'_\perp)}{\overline{\omega}_r(k'_\perp)}k'^{-1}_\perp\right). \tag{4.27}$$

A contour plot of the energy distribution with damping according to (4.25)-(4.27) is

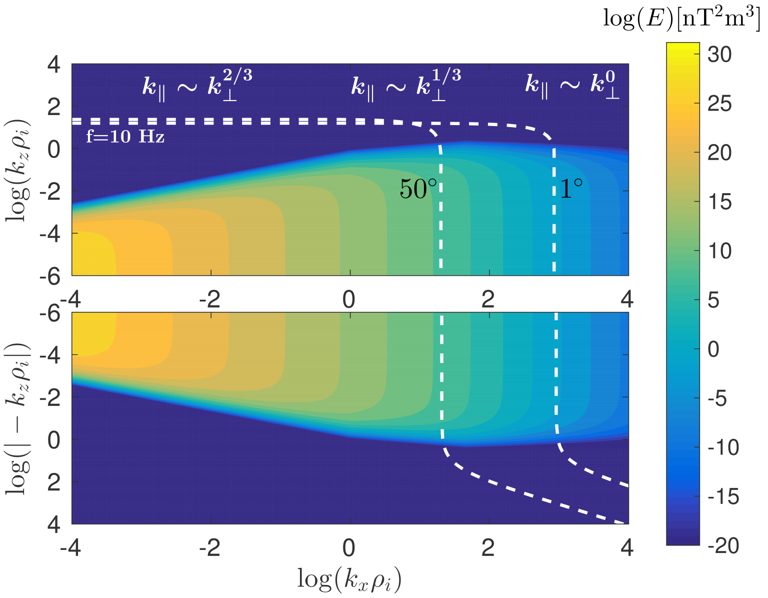

Figure 4.4: Double logarithmic plot of the energy density with damping as logarithmically equidistant iso-contours calculated with Equations (4.25)-(4.27) with the same parameters as in Figure 4.1 and with a Kolmogorov constant of $C_K = 3.1$ (The different value of C_K compared to the one-dimensional model will be discussed in Section 4.4). Integration planes according to (4.1) are shown as white dashed lines for field-to-flow angles of 1° and 50° for a frequency of 10 Hz.

shown in Figure 4.4 with the same plasma parameters as in Figure 4.1. Compared to

Figure 4.1, the energy decreases more rapidly in the perpendicular direction ($k_x\rho_i$) due to damping. A comparison of the integration planes for 1° and 50° for f= 10 Hz demonstrates that these integration planes are assigned to higher perpendicular wavenumbers for smaller field-to-flow angles. These higher perpendicular wavenumbers are more strongly affected by damping compared to smaller perpendicular wavenumbers. Hence, power spectral densities for smaller field-to-flow angles are more strongly influenced by KAW damping. The resultant power spectra for different field-to-flow angles are displayed in Figure 4.4. Black dashed lines show for comparison associated power spectral densities without damping. The spectral index in the sub-ion range for 90° (red), 50° (blue), and 20° (green) is shown on the right. The spectral index is fitted in the range between the Doppler-shifted ion gyroradius for $\theta_{\mathbf{vB}}$= 90° and 0.3 times the Doppler shifted electron gyroradius f_{ρ_e} for associated field-to-flow angles, where the spectrum can still be approximated by a power-law. The spectra for smaller field-to-flow angles are more and more affected by damping due to the sampling effect. For all field-to-flow angles, the spectral slope in the sub-ion range is steeper than the theoretically predicted spectral index

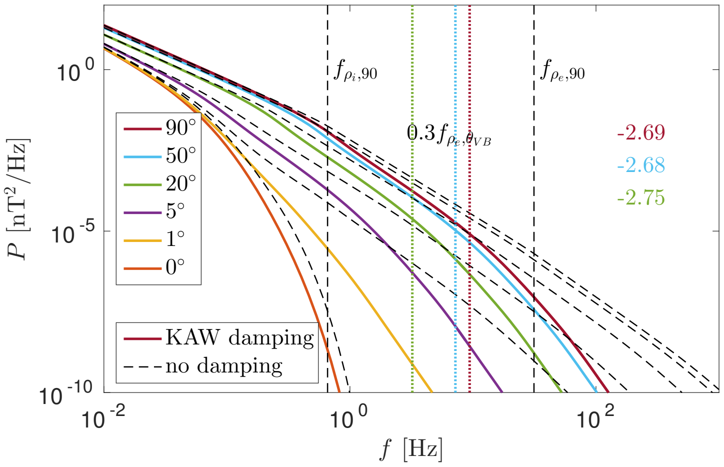

Figure 4.5: Power spectral densities for different field-to-flow angles in the MHD, KAW, and electron dissipation regime with KAW damping. Black dashed lines show power spectra without damping. The Doppler-shifted ion gyroradius and electron gyroradius for a field-to-flow angle of 90° are shown in the black dashed vertical lines. The colored dotted vertical lines show Doppler-shifted $0.3f_{\rho_e}$ for field-to-flow angles of 90° (red), 50° (blue), 20° (green). The numbers on the right give the spectral index fitted between $f_{\rho_i,90}$ and $0.3f_{\rho_e,\theta_{\mathbf{vB}}}$.

of 7/3 for a KAW driven turbulence. The spectral index varies from 2.7 for 90° to 2.75 for 20° in agreement with the observed range of spectral indices between 2.3 and 2.9, which are observed usually for large field-to-flow angles. The chosen parameters for the calculation of the energy distribution lead to relatively strong damping; for weaker damping, the steepening in the sub-ion range is not as strong. At electron scales, here marked by $f_{\rho_e,90}$, the spectrum can be described by an exponential or 'quasi'- exponential function, which is in agreement with the observations by Alexandrova et al. (2009, 2012). The analysis in this section shows, that damping of KAWs leads in general to a steepening of the spectral slope in the sub-ion range, which agrees with recent observations of magnetic spectral densities in this range. In the next section, we compare our model with a set of solar wind observations to analyze whether this steepening is in agreement with measurements for varying solar wind conditions.

4.3 Comparison with Solar Wind Observations

In this section, we first present the data set of Cluster observations and how it was obtained and analyzed. In the next part, we show how the reduced power spectra are calculated and how we compare them with each observed solar wind interval. The main part of this chapter presents the results of the comparison.

4.3.1 Data Set

We use a data set of solar wind data measured by the Cluster spacecraft in the free solar wind. Cluster is a constellation of four NASA/ESA spacecraft, which is in orbit around the Earth since 2000 to investigate the Earth's magnetic environment and its interaction with the solar wind in three dimensions. Owing to the high time resolution and the high accuracy of magnetic field measurements, Cluster data are well suitable to investigate kinetic scale turbulence. The data set was analyzed by Olga Alexandrova and Catherine Lacombe from the 'Observatoire de Paris' in France. Results of the analysis of this data set are published in Alexandrova et al. (2012). The authors selected 93 intervals of magnetic field data of 10 minutes, which were not connected magnetically to the Earth's bow shock and which were not contaminated by the presence of quasi-parallel propagating whistler waves, so that Taylor's hypothesis is applicable. The data were measured with the Cluster-1/STAFF Search Coil sensor (SC) for frequencies $f = [0.5,\ 9]\,\mathrm{Hz}$, and with the STAFF Spectrum Analyser (SA) for frequencies $f \geq 8\,\mathrm{Hz}$. The spectra are normal mode spectra averaged over 10 minutes calculated by a Morlet wavelet transform of the STAFF-SC data and by averages of the STAFF-SA spectra, which are recorded every 4 seconds. The spectra are analyzed for frequencies where the signal-to-noise ratio is larger than 3. The variations of the solar wind plasma parameters are in the following ranges: $v_{SW}\,[\mathrm{km/s}] \in [300,\ 700]$, $B\,[\mathrm{nT}] \in [2,\ 20]$, $T_i/T_e \in [0.5,\ 5]$, $\beta_i \in [0.1,\ 10]$, $\beta_e \in [0.1,\ 20]$. As the STAFF-SA spectra are not well calibrated at 8.8 Hz, 11 Hz, and 14 Hz, the spectra between 8.5 Hz and 17.5 Hz are linearly interpolated, which is a good approximation as far as the spectra follow a power-law at these frequencies. Figure 2.9 shows power spectral densities without correction at the mentioned frequencies. It can be clearly seen that a linear interpolation is suitable in this frequency range. For all intervals, the instrument background noise, which is obtained by measurements of the magnetic field in the magnetospheric lobes, is

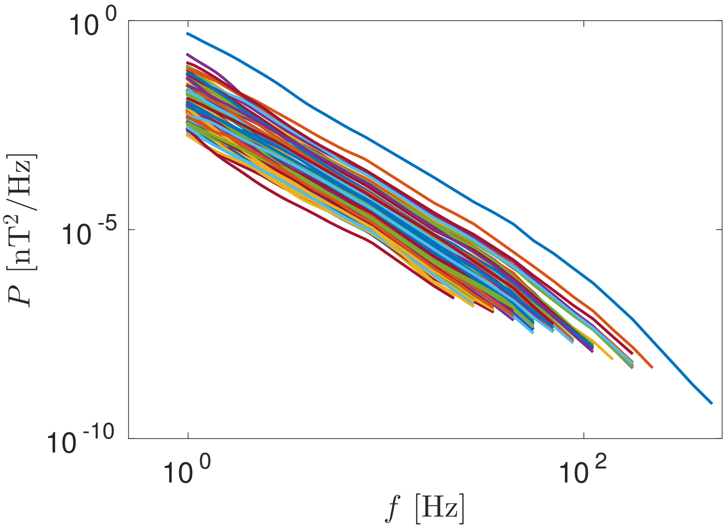

Figure 4.6: Magnetic power spectral densities of 93 intervals in the free solar wind measured with the Cluster-1/STAFF-SC sensor for $f = [0.5,\ 9]\,\mathrm{Hz}$ and the STAFF-SA instrument for $f \geq 8\,\mathrm{Hz}$ analyzed by Alexandrova et al. (2012). The spectra are analyzed for frequencies where the signal-to-noise ratio is larger than 3.

subtracted. The total magnetic spectrum, as shown in Figure 4.6, is calculated by the sum of the diagonal elements of the spectral tensor. In case of spectral densities measured with the STAFF-SA, 150 consecutive 4 s-average spectra are measured in each of the 10 minutes intervals. We estimate the error by calculating the standard deviation of the $\log_{10}$ value of the 150 spectra at every frequency. In the following, we do not take into account the errors at the first three frequencies of the STAFF-SA spectrum (8.8 Hz, 11 Hz, and 14 Hz) due to the poor calibration at these frequencies. We calculate the error for the spectrum with the highest intensity, i.e., the blue line with the highest intensity in Figure 4.6, and apply the estimated error to all remaining spectra because the instrument noise should be similar for all measurements. The estimated errors are shown in Figure 2.9 and are indicated in the following figures by error bars.

4.3.2 Calculation of Reduced Power Spectra

We calculate the reduced power spectra as shown in Section 4.2 with damping rates of KAWs, where we use the measured plasma parameters in each interval to obtain the damping rate $\overline{\gamma}(k_\perp)/\overline{\omega}_r$ and to calculate the parameters that are needed to obtain the three-dimensional energy distribution. Figure 4.7 displays the magnetic spectrum with the highest intensity, which is also presented in Alexandrova et al. (2012). The modeled spectrum without damping is shown in the blue dashed line, the modeled spectrum with damping is shown in the black line, and the observed spectrum with correction at the first three frequencies of the STAFF-SA instrument and without background noise is shown in the red dashed line with error bars. The vertical dashed lines mark the Doppler-shifted ion and electron gyroradius and inertial length. The model is shifted vertically so that the model is in agreement with the observed spectrum at $f = 3.5$ Hz. At frequencies larger than 3.5 Hz, no ion scale effects, such as damping or coherent structures, which are not taken into account in our model, influence the spectra in all intervals. Besides the intensity, the only other free parameter of our model is the Kolmogorov constant C_K, which

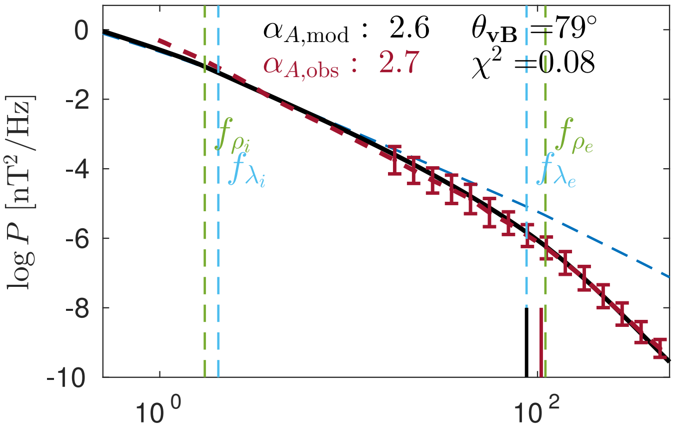

Figure 4.7: Most intense spectrum of the 93 observed intervals. The model without damping is shown in the blue dashed line, the model with damping in the black line, and the observations with error bars in the red dashed line. The vertical dashed lines mark the Doppler-shifted electron and ion gyroradius and inertial length. The measured plasma parameters are B=5.7 Hz, T_i = 72 eV, T_e= 33 eV, n_i =20 cm^{-3}, and v_{SW}=650 km/s. $\alpha_{A,\mathrm{mod}}$ and $\alpha_{A,\mathrm{obs}}$ give the spectral index in the sub-ion range of the model and the observations, respectively, obtained by fitting $P_A(k_\perp) = Ak_\perp^{-\alpha_A}\exp(-k_\perp l_d)$ to the spectra. The black and red vertical lines give the frequency of the dissipation length $f_d = v_{SW}/2\pi l_d$ for the model and the observation, respectively.

we determine by minimization of the χ^2 error

$$\chi^2 = 1/N\sum_{i=1}^{N}\left[\log_{10}(d(i)) - \log_{10}(m(i))\right]^2 / \log_{10}(\sigma(i))^2, \tag{4.28}$$

for data points with error bars, $d(i)$. $m(i)$ are the modeled power spectral densities and $\sigma(i)$ the errors at every data point. For a Kolmogorov constant of C_K=3.1, $\chi^2 < 1$ in all intervals and the mean value of χ^2 is 0.15. The different value of C_K compared to the value of C_K in the one-dimensional model is discussed in Section 4.4.

In Section 4.2, we obtain the spectral index in the sub-ion range by fitting a power-law between 3.5 Hz and $0.3 f_{\rho_e}$ to avoid any influence of the exponentially shaped dissipation range. In some of the intervals, which we analyze in this section, the exponentially shaped dissipation range sets in at scales larger than $0.3 f_{\rho_e}$. Additionally, the range between 3.5 Hz and $0.3 f_{\rho_e}$ is often relatively small, therefore, a power-law fit in this regime is not suitable to obtain the spectral index. For this reason, we obtain the spectral index α_A and the dissipation length l_d in the sub-ion range by fitting $P_A(k_\perp) = Ak_\perp^{-\alpha_A} \exp(-k_\perp l_d)$ to the spectra as was suggested by Alexandrova et al. (2012) and as was applied in Chapter 3. Note that the spectral index obtained by this method is not as steep as the spectral index obtained by the power-law fit. Further, note that we can not draw conclusions regarding the fitting parameter A, which describes the intensity of the power spectral density, because we shift the model in the vertical direction to be in agreement with the observed spectrum. Unfortunately, we have no information concerning the errors of the power spectral densities for the STAFF-SC instrument but only for the STAFF-SA instrument. Therefore, we do not consider the errors when fitting $P_A(k_\perp) = Ak_\perp^{-\alpha_A} \exp(-k_\perp l_d)$ to the observed spectra. Hence, no error estimations for the fitting parameters l_d and α_A can be given. In the next section, we show exemplary data comparisons and analyze the spectral index in the sub-ion range.

4.3.3 Comparison with Exemplary Data Intervals and Analysis of the Spectral Index

We present exemplary intervals for which we compare modeled power spectral densities with observed ones. For the sake of completeness, all intervals are shown in appendix A.1. The here presented examples are divided into four groups with four exemplary intervals each: Group 1 includes intervals, where model and observation have different spectral indices and do not agree well; group 2 contains intervals, where the spectral slope of the observations is shallower than in the model; in group 3, model and observation are in general agreement but the spectral slope of the observations is steeper than in the model; and in group 4, model and observation are in good agreement including matching spectral indices. The labeling in the following figures, (Figure 4.8, Figure 4.10, Figure 4.11, and Figure 4.13) is the same as in Figure 4.7.

Figure 4.8 displays exemplary intervals of group 1, i.e., the spectral index of the observed power spectral densities is steeper than the modeled one, and the intensity in the sub-ion and electron dissipation regime of the observation is lower than

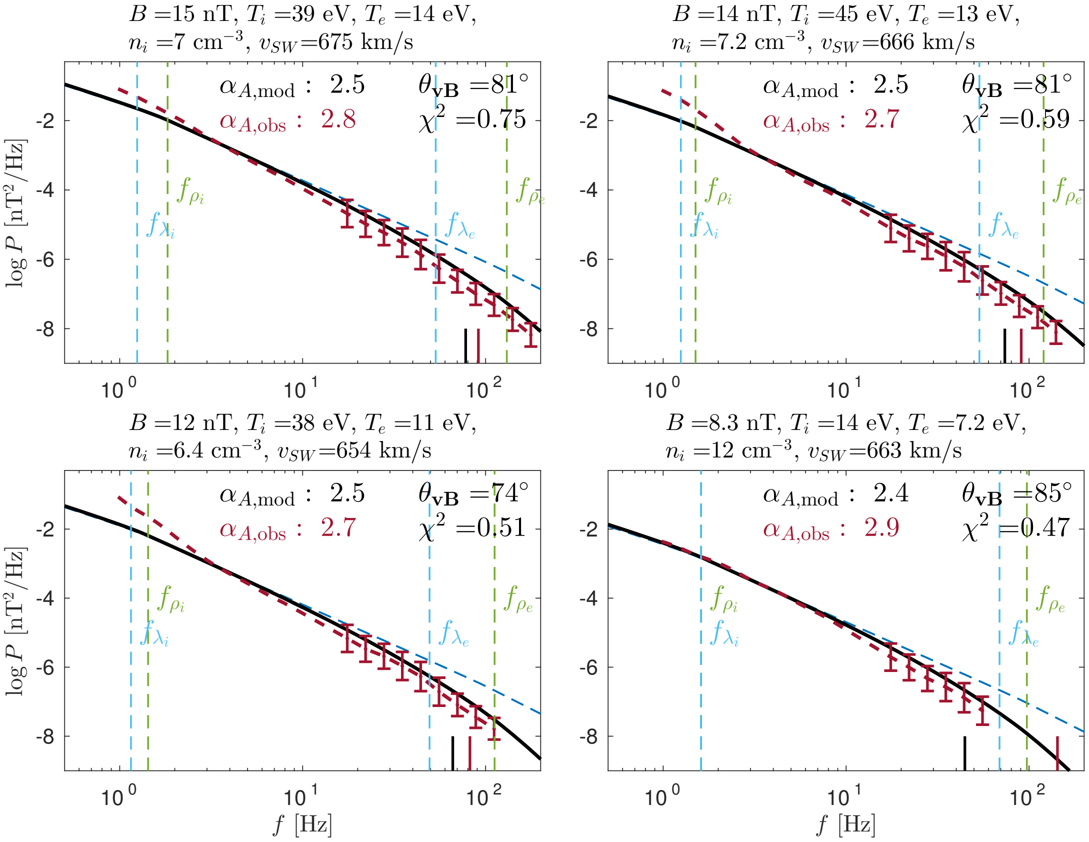

Figure 4.8: Exemplary intervals of group 1: Model and observation have different spectral indices and do not agree well. The labeling is the same as in Figure 4.7. Solar wind plasma parameters are given at the top of each panel. 8.6% of 93 intervals belong to this group.

in the model. This discrepancy can possibly be explained by intermittent events due to coherent structures, which lead to a steepening of the spectral slope in the sub-ion range (Boldyrev & Perez, 2012). Intermittent events in form of spatially localized coherent structures, specifically current sheets, emerge due to the nonlinear dynamics of the background flow (Salem et al., 2009). Numerical simulations of turbulent plasma flows indicate that dissipation is primary concentrated in these current sheets (Wan et al., 2012; Karimabadi et al., 2013; TenBarge & Howes, 2013; Wu et al., 2013; Zhdankin et al., 2013). This concept of dissipation appearing mainly in current sheets is not contradictory to a KAW driven turbulent cascade with damping by wave-particle interactions. We conclude that the KAW driven background turbu-

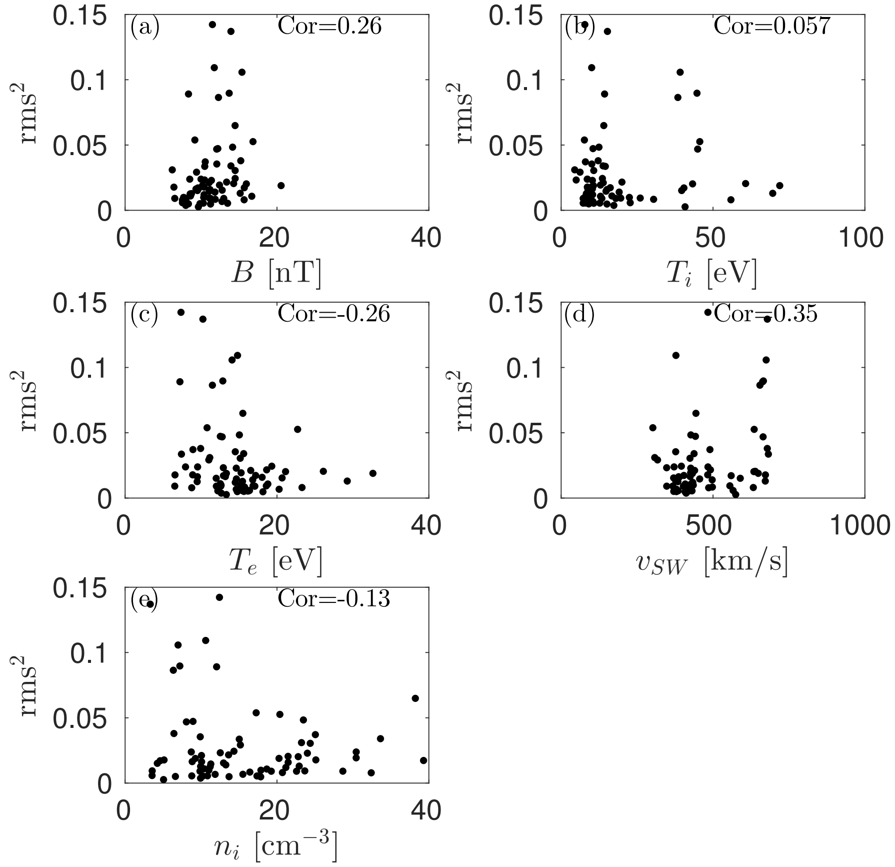

Figure 4.9: $\mathrm{rms}^2 = 1/N \sum_{i=1}^{N} [\log_{10}(d(i)) - \log_{10}(m(i))]^2$ for all observed power spectral densities $d(i)$ and associated modeled power spectral densities $m(i)$ as a function of the magnetic field (a), the ion temperature (b), the electron temperature (c), the solar wind velocity (d), and the plasma density (e) for intervals with $\alpha_{A,\mathrm{obs}} > \alpha_{A,\mathrm{mod}}$.

lent cascade might be overlayed by additional intermittency effects, which result in a steeper spectral slope in the observations. In order to investigate the occurrence of these intermittent events, we analyze the dependence of the rms^2 error on the plasma parameters B, T_i, T_e, n_i, and v_{SW} for intervals with $\alpha_{A,\mathrm{obs}} > \alpha_{A,\mathrm{mod}}$. Figure 4.9 shows that there is no clear correlation with any of the plasma parameters, which means that the intermittent events occur randomly or that the steeper spectral slope can not be explained by intermittency.

Figure 4.10 displays exemplary intervals of group 2, i.e., the spectral slope of the observed power spectral densities is shallower than the modeled spectral index. The

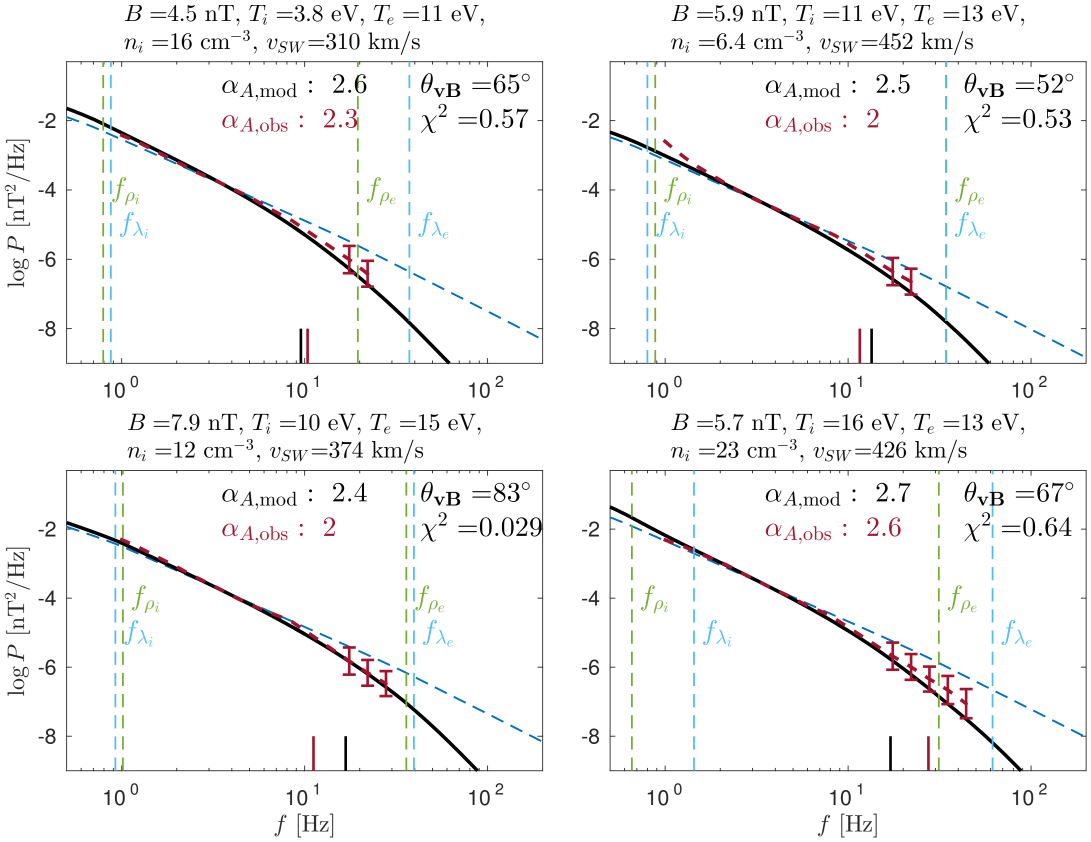
B =4.5 nT, T_i =3.8 eV, T_e =11 eV, n_i =16 cm^{-3}, v_{SW}=310 km/s

B =5.9 nT, T_i =11 eV, T_e =13 eV, n_i =6.4 cm^{-3}, v_{SW}=452 km/s

B =7.9 nT, T_i =10 eV, T_e =15 eV, n_i =12 cm^{-3}, v_{SW}=374 km/s

B =5.7 nT, T_i =16 eV, T_e =13 eV, n_i =23 cm^{-3}, v_{SW}=426 km/s

Figure 4.10: Exemplary intervals of group 2: The spectral slope in the observations is shallower than in the model. The labeling is the same as in Figure 4.7. Solar wind plasma parameters are given at the top of each panel. 11.8% of 93 intervals belong to this group.

intensity of the power spectral densities in this group are relatively low, and, therefore, the spectra reach the noise level for relatively low frequencies. Thus, no clear conclusion about the agreement of model and observations at electron scales can be drawn. Additionally, the relatively large dissipation scales (marked by the black and red vertical lines) in these intervals compared to the dissipation scales in Figures 4.8, 4.11, and 4.13 indicate that damping is relatively strong in these intervals, which results in a very short sub-ion range. Therefore, fitting a power-law with an exponential damping term might not be suitable for these intervals and the small spectral indices between 2 and 2.3 might not occur due to physical reasons. Especially in the bottom panels, the spectra seem to display a small bump at $\sim 10^1$ Hz.

Bumps have been observed at ion scales in Earth's magnetosheath and have been associated with Alfvén vortices. Similar effects might occur in the highly dynamic solar wind flow.

Most intervals are assigned to group 3, where model and observations are in general agreement with small values of χ^2 but the spectral slope of the observations is steeper than in the model. Exemplary intervals are shown in Figure 4.11. Similarly to the intervals in group 1, intermittent events could lead to a steeper spectral slope in the observations. In contrast to intervals in group 1, modeled power spectral densities in group 3 are in good agreement with the observed ones at electron scales with χ^2 values of less than 0.1. Because we do not take into account the errors of the

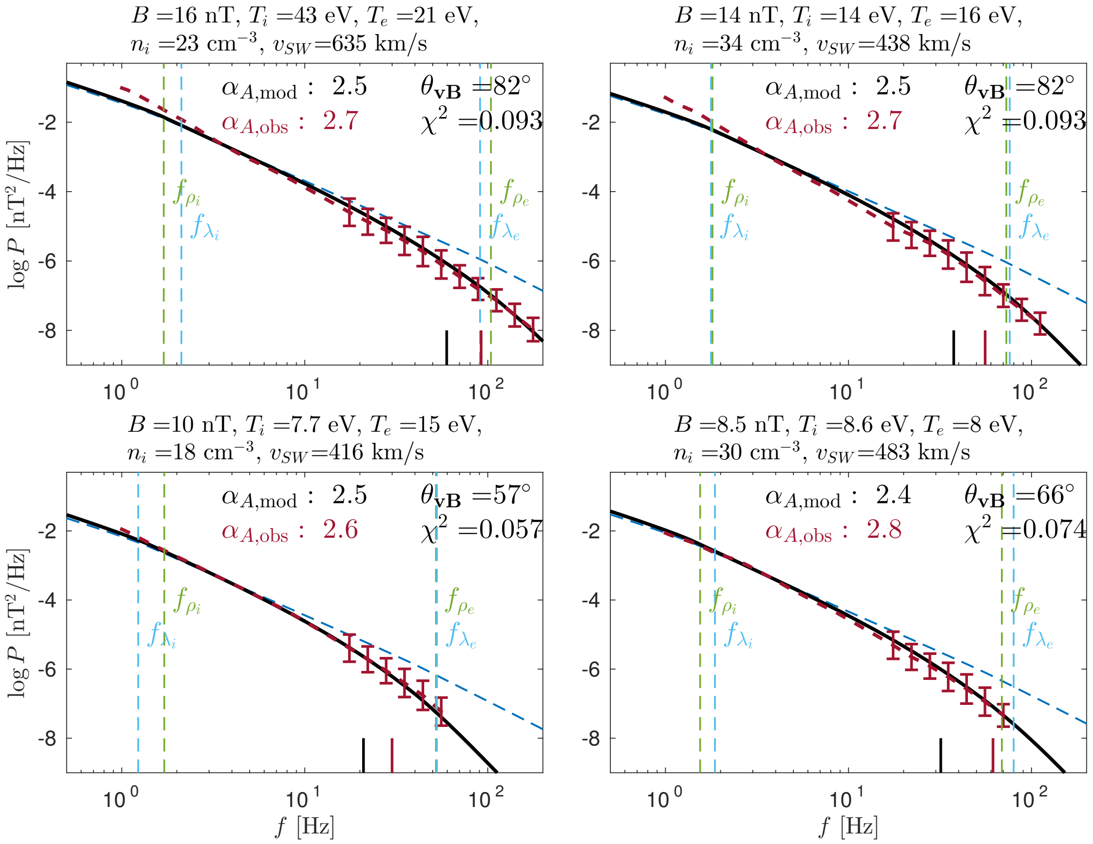

Figure 4.11: Exemplary intervals of group 3: Model and observations are in general agreement but the spectral slope of the observations is steeper than in the model. The labeling is the same as in Figure 4.7. Solar wind plasma parameters are given at the top of each panel. 54.8% of 93 intervals belong to this group.

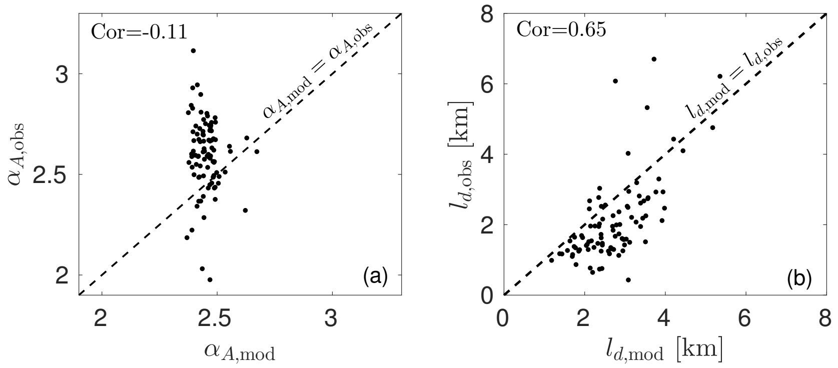

Figure 4.12: Spectral index in the sub-ion range of the observations $\alpha_{A,\mathrm{obs}}$ as a function of the spectral index of the model $\alpha_{A,\mathrm{mod}}$ (a), and observed dissipation length $l_{d,\mathrm{obs}}$ as a function of the modeled one $l_{d,\mathrm{mod}}$ (b).

observed power spectral densities when fitting the dissipation scale and the spectral index, we can not estimate errors of these fitting parameters. Due to fitting of α_A and l_d simultaneously, the obtained results are not unambiguous. Combinations of a smaller spectral index and a larger dissipation scale lead to similarly good fittings of the observations, which would be in better agreement with the spectral index and the dissipation scale of the model. Indeed, Figure 4.12 shows that the spectral index in the observations $\alpha_{A,\mathrm{obs}}$ with a mean value of 2.60 is in most intervals larger than the spectral index in the model $\alpha_{A,\mathrm{mod}}$ with a mean value of 2.45, whereas the dissipation length in the observations $l_{d,\mathrm{obs}}$ is in most intervals smaller than in the model $l_{d,\mathrm{mod}}$.

Figure 4.13 shows intervals of group 4, i.e., model and observations are in good agreement including matching spectral indices. Jointly, group 3 and group 4, i.e., intervals where the model is in agreement with the observations at electron scales, contain about 80% of the 93 intervals. Additionally, the value of χ^2 is less than one in all observed intervals. Thus, we conclude that a KAW driven turbulent background cascade is present in all observed intervals. However, additional effects, such as intermittency or coherent structures and wave modes, might influence the power spectral densities in the sub-ion range leading to a steeper spectral slope. As shown in Figure 4.9, it is not possible to identify solar wind parameter ranges, where these additional effects occur preferentially, which might indicate that these structures

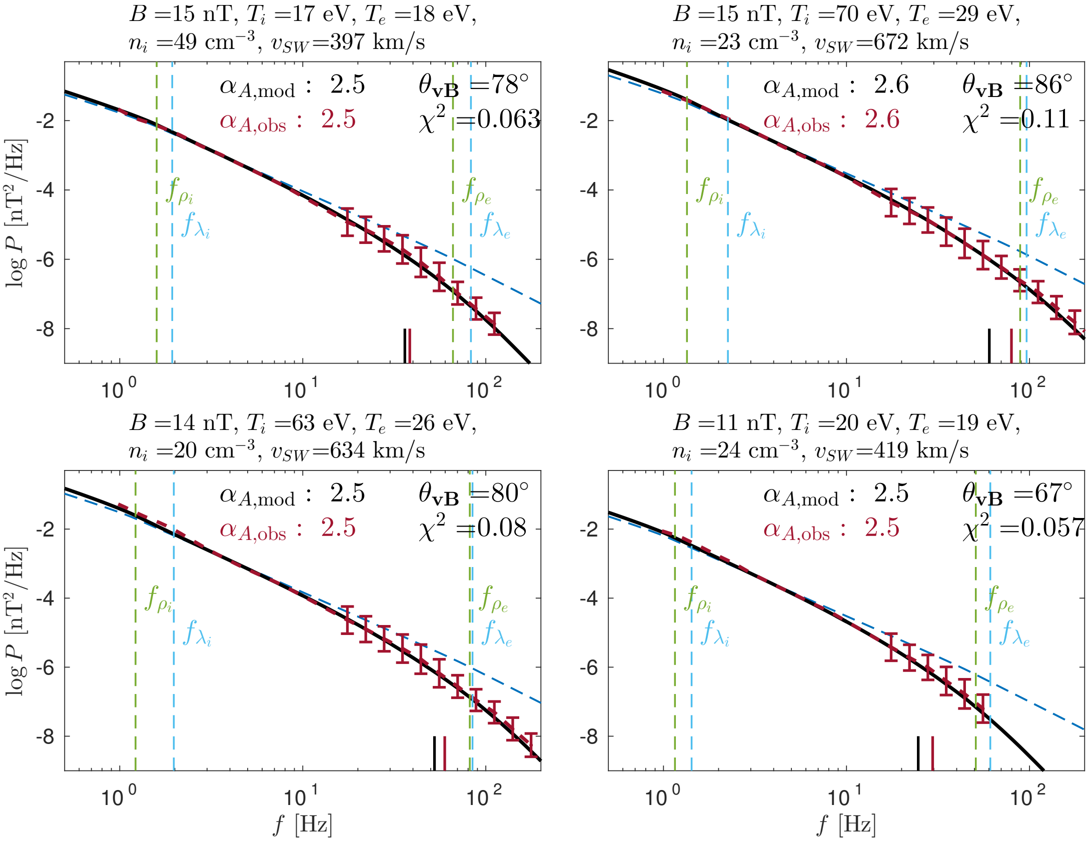

Figure 4.13: Exemplary intervals of group 4: Model and observation are in good agreement including matching spectral indices. The labeling is the same as in Figure 4.7. Solar wind plasma parameters are given at the top of each panel. 24.7% of 93 intervals belong to this group.

occur randomly. Analysis of the solar wind conditions of the intervals that where eliminated due to the presence of quasi-parallel propagating whistler waves might give a more detailed insight into this question. A steepening of the spectral index in the sub-ion range due to a variation of the field-to-flow angle as shown in Figure 4.5 would indicate that the combination of KAW turbulence and critical balance is suitable to describe solar wind turbulence. Unfortunately, the field-to-flow angles in our data set vary only between 50° and 90°, i.e., the influence of the damping on the spectral index is more important than the influence of the field-to-flow angle. Therefore, no clear conclusion about the steepening due to varying field-to-flow angles can be drawn.

The key results of the analysis in this chapter can be summarized as follows: In general, KAW damping in combination with the sampling effect, which arises when calculating the reduced power spectra, leads to a steeper spectral slope in the sub-ion range than the theoretically predicted slope of -7/3. KAW damping is therefore one possibility to explain the steep observed spectral index, which is not in agreement with -7/3. In more detail, this steepening gets even stronger for small field-to-flow angles, because in this case the integration planes of Equation (4.1) go to higher perpendicular wavenumbers, which are more strongly affected by damping. The steepening of the spectral slope due to damping has already been reported in von Papen & Saur (2015), but in contrast to our study, they use an empirical function to describe KAW damping and not physically motivated damping rates obtained from the hot dispersion relation. The comparison of the reduced power spectra with a set of solar wind observations shows that a critically balanced turbulent cascade with KAW damping is able to explain the observed power spectral densities with a value of χ^2 of less than one in all observed intervals. However, the spectral index in the sub-ion range of the observations is in most intervals steeper than the modeled one. Thus, we conclude that a KAW driven background turbulence is present in all observed intervals, but other effects, such as intermittent events or coherent structures, might influence the spectral slope as well. In the following section, we discuss the approximations and limitations of the presented approach.

4.4 Discussion

Owing to the analogy of the one-dimensional dissipation model and the three-dimensional one, the discussion part of the one-dimensional model concerning critical balance, the linearity of the model, influence of nonlocal effects, the Maxwellian distribution of electrons and ions, and the description of solar wind turbulence with the nonlinear interaction of linear wave modes applies also for the three-dimensional dissipation model and is not discussed here again.

To obtain the equation for the calculation of the reduced power spectra in (4.1), the assumptions of Taylor's hypothesis and statistical stationarity (which implies statistical homogeneity when Taylor's hypothesis is applicable) have to be made.

Since KAWs are low-frequency waves and the data set does not contain intervals with quasi-parallel propagating whistler waves, Taylor's hypothesis is valid for the observed intervals. For the application of this model to whistler wave turbulence, the validity of Taylor's hypothesis should be reconsidered. Time stationarity of the solar wind has been tested by Matthaeus & Goldstein (1982) who show that time series of the interplanetary magnetic field ranging from days to years satisfy the condition of stationarity in a weak sense, which means that the average properties of the time series are unchanged for any given time translation. More recently, Perri & Balogh (2010) analyze an extended set of solar wind observations in comparison to Matthaeus & Goldstein (1982) and conclude that weak stationarity is a good assumption in the fast solar wind flow, whereas for mixed streams this assumption should be treated with caution. However, they find that this non-stationarity of mixed flows is more important beyond 1 AU.

By applying the three-dimensional model to observations, we find that the Kolmogorov constant that fits best to the observations has a value of $C_{K,3} = 3.1$, which is close to the value of $C_K = 3.27 \pm 0.07$ found by three-dimensional numerical simulations of Alfvénic turbulence (Beresnyak, 2011). However, $C_{K,3}$ differs from the value of $C_{K,1} \approx [1.4, 1.8]$ of the one-dimensional model. This difference is a result of the different prefactors in the exponential damping term of $1/2$ in the three-dimensional model and $4/3$ in the one-dimensional model. When calculating the reduced one-dimensional k spectrum from the three-dimensional spectrum via

$$P(k_\perp) = \int_0^{2\pi} \int_{k_{z,0}}^{k_{z,max}} E(k_\perp, k_z) k_\perp \mathrm{d}\varphi \mathrm{d}k_z, \tag{4.29}$$

one sees that the exponential damping term in the one-dimensional and the three-dimensional model is the same. The only way to achieve this equality is to set $C_{K,3} = (8/3)^{2/3} C_{K,1} \approx 3.1$.

Following von Papen & Saur (2015), we assume an exponential energy distribution in the parallel direction, which was suggested by Cho et al. (2002), who analyzed simulation results of incompressible MHD turbulence. However, the exact energy distribution below and at the critical balance path $k_\parallel = k_\perp^{e,CB}$ is not known, and several other suggested realizations exist, e.g., a Heaviside function, i.e, the energy is at a constant value below the critical balance path and zero above, a Gaussian function, i.e., the energy follows a Gaussian distribution centered at the critical balance path, or the Dirac Delta function, which we use in the one-dimensional model, i.e., there is only energy along the critical balance path. All of these energy distributions result in similar power spectral densities (see Figure A.13 in appendix A.2), so that it is not possible to draw conclusions about the exact energy distribution in the parallel direction by analyzing observed reduced power spectral densities. In the following chapter, we summarize the results presented in Chapter 3 and Chapter 4 and discuss the limitations of our model.

5 Summary and Conclusions

The solar wind provides the largest laboratory to study turbulence in magnetized plasma due to an enormous number of space missions that take in situ measurements of the magnetic field, the electric field, and the plasma parameters. However, owing to the requirement for a kinetic description at sub-ion and electron scales, the interpretation of solar wind observations at these scales remains difficult, and a number of physical aspects of the dissipation process are still poorly understood. The studies in this thesis help to give an improved characterization of the kinetic cascade process and more detailed insight into the question how the turbulent energy is dissipated in the solar wind. In Chapter 3, we presented an one-dimensional 'quasi'-analytical dissipation model in wavenumber space to describe power spectral densities at kinetic scales. The model is a combination of the energy cascade from large to small scales and KAW damping, which removes energy from the magnetic fluctuations at small scales. KAW damping is quantified by the imaginary part of the wave frequency obtained from the general hot dispersion relation, which describes the properties of plasma waves. The analysis in this chapter reveals that the real part of the wave frequency does not exceed the ion gyrofrequency under the assumption of critical balance due to the influence of damping on the parallel wavenumber. Therefore, the turbulent cascade is driven by KAWs rather than whistler waves. Owing to this low-frequency nature of KAWs, the application of Taylor's hypothesis to solar wind observations is reasonable. We find that the surprising independence of the dissipation length from the injected energy flux is a result of the combination of an anisotropic energy transport and a damping rate that is proportional to the parallel wavenumber. The more energy is injected at large scales, the more effective the damping gets at small scales. We present the first comparison of a dissipation model with actual solar wind measurements, which confirms that a combination of a critically balanced energy cascade and KAW damping is able to explain observed power spectral densities. Analysis of the KAW damping rate shows that damping by KAW results in a 'quasi'-exponentially shaped dissipation range, which agrees with observations in Alexandrova et al. (2009, 2012). However, additional damping effects by other wave modes might explain the observed power-law dissipation range in Sahraoui et al. (2009, 2013). The results of a statistical study with varying solar wind conditions show a high correlation of the dissipation length and the electron gyroradius. Thus, we conclude that the electron gyroradius acts as a dissipation scale in a KAW driven turbulent cascade.

The relation of frequencies and wavenumbers as applied in the one-dimensional model is only valid for a field-to-flow angle of 90°. For smaller field-to-flow angles different wavevectors map to the power spectrum at a given frequency, which is called sampling effect (von Papen & Saur, 2015). In order to take into account this sampling effect, in Chapter 4, we extend the one-dimensional model to three dimensions, and use a forward modeling approach by von Papen & Saur (2015) to calculate reduced power spectra in frequency space, which can be compared directly with measurements. In agreement with the study by von Papen & Saur (2015), we find that the KAW damping in combination with the sampling effect results in a spectral slope in the sub-ion range that is steeper than -7/3, and that this steepening gets even stronger for small field-to-flow angles. In general, KAW damping is therefore a reasonable explanation for the observed spectral slope in the sub-ion range, which is steeper than the theoretically predicted value of -7/3. In contrast to the study by von Papen & Saur (2015), we present the first calculation of reduced power spectra with damping rates obtained from the hot dispersion relation. The comparison of the reduced power spectra with a set of solar wind Cluster observations confirms our findings in Chapter 3 that a combination of critical balance and KAW damping results in modeled power spectra that agree with the observations. In detail, in all 93 observed and analyzed intervals, the χ^2 error of modeled power spectral densities and observed ones is less than one. However, the observed spectral index in the sub-ion range is still steeper than the spectral index in the model in most of the intervals. Thus, we conclude that the KAW driven background turbulence is present in all observed intervals, but that intermittent events or other wave modes might influence the spectral slope additionally. Unfortunately, the occurrence of these additional effects can not be characterized in detail or associated with certain solar wind conditions.

Both, the one-dimensional and the three-dimensional model were derived to describe solar wind turbulence at kinetic scales. When applying the model to other scales or other space plasmas, the following assumptions have to be reconsidered. The dissipation model as presented in this thesis is not able to handle a change from strong to weak turbulence at small scales, where the damping reduces the amplitudes of the nonlinear interaction, so that weak turbulence should be applied. Also, the model does not account for the mutual feedback of the nonlinear cascade and the process transferring magnetic field energy to particle energy, which might become stronger at small scales. These assumptions limit the considered scales to electron scales. Physical processes that act on scales significantly smaller than electron scales can not be described with the model. The assumptions of local interactions, Maxwellian distributed electrons and ions, Taylor's hypothesis, and statistical stationarity need to be verified when going to smaller scales or when going to other space environments, such as planetary magnetospheres, which also exhibit turbulent features. Especially in the polar environment of the gas planets, the low densities and high magnetic fields, which lead to relativistic effects, need to be taken into account.

A Appendix

A.1 Comparison of Modeled Power Spectral Densities with All 93 Observed Solar Wind Spectra

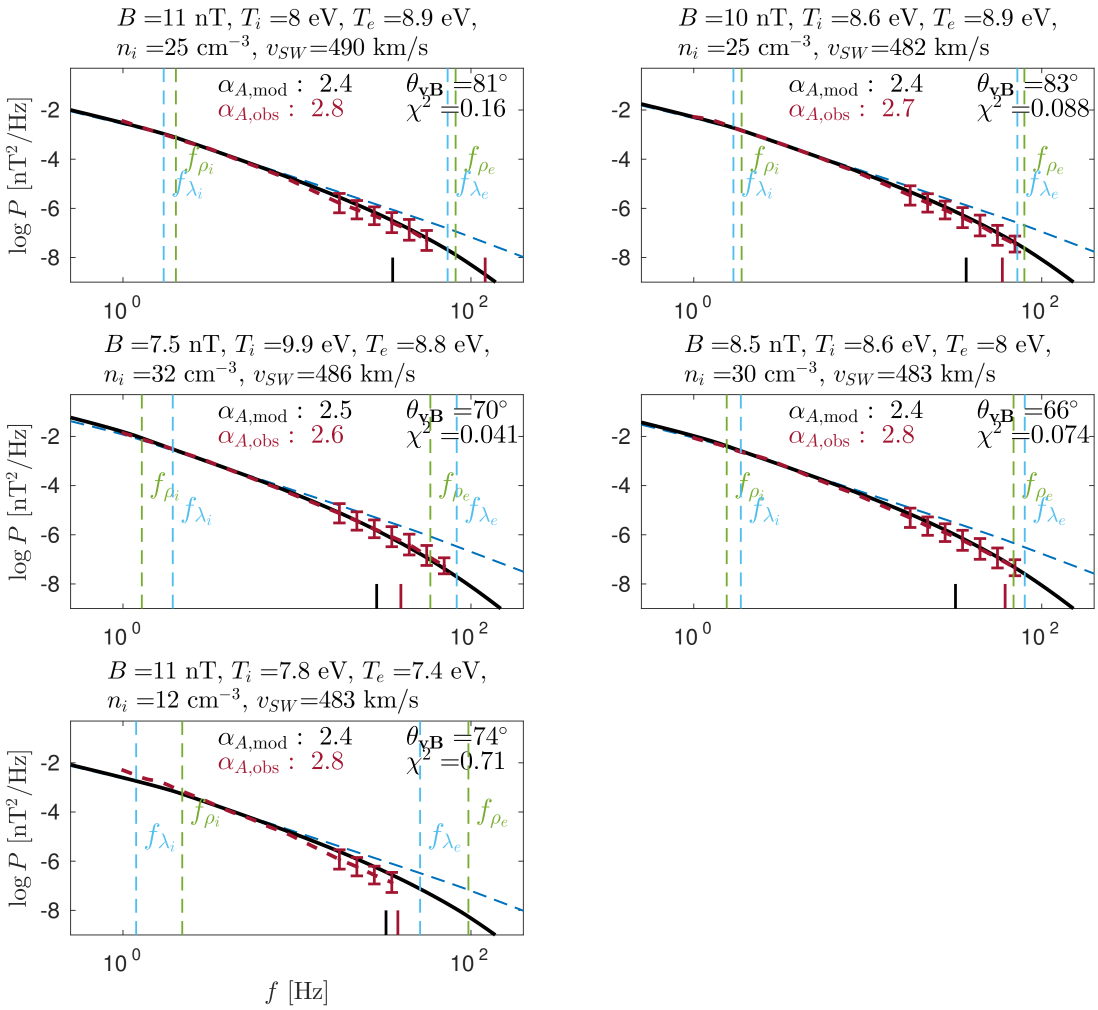

Figure A.1: Same labeling as Figure 4.8.

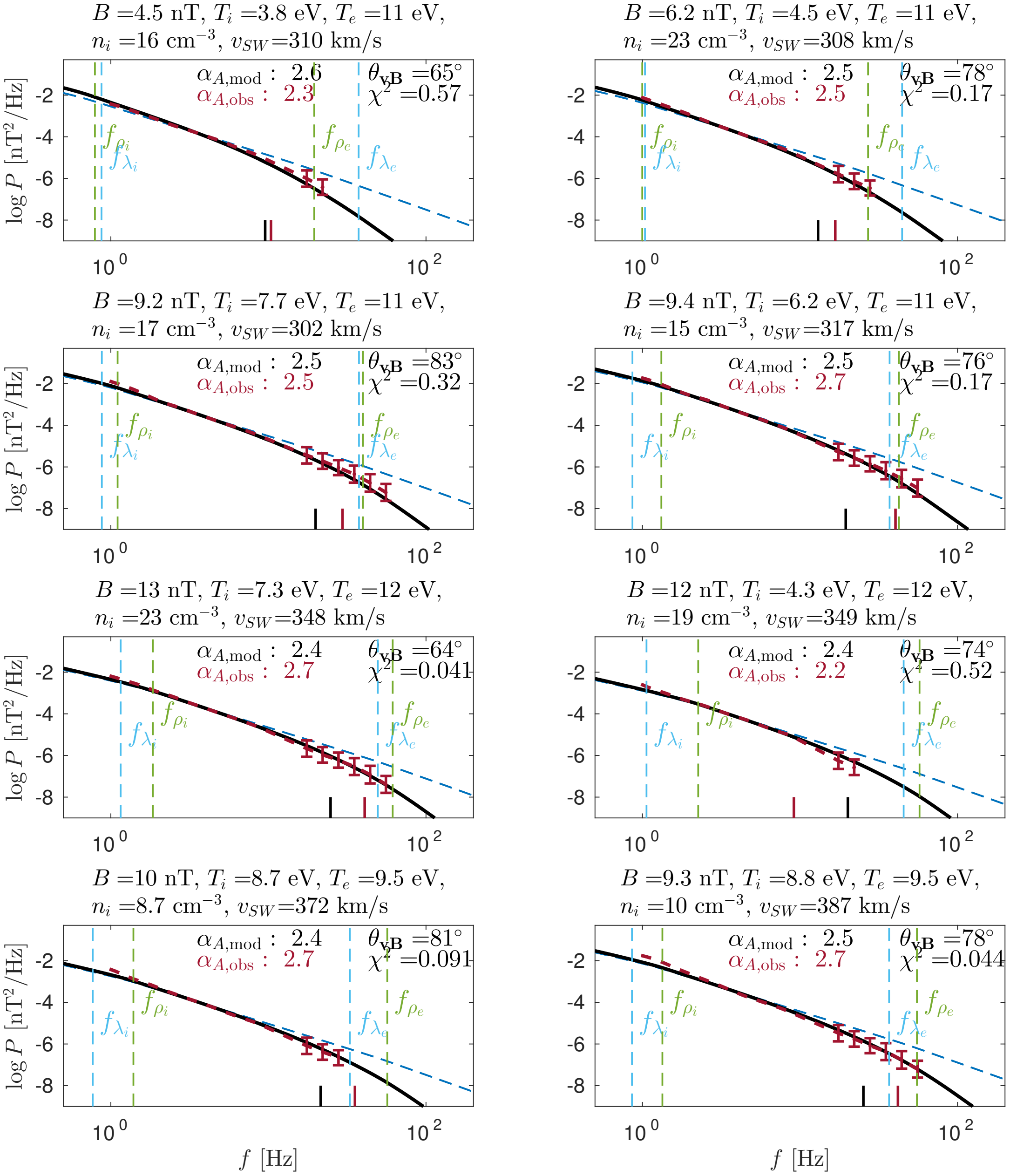

B =4.5 nT, T_i =3.8 eV, T_e =11 eV, n_i =16 cm^{-3}, v_{SW}=310 km/s

B =6.2 nT, T_i =4.5 eV, T_e =11 eV, n_i =23 cm^{-3}, v_{SW}=308 km/s

B =9.2 nT, T_i =7.7 eV, T_e =11 eV, n_i =17 cm^{-3}, v_{SW}=302 km/s

B =9.4 nT, T_i =6.2 eV, T_e =11 eV, n_i =15 cm^{-3}, v_{SW}=317 km/s

B =13 nT, T_i =7.3 eV, T_e =12 eV, n_i =23 cm^{-3}, v_{SW}=348 km/s

B =12 nT, T_i =4.3 eV, T_e =12 eV, n_i =19 cm^{-3}, v_{SW}=349 km/s

B =10 nT, T_i =8.7 eV, T_e =9.5 eV, n_i =8.7 cm^{-3}, v_{SW}=372 km/s

B =9.3 nT, T_i =8.8 eV, T_e =9.5 eV, n_i =10 cm^{-3}, v_{SW}=387 km/s

Figure A.2: Same labeling as Figure 4.8.

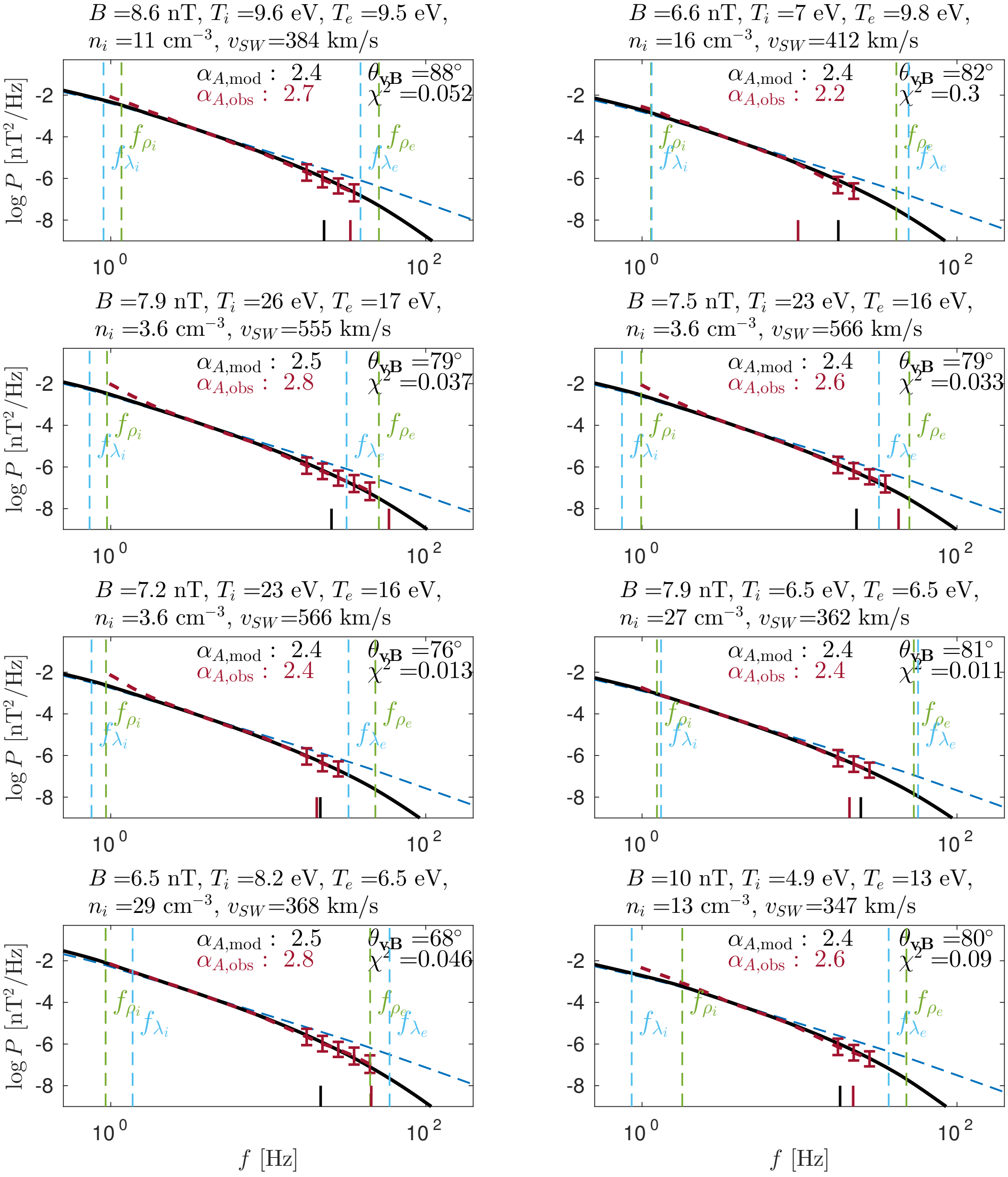

B =8.6 nT, T_i =9.6 eV, T_e =9.5 eV, n_i =11 cm^{-3}, v_{SW}=384 km/s

B =6.6 nT, T_i =7 eV, T_e =9.8 eV, n_i =16 cm^{-3}, v_{SW}=412 km/s

B =7.9 nT, T_i =26 eV, T_e =17 eV, n_i =3.6 cm^{-3}, v_{SW}=555 km/s

B =7.5 nT, T_i =23 eV, T_e =16 eV, n_i =3.6 cm^{-3}, v_{SW}=566 km/s

B =7.2 nT, T_i =23 eV, T_e =16 eV, n_i =3.6 cm^{-3}, v_{SW}=566 km/s

B =7.9 nT, T_i =6.5 eV, T_e =6.5 eV, n_i =27 cm^{-3}, v_{SW}=362 km/s

B =6.5 nT, T_i =8.2 eV, T_e =6.5 eV, n_i =29 cm^{-3}, v_{SW}=368 km/s

B =10 nT, T_i =4.9 eV, T_e =13 eV, n_i =13 cm^{-3}, v_{SW}=347 km/s

Figure A.3: Same labeling as Figure 4.8.

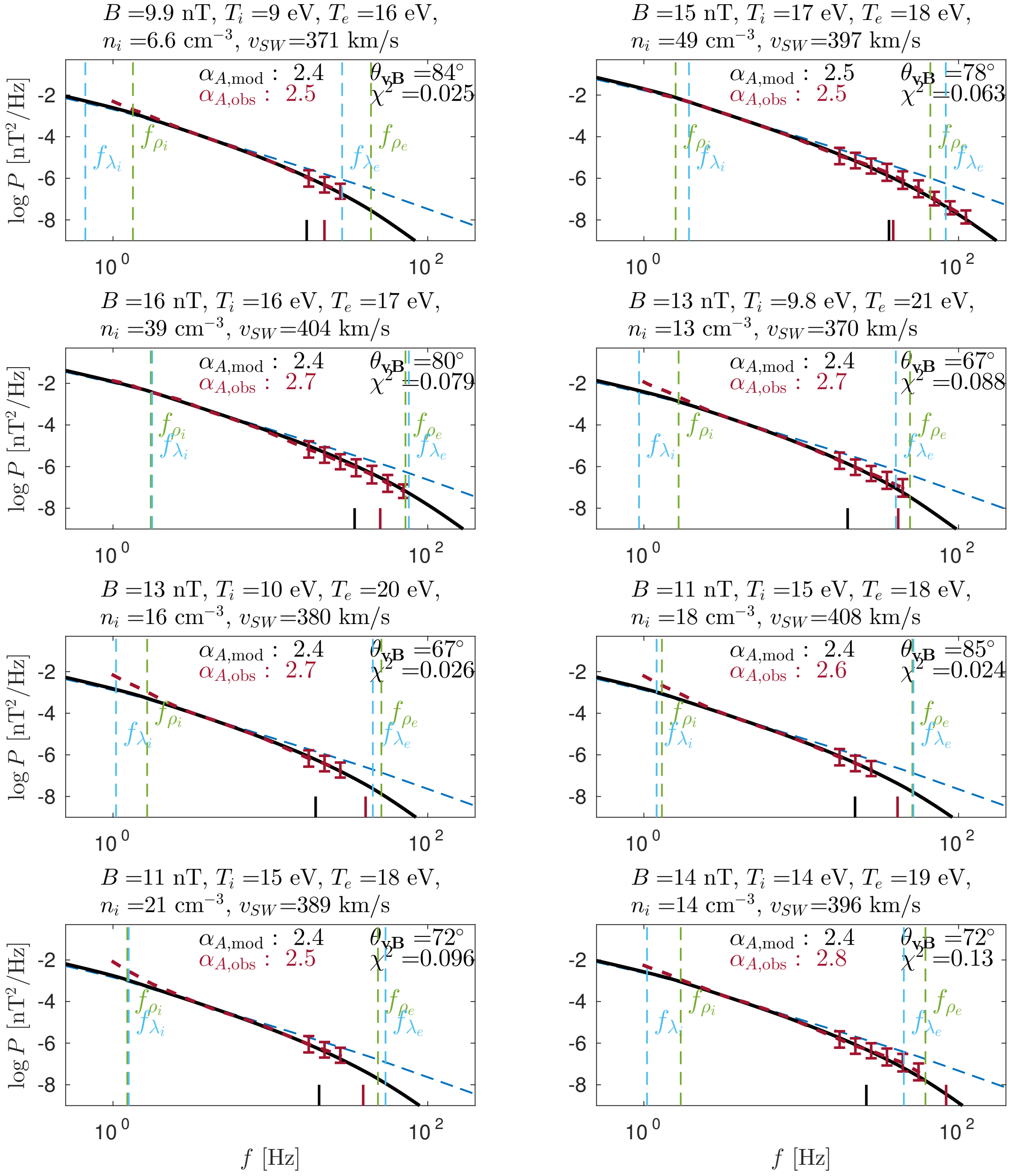

B =9.9 nT, T_i =9 eV, T_e =16 eV, n_i =6.6 cm^{-3}, v_{SW}=371 km/s

B =15 nT, T_i =17 eV, T_e =18 eV, n_i =49 cm^{-3}, v_{SW}=397 km/s

B =16 nT, T_i =16 eV, T_e =17 eV, n_i =39 cm^{-3}, v_{SW}=404 km/s

B =13 nT, T_i =9.8 eV, T_e =21 eV, n_i =13 cm^{-3}, v_{SW}=370 km/s

B =13 nT, T_i =10 eV, T_e =20 eV, n_i =16 cm^{-3}, v_{SW}=380 km/s

B =11 nT, T_i =15 eV, T_e =18 eV, n_i =18 cm^{-3}, v_{SW}=408 km/s

B =11 nT, T_i =15 eV, T_e =18 eV, n_i =21 cm^{-3}, v_{SW}=389 km/s

B =14 nT, T_i =14 eV, T_e =19 eV, n_i =14 cm^{-3}, v_{SW}=396 km/s

Figure A.4: Same labeling as Figure 4.8.

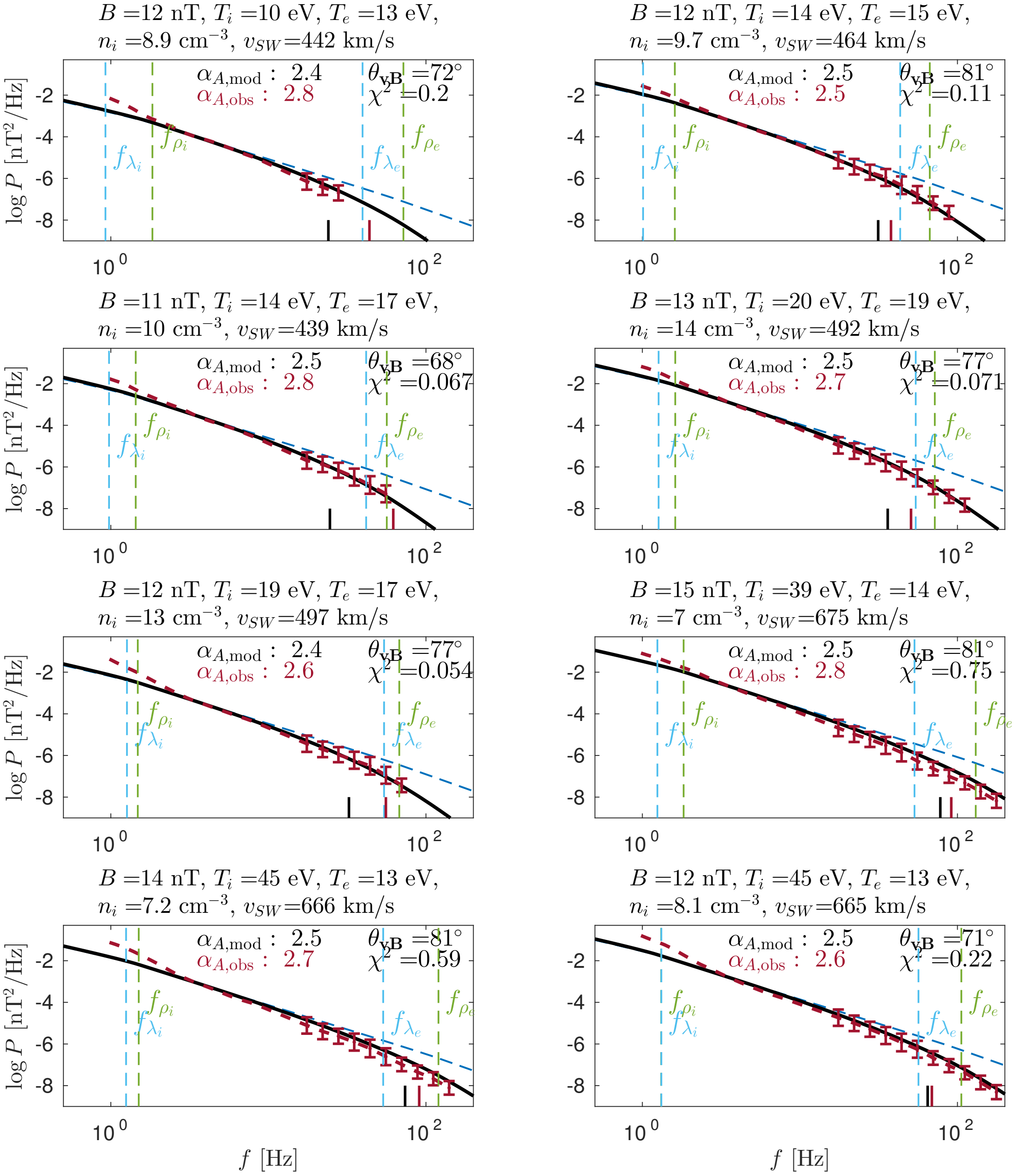

Figure A.5: Same labeling as Figure 4.8.

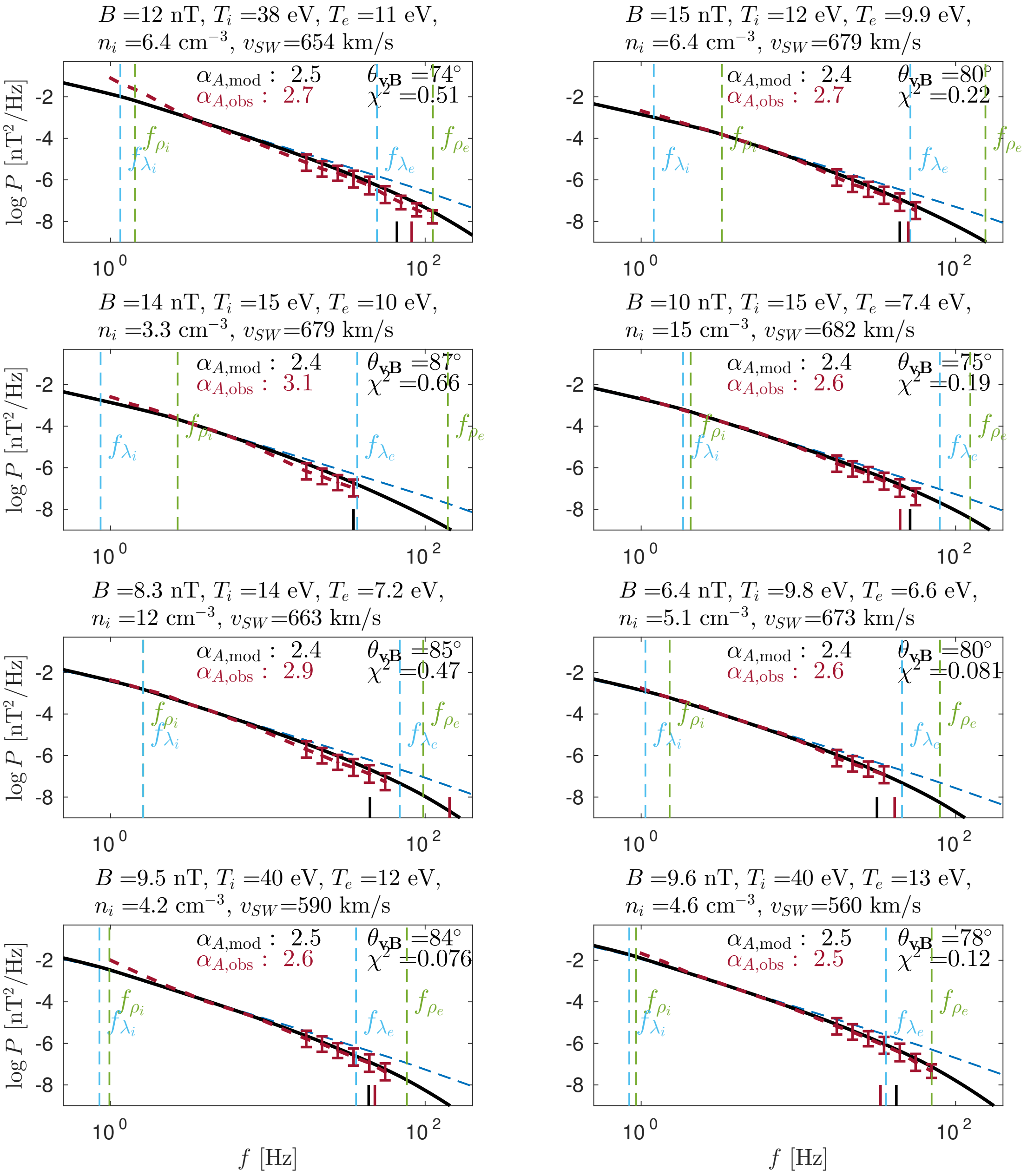
B =12 nT, T_i =38 eV, T_e =11 eV, n_i =6.4 cm^{-3}, v_{SW}=654 km/s

B =15 nT, T_i =12 eV, T_e =9.9 eV, n_i =6.4 cm^{-3}, v_{SW}=679 km/s

B =14 nT, T_i =15 eV, T_e =10 eV, n_i =3.3 cm^{-3}, v_{SW}=679 km/s

B =10 nT, T_i =15 eV, T_e =7.4 eV, n_i =15 cm^{-3}, v_{SW}=682 km/s

B =8.3 nT, T_i =14 eV, T_e =7.2 eV, n_i =12 cm^{-3}, v_{SW}=663 km/s

B =6.4 nT, T_i =9.8 eV, T_e =6.6 eV, n_i =5.1 cm^{-3}, v_{SW}=673 km/s

B =9.5 nT, T_i =40 eV, T_e =12 eV, n_i =4.2 cm^{-3}, v_{SW}=590 km/s

B =9.6 nT, T_i =40 eV, T_e =13 eV, n_i =4.6 cm^{-3}, v_{SW}=560 km/s

Figure A.6: Same labeling as Figure 4.8.

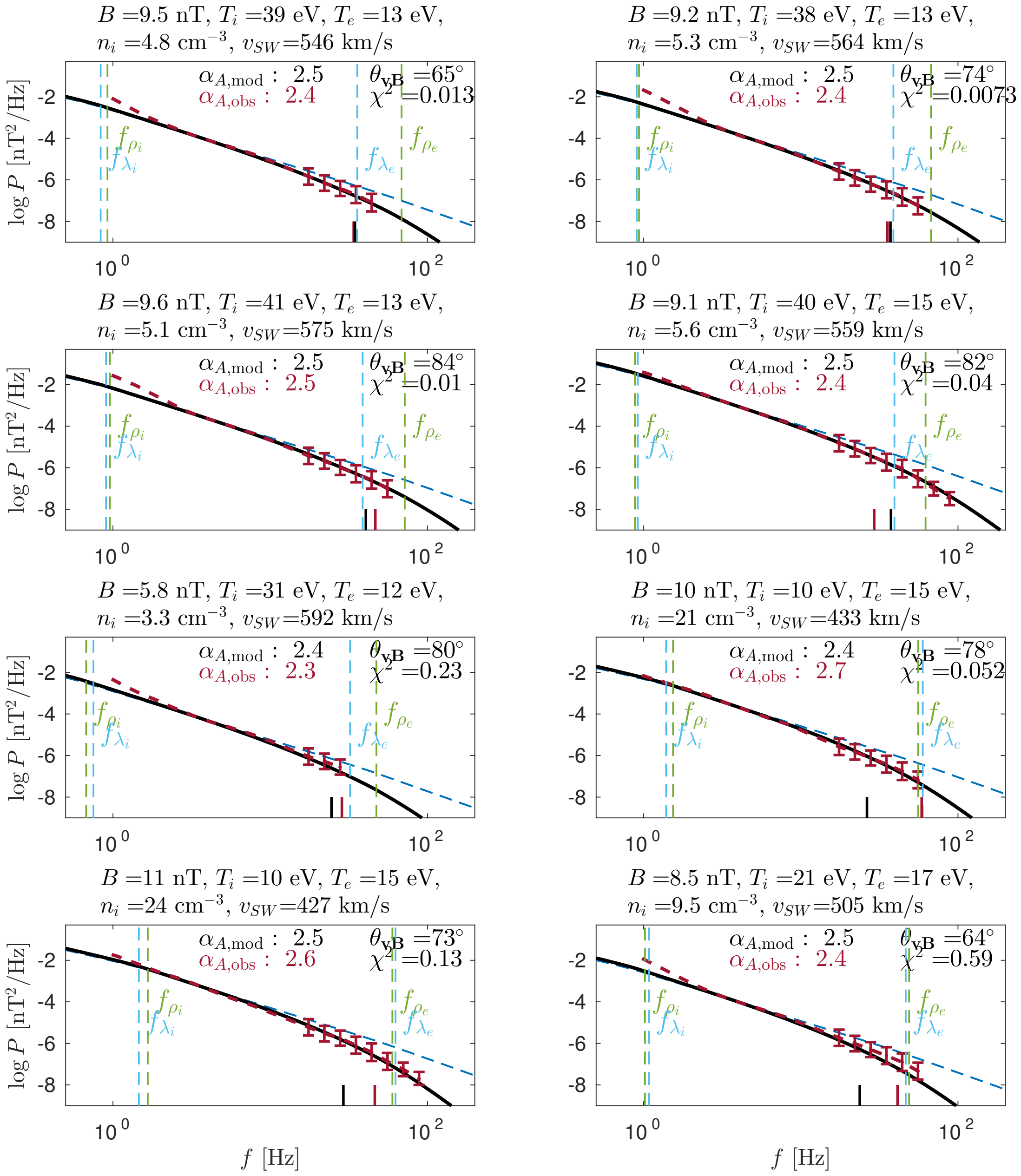

B =9.5 nT, T_i =39 eV, T_e =13 eV, n_i =4.8 cm^{-3}, v_{SW}=546 km/s

B =9.2 nT, T_i =38 eV, T_e =13 eV, n_i =5.3 cm^{-3}, v_{SW}=564 km/s

B =9.6 nT, T_i =41 eV, T_e =13 eV, n_i =5.1 cm^{-3}, v_{SW}=575 km/s

B =9.1 nT, T_i =40 eV, T_e =15 eV, n_i =5.6 cm^{-3}, v_{SW}=559 km/s

B =5.8 nT, T_i =31 eV, T_e =12 eV, n_i =3.3 cm^{-3}, v_{SW}=592 km/s

B =10 nT, T_i =10 eV, T_e =15 eV, n_i =21 cm^{-3}, v_{SW}=433 km/s

B =11 nT, T_i =10 eV, T_e =15 eV, n_i =24 cm^{-3}, v_{SW}=427 km/s

B =8.5 nT, T_i =21 eV, T_e =17 eV, n_i =9.5 cm^{-3}, v_{SW}=505 km/s

Figure A.7: Same labeling as Figure 4.8.

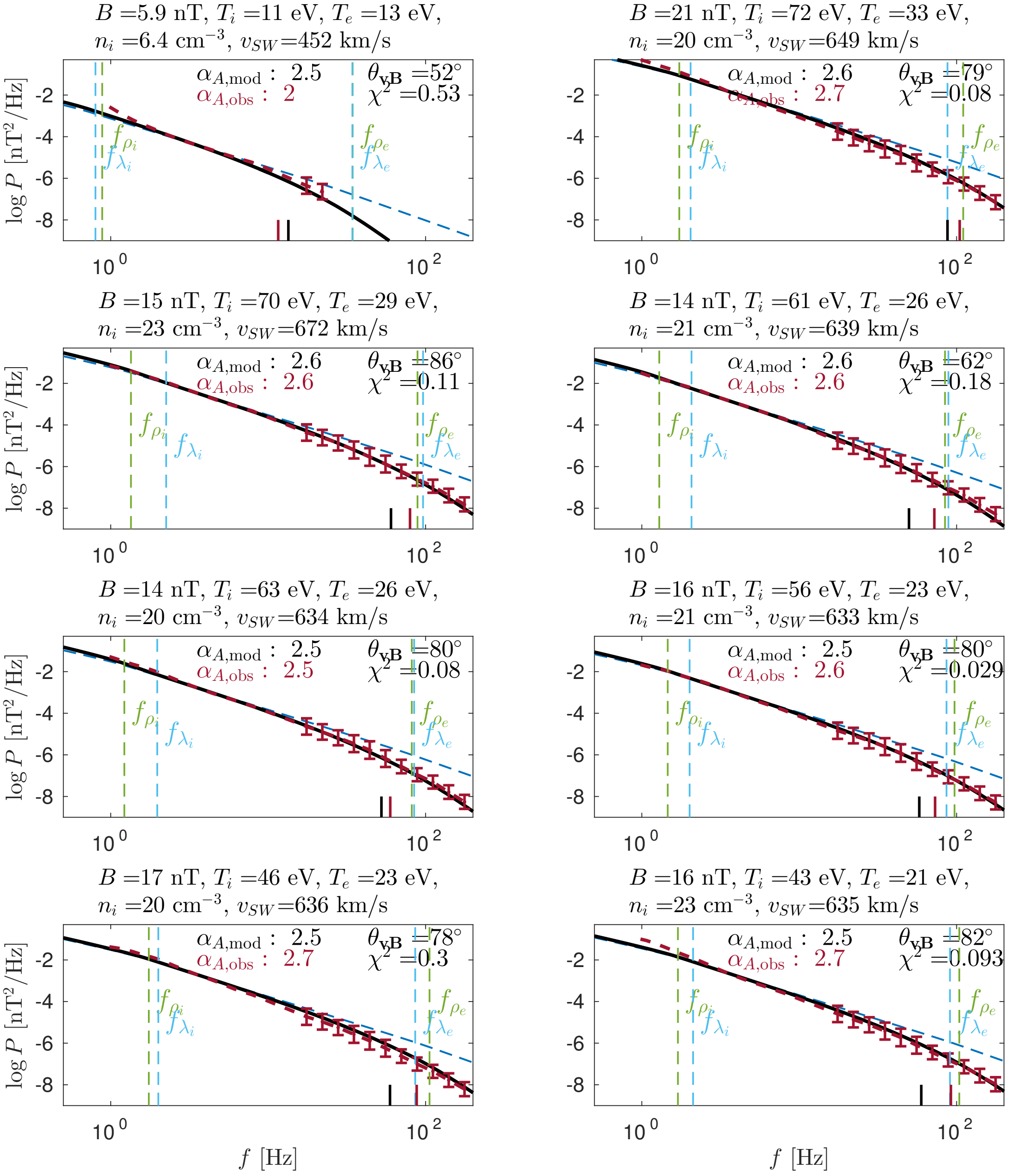

B =5.9 nT, T_i =11 eV, T_e =13 eV, n_i =6.4 cm^{-3}, v_{SW}=452 km/s

B =21 nT, T_i =72 eV, T_e =33 eV, n_i =20 cm^{-3}, v_{SW}=649 km/s

B =15 nT, T_i =70 eV, T_e =29 eV, n_i =23 cm^{-3}, v_{SW}=672 km/s

B =14 nT, T_i =61 eV, T_e =26 eV, n_i =21 cm^{-3}, v_{SW}=639 km/s

B =14 nT, T_i =63 eV, T_e =26 eV, n_i =20 cm^{-3}, v_{SW}=634 km/s

B =16 nT, T_i =56 eV, T_e =23 eV, n_i =21 cm^{-3}, v_{SW}=633 km/s

B =17 nT, T_i =46 eV, T_e =23 eV, n_i =20 cm^{-3}, v_{SW}=636 km/s

B =16 nT, T_i =43 eV, T_e =21 eV, n_i =23 cm^{-3}, v_{SW}=635 km/s

Figure A.8: Same labeling as Figure 4.8.

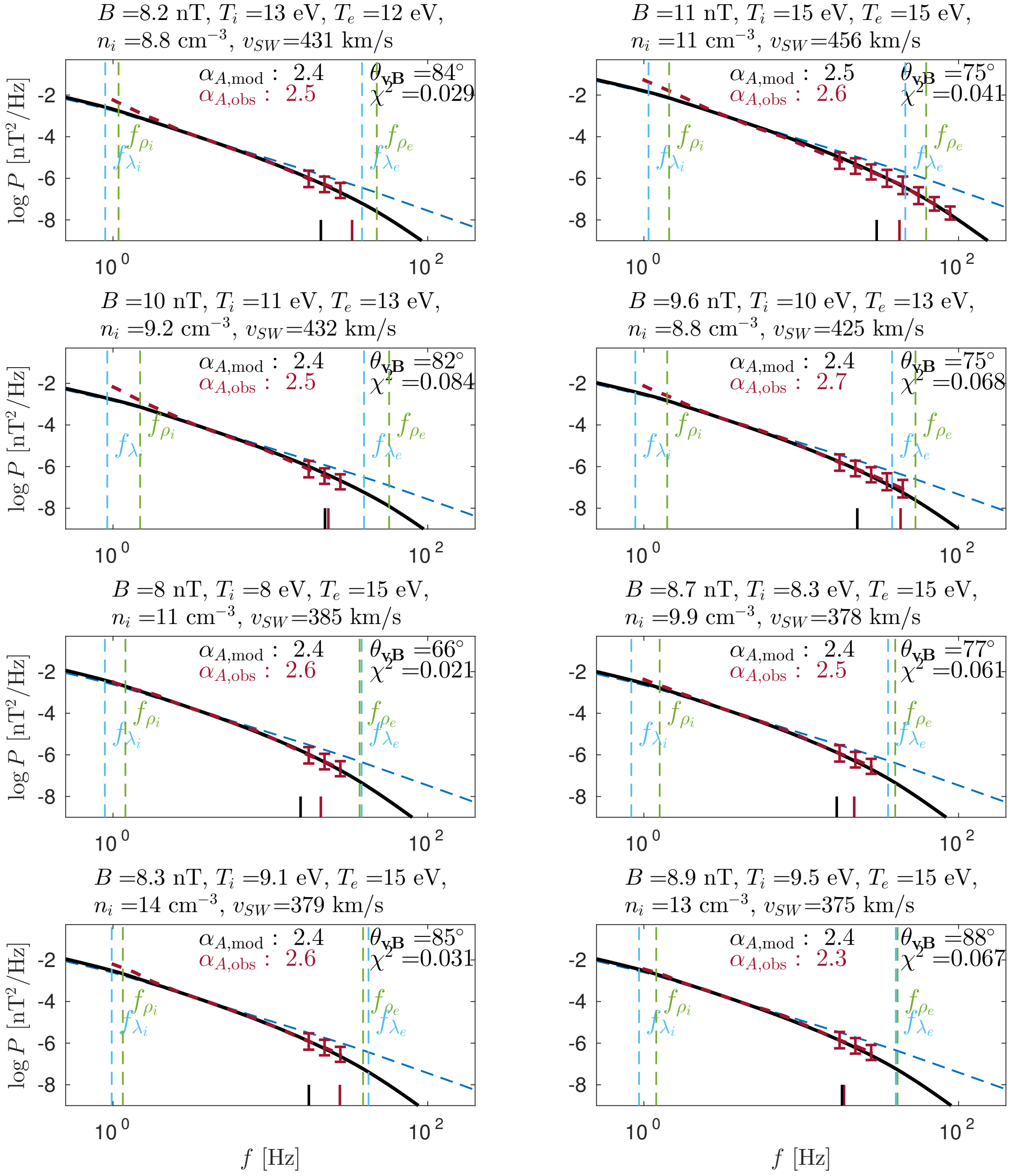

B =8.2 nT, T_i =13 eV, T_e =12 eV, n_i =8.8 cm^{-3}, v_{SW}=431 km/s

B =11 nT, T_i =15 eV, T_e =15 eV, n_i =11 cm^{-3}, v_{SW}=456 km/s

B =10 nT, T_i =11 eV, T_e =13 eV, n_i =9.2 cm^{-3}, v_{SW}=432 km/s

B =9.6 nT, T_i =10 eV, T_e =13 eV, n_i =8.8 cm^{-3}, v_{SW}=425 km/s

B =8 nT, T_i =8 eV, T_e =15 eV, n_i =11 cm^{-3}, v_{SW}=385 km/s

B =8.7 nT, T_i =8.3 eV, T_e =15 eV, n_i =9.9 cm^{-3}, v_{SW}=378 km/s

B =8.3 nT, T_i =9.1 eV, T_e =15 eV, n_i =14 cm^{-3}, v_{SW}=379 km/s

B =8.9 nT, T_i =9.5 eV, T_e =15 eV, n_i =13 cm^{-3}, v_{SW}=375 km/s

Figure A.9: Same labeling as Figure 4.8.

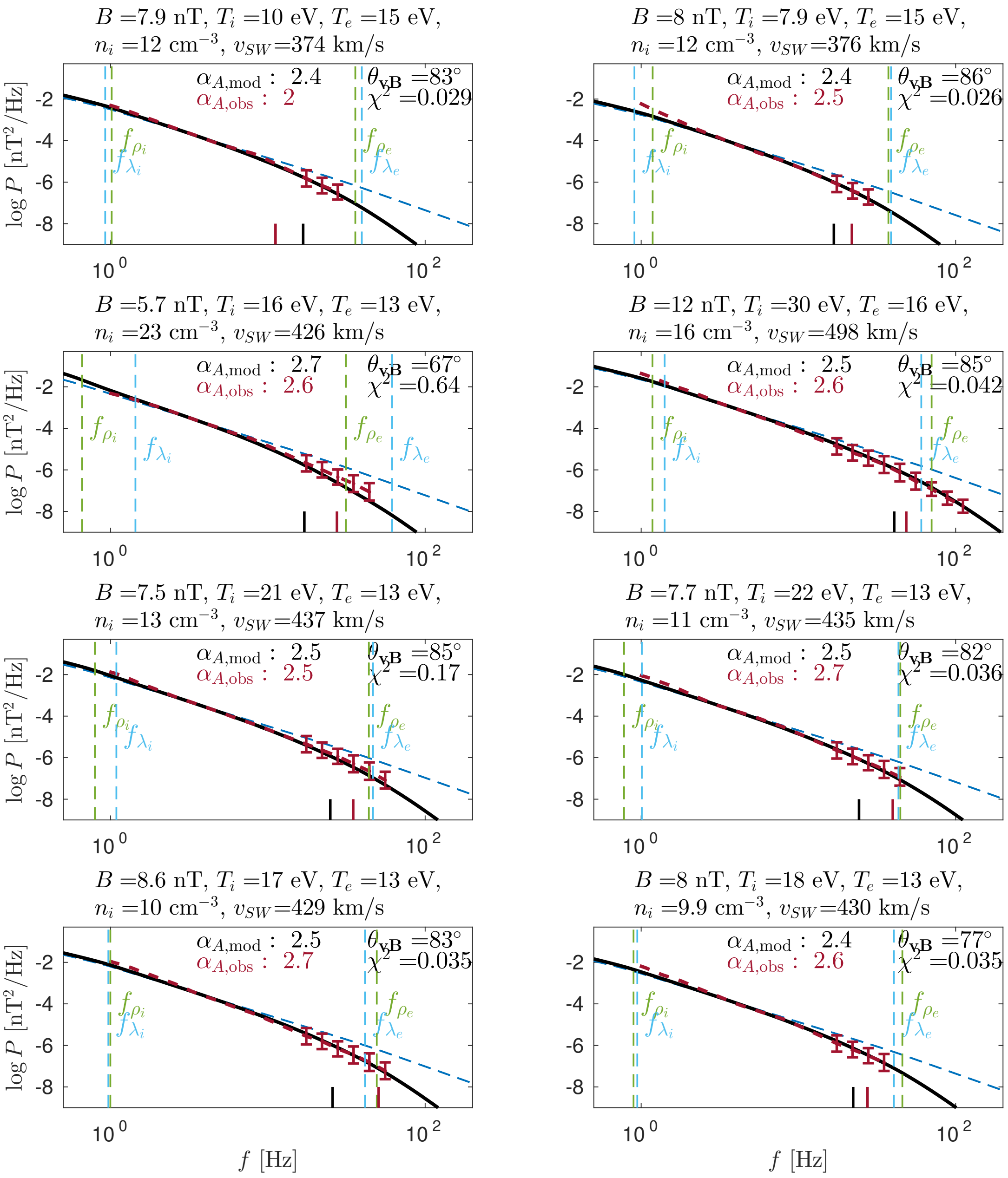

B =7.9 nT, T_i =10 eV, T_e =15 eV, n_i =12 cm^{-3}, v_{SW}=374 km/s

B =8 nT, T_i =7.9 eV, T_e =15 eV, n_i =12 cm^{-3}, v_{SW}=376 km/s

B =5.7 nT, T_i =16 eV, T_e =13 eV, n_i =23 cm^{-3}, v_{SW}=426 km/s

B =12 nT, T_i =30 eV, T_e =16 eV, n_i =16 cm^{-3}, v_{SW}=498 km/s

B =7.5 nT, T_i =21 eV, T_e =13 eV, n_i =13 cm^{-3}, v_{SW}=437 km/s

B =7.7 nT, T_i =22 eV, T_e =13 eV, n_i =11 cm^{-3}, v_{SW}=435 km/s

B =8.6 nT, T_i =17 eV, T_e =13 eV, n_i =10 cm^{-3}, v_{SW}=429 km/s

B =8 nT, T_i =18 eV, T_e =13 eV, n_i =9.9 cm^{-3}, v_{SW}=430 km/s

Figure A.10: Same labeling as Figure 4.8.

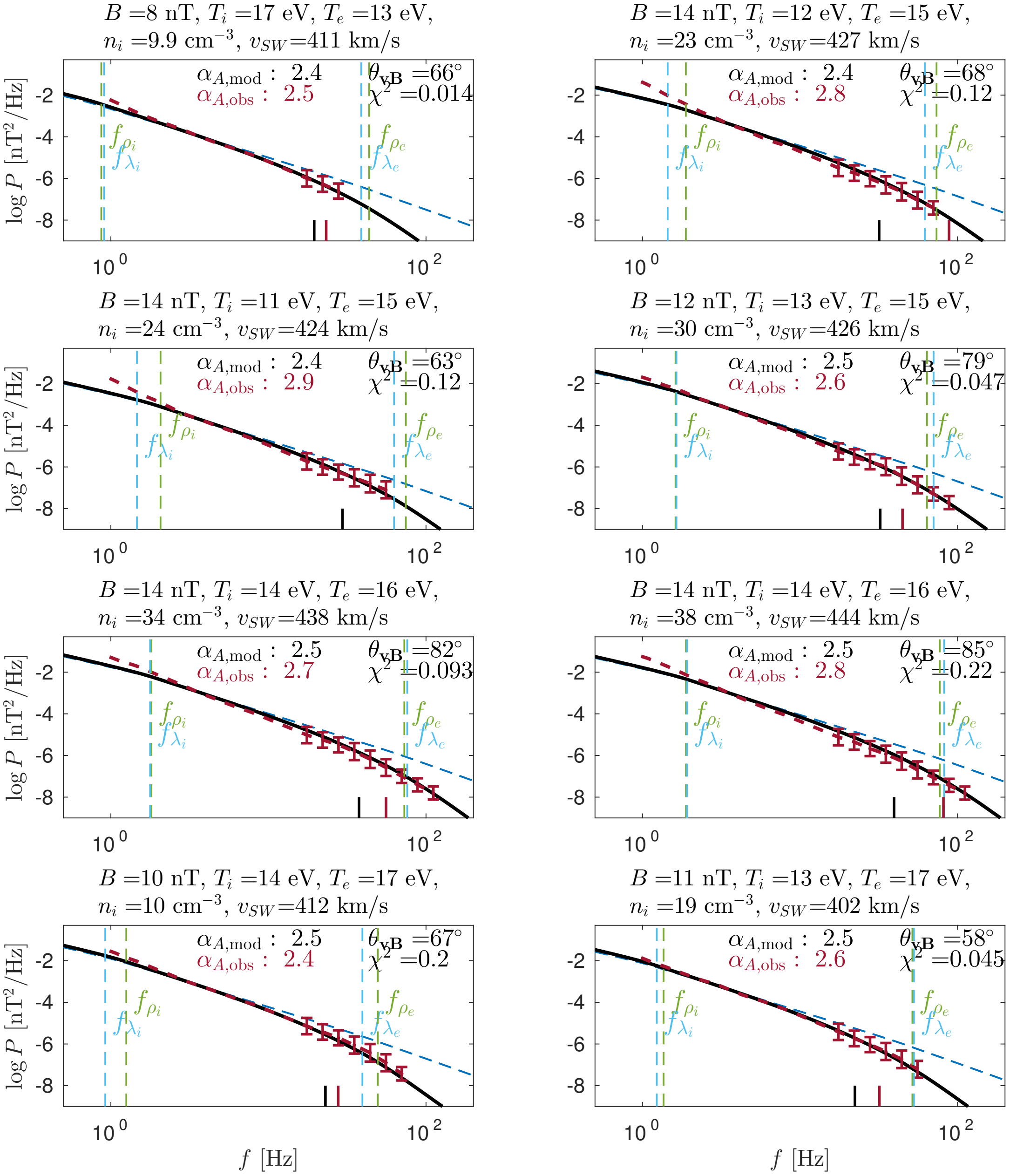

Figure A.11: Same labeling as Figure 4.8.

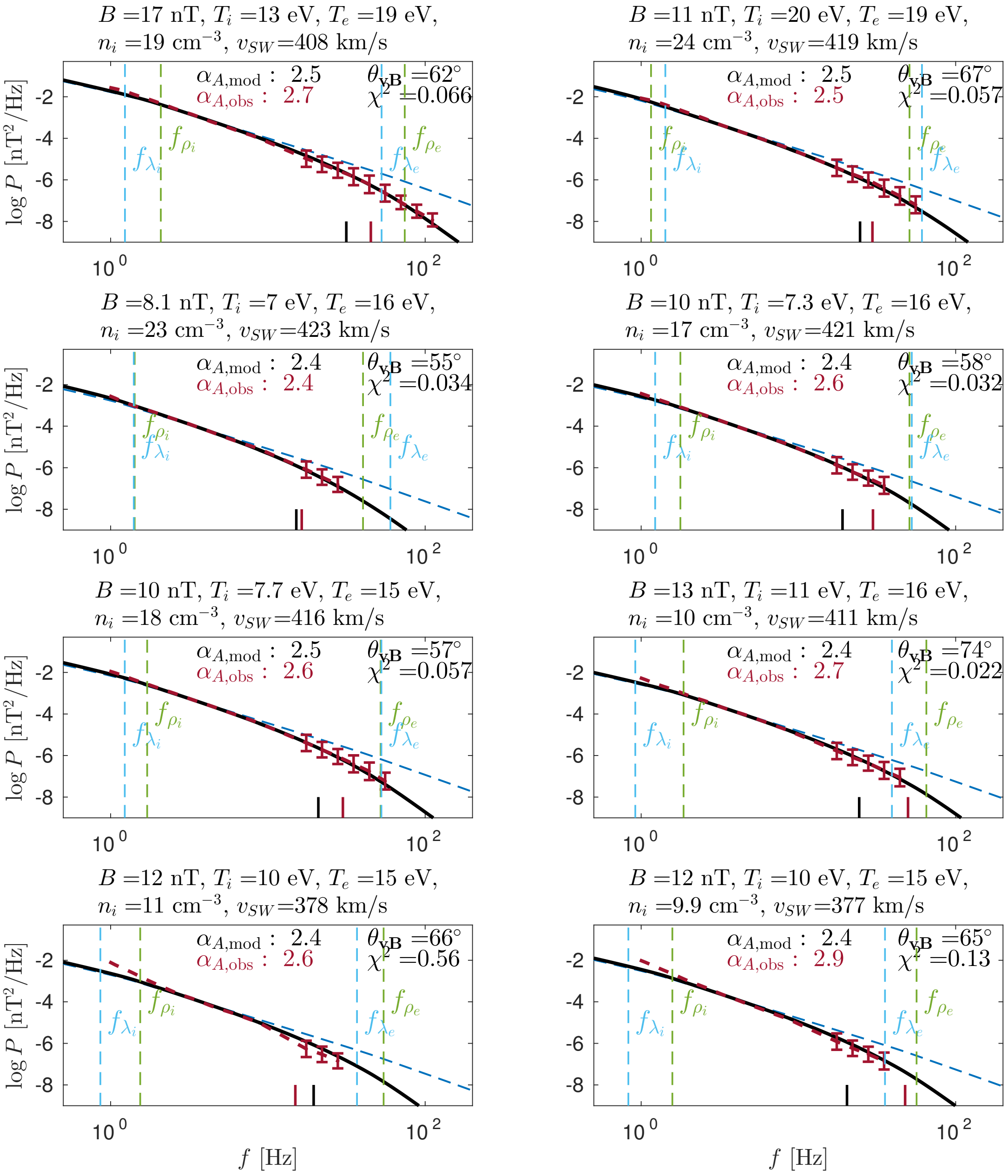

B =17 nT, T_i =13 eV, T_e =19 eV, n_i =19 cm^{-3}, v_{SW}=408 km/s

B =11 nT, T_i =20 eV, T_e =19 eV, n_i =24 cm^{-3}, v_{SW}=419 km/s

B =8.1 nT, T_i =7 eV, T_e =16 eV, n_i =23 cm^{-3}, v_{SW}=423 km/s

B =10 nT, T_i =7.3 eV, T_e =16 eV, n_i =17 cm^{-3}, v_{SW}=421 km/s

B =10 nT, T_i =7.7 eV, T_e =15 eV, n_i =18 cm^{-3}, v_{SW}=416 km/s

B =13 nT, T_i =11 eV, T_e =16 eV, n_i =10 cm^{-3}, v_{SW}=411 km/s

B =12 nT, T_i =10 eV, T_e =15 eV, n_i =11 cm^{-3}, v_{SW}=378 km/s

B =12 nT, T_i =10 eV, T_e =15 eV, n_i =9.9 cm^{-3}, v_{SW}=377 km/s

Figure A.12: Same labeling as Figure 4.8.

A.2 Modeled Power Spectral Densities for Different Energy Distributions

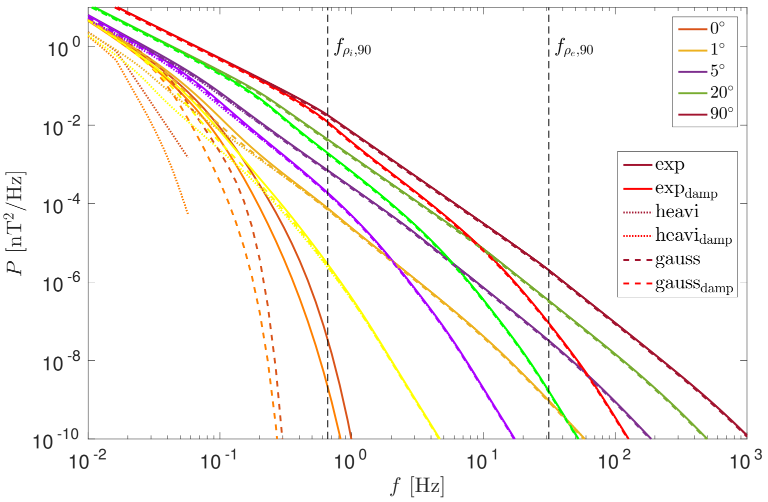

Figure A.13: Power spectral densities for different field-to-flow angles and different realizations of critical balance for the same solar wind parameters as in Figure 4.1. The vertical dashed lines mark the ion and electron gyroradius for a field-to-flow angle of 90°. The darker line of each color gives the result of the exponential energy distribution (solid line), the Heaviside distribution (dotted line), and the Gaussian distribution (dashed line) without damping. The brighter line of each color gives the associated spectrum with KAW damping. Except for 0° and 1°, the power spectral densities for all three energy distributions fall approximately on the same line. The power spectral densities of the Dirac delta function are not shown here, because they have smaller amplitudes than the power spectral densities for the other distributions but follow similar scalings.

List of Figures

2.1 Richardson cascade of hydrodynamic turbulence. The energy is transported from large scales/large eddies to the smaller ones. Figure from Frisch (1995) p. 104. Reproduced by permission of the Camebridge University Press. 9

2.2 Solution ω/Ω_i of linear Maxwell-Vlasov equations as a function of $k\rho_i$: Real part of wave frequency is shown in blue, damping rate γ in red for different angles of propagation $\theta_{\mathbf{kB}}$. The inset shows the same plot with double-logarithmic axes to illustrate the transition from non-dispersive to kinetic regime at wavenumbers $\sim k\rho_i = 1$. Figure from Sahraoui et al. (2012). Reproduced by permission of the American Astronomical Society. 19

2.3 Power spectral density of the magnetic field fluctuations for typical solar wind parameters at 1 AU. Blue and red lines are calculated from ACE measurements; yellow line from Cluster measurements. Instruments and interval lengths are given in the legend. The vertical dashed lines indicate the correlation length λ_c, the ion gyroradius ρ_i, and the electron gyroradius ρ_e. Figure from Kiyani et al. (2015). Reproduced by permission of the Royal Society. 21

2.4 Power spectral densities of the normalized magnetic field $\delta\tilde{\mathbf{b}} = \delta\mathbf{B}/B_0$ in red and the normalized electron density $\delta\tilde{n} \sim \delta n/n_0$ in blue measured by ARTEMIS-P2 on October 11, 2010 from 00:21 to 01.14 UT. Vertical dashed lines mark ion and electron gyroradius and inertial length. Figure from Chen et al. (2013). Reproduced by permission of the American Physical Society. 24

2.5 Contour plot of the two-dimensional correlation function as a function of distance parallel and perpendicular to the magnetic field obtained from 463 intervals of ISEE 3 magnetometer data. The original data in the $r_{\|} > 0$ and $r_{\perp} > 0$ quadrant has been reflected to fill all four quadrants. $r_{\|}$ and $r_{\perp}$ is shown in units of 10^{10} cm. Figure from Matthaeus et al. (1990). Reproduced by permission of the American Geophysical Union. 27

2.6 Wavelet (blue) and Fourier (black) spectrum of magnetic fluctuations obtained from Ulysses data of day 100-200 of 1995. Figure from Wicks et al. (2010). Reproduced by permission of the Oxford University Press. 28

2.7 Spectral index of magnetic power spectral densities in the kinetic regime for fluctuations parallel (red) and perpendicular (blue) with respect to the magnetic field obtained by Chen et al. (2010) from Cluster data. Figure from Chen et al. (2010). Reproduced by permission of the American Physical Society. 29

2.8 Parallel (black, green) and perpendicular (red, blue) magnetic power spectral densities of Cluster FGM data up to 33 Hz and STAFF-SC data for frequencies between 1.5 Hz and 225 Hz measured on 19 March 2006 from 20h30 to 23h20 UT. Dashed and dotted lines give the noise level, respectively. Black arrows indicate characteristic frequencies. Figure from Sahraoui et al. (2009). Reproduced by permission of the American Physical Society. 30

2.9 Magnetic power spectral densities of Cluster STAFF-SC data (green) and STAFF-SA data (red) measured on 2004 January 22. Diamonds mark the STAFF-SA noise level. Blue and black arrows indicate characteristic ion and electron scales. The exponential model $Ak^{-8/3}$ $\exp(-k\rho_e)$ is shown in the black solid line. Figure from Alexandrova et al. (2012). 31

2.10 Results of fitting (2.41) to 100 observed magnetic power spectra. (a) spectral index α in sub-ion range; (b) dissipation length l_d as a function of the spectral index α; (c) dissipation length l_d as a function of the electron gyro radius ρ_e; (d) dissipation length l_d as a function of the electron inertial length. Figure from Alexandrova et al. (2012). Reproduced by permission of the American Astronomical Society. . . 32

2.11 Superposition of 107 solar wind spectra analyzed in Alexandrova et al. (2009, 2012). The spectra are shifted vertically by a parameter $E_0 = \langle E_j(k)/E_1(k)\rangle$, where $\langle ...\rangle$ defines the mean over wavenumbers and $E_1(k)$ a reference spectrum. Characteristic ion and electron scales are marked in black. The blue line gives a power-law $\sim k^{-5/3}$ and the red line shows $\sim k^{-8/3} exp(-k\rho_e)$. Figure from Alexandrova et al. (2012). Reproduced by permission of the American Astronomical Society. 33

3.1 $\overline{\gamma}/\overline{\omega}_r$ for a temperature ratio of $T_i/T_e = 1$ (a) and of $T_i/T_e = 10$ (b) and ion plasma betas of 0.01, 0.1, 1, and 10. Damping rates from the simplified dispersion relation are shown in dashed lines, hot damping rates in solid lines and hot damping rates with Padé approximation in dotted lines. Figure from Schreiner & Saur (2017). 44

3.2 Real part of the wave frequency normalized by the ion gyroradius ω_r/Ω_i for a temperature ratio of (a) $T_i/T_e = 1$ and (b) $T_i/T_e = 10$ and ion plasma betas of 0.01, 0.1, 1, and 10. 45

3.3 Equation (3.20) for $\varepsilon_0 = \{0.01, 0.1, 1, 10\} \times \varepsilon_{0,\mathrm{ref}}$ with $\varepsilon_{0,\mathrm{ref}} = 7 \times 10^{-16}$ $\mathrm{Jm^{-3}s^{-1}}$. The dotted line shows the transition from MHD to the kinetic regime. Solar wind parameters ($B = 15.5\,\mathrm{nT}$, $n = 20\,\mathrm{cm^{-3}}$, $T_i = 61\,\mathrm{eV}$, $T_e = 26\,\mathrm{eV}$, and $v_{SW} = 630\,\mathrm{km/s}$), the break frequency, and $\varepsilon_{0,\mathrm{ref}}$ are taken from observation 5 in Alexandrova et al. (2009). Figure from Schreiner & Saur (2017). 47

3.4 Hot damping rate ($\overline{\gamma}/\overline{\omega}_r$) for all ratios of $k_\parallel$ to $k_\perp$ from Figure 3.3 and the same parameters as in Figure 3.3. All damping rates fall approximately on the same dark blue solid line. Figure from Schreiner & Saur (2017). 48

3.5 Sketch of the role of different energy cascade rates on the energy distribution in k-space (left panels) and on the energy flux $\varepsilon(k)$ (right panel) for hydrodynamic turbulence (top panels) and solar wind turbulence (bottom panels). The different values for the energy cascade rate ε_0 are referred to as ε_1, ε_2, ε_3 with $\varepsilon_1 < \varepsilon_2 < \varepsilon_3$. In panel (c), the energy distribution for solar wind turbulence is assumed to follow critical balance, which implies that larger ε_0 result in larger parallel wavenumbers $k_\parallel$. For KAW larger parallel wavenumbers additionally result in larger damping rates γ for the same $k_\perp$. The larger damping rates γ are indicated by the intensity of the red color in panel (c). The dissipation scales k_d shown in orange in panel (b) and (d) are defined as the scales where the energy is reduced by a factor of $1/e$. Figure from Schreiner & Saur (2017). 50

3.6 The solid line gives the KAW damping rate from Equation (2.32) for the same parameters as in Figure 3.3. $k_\perp^{4/3}$ and $k_\perp^{7/3}$ is shown for comparison. λ_e and ρ_e are marked by the vertical lines. Figure from Schreiner & Saur (2017). 52

3.7 Equation (3.21) for the same parameters as in Figure 3.3 in the brown line. Observations from interval 5 in Alexandrova et al. (2009) are shown in blue dots. Vertical lines indicate the electron scales, where f_{λ_e} corresponds to the Doppler-shifted λ_e with $f_{\lambda_e} = v_{SW}/2\pi\lambda_e$, and f_{ρ_e} to ρ_e with $f_{\rho_e} = v_{SW}/2\pi\rho_e$. Figure from Schreiner & Saur (2017). 53

3.8 Results of fitting Equation (3.29) to 300 model spectra with hot damping rates. The dissipation length l_d is shown as a function of (a) the electron gyroradius ρ_e, and (b) the electron inertial length λ_e. The red dots show the results for $\beta_i = [0.1, 10]$ and $\beta_e = [0.1, 20]$; the black and blue dots show separated results for small ($\beta_i, \beta_e = [0.1, 1]$) and large plasma betas ($\beta_i = [1, 10]$ and $\beta_e = [1, 20]$), respectively. Figure from Schreiner & Saur (2017). 55

4.1 Double logarithmic plot of the energy density as logarithmically equidistant iso-contours calculated with Equations (4.2)-(4.4). A very similar figure can be found in von Papen & Saur (2015), however, for better comparison with the energy distribution with damping, we generated the figure with the following parameters: $B=$ 5.7 nT, L=6 × 10^9 m, $\rho_i=$ 10^5 m, ρ_e=2.2 × 10^3 m, v_{SW}=4 × 10^5 m/s, v_A = 2.5 × 10^4 m/s. Integration planes according to (4.1) are shown as white dashed lines for a field-to-flow angle of 1° for logarithmically equidistant frequencies between 10^{-4} Hz and 10 Hz. 63

4.2 Power spectral densities for different field-to-flow angles in the MHD, KAW, and electron dissipation regime. The Doppler-shifted ion gyroradius and electron gyroradius for a field-to-flow angle of 90° are shown in the black dashed vertical lines. Power-laws with a spectral index of 5/3 and 7/3 are shown for comparison. 64

4.3 Sketch of energy distribution in k-space. The energy is constant over red shells with radius $k_\perp$ and constant along $k_\|$. The energy is transported in the perpendicular direction with velocity v_k and distributed in the parallel direction following critical balance. S_k defines the surface of the shell and $\widetilde{V}_k$ the approximate volume between two shells with radius $k_\perp$ and $k'_\perp = k_\perp + \mathrm{d}k_\perp$. 66

4.4 Double logarithmic plot of the energy density with damping as logarithmically equidistant iso-contours calculated with Equations (4.25)-(4.27) with the same parameters as in Figure 4.1 and with a Kolmogorov constant of $C_K = 3.1$ (The different value of C_K compared to the one-dimensional model will be discussed in Section 4.4). Integration planes according to (4.1) are shown as white dashed lines for field-to-flow angles of 1° and 50° for a frequency of 10 Hz. 70

4.5 Power spectral densities for different field-to-flow angles in the MHD, KAW, and electron dissipation regime with KAW damping. Black dashed lines show power spectra without damping. The Doppler-shifted ion gyroradius and electron gyroradius for a field-to-flow angle of 90° are shown in the black dashed vertical lines. The colored dotted vertical lines show Doppler-shifted $0.3f_{\rho_e}$ for field-to-flow angles of 90° (red), 50° (blue), 20° (green). The numbers on the right give the spectral index fitted between $f_{\rho_i,90}$ and $0.3f_{\rho_e,\theta_{\mathbf{vB}}}$. 71

4.6 Magnetic power spectral densities of 93 intervals in the free solar wind measured with the Cluster-1/STAFF-SC sensor for $f=[0.5,9]$ Hz and the STAFF-SA instrument for $f \geq 8$ Hz analyzed by Alexandrova et al. (2012). The spectra are analyzed for frequencies where the signal-to-noise ratio is larger than 3. 73

4.7 Most intense spectrum of the 93 observed intervals. The model without damping is shown in the blue dashed line, the model with damping in the black line, and the observations with error bars in the red dashed line. The vertical dashed lines mark the Doppler-shifted electron and ion gyroradius and inertial length. The measured plasma parameters are B=5.7 Hz, T_i = 72 eV, T_e= 33 eV, n_i =20 cm^{-3}, and v_{SW}=650 km/s. $\alpha_{A,\mathrm{mod}}$ and $\alpha_{A,\mathrm{obs}}$ give the spectral index in the sub-ion range of the model and the observations, respectively, obtained by fitting $P_A(k_\perp) = Ak_\perp^{-\alpha_A}\exp(-k_\perp l_d)$ to the spectra. The black and red vertical lines give the frequency of the dissipation length $f_d = v_{SW}/2\pi l_d$ for the model and the observation, respectively. 75

4.8 Exemplary intervals of group 1: Model and observation have different spectral indices and do not agree well. The labeling is the same as in Figure 4.7. Solar wind plasma parameters are given at the top of each panel. 8.6% of 93 intervals belong to this group. 77

4.9 $\mathrm{rms}^2 = 1/N \sum_{i=1}^{N} \left[\log_{10}(d(i)) - \log_{10}(m(i))\right]^2$ for all observed power spectral densities $d(i)$ and associated modeled power spectral densities $m(i)$ as a function of the magnetic field (a), the ion temperature (b), the electron temperature (c), the solar wind velocity (d), and the plasma density (e) for intervals with $\alpha_{A,\mathrm{obs}} > \alpha_{A,\mathrm{mod}}$. 78

4.10 Exemplary intervals of group 2: The spectral slope in the observations is shallower than in the model. The labeling is the same as in Figure 4.7. Solar wind plasma parameters are given at the top of each panel. 11.8% of 93 intervals belong to this group. 79

4.11 Exemplary intervals of group 3: Model and observations are in general agreement but the spectral slope of the observations is steeper than in the model. The labeling is the same as in Figure 4.7. Solar wind plasma parameters are given at the top of each panel. 54.8% of 93 intervals belong to this group. 80

4.12 Spectral index in the sub-ion range of the observations $\alpha_{A,\mathrm{obs}}$ as a function of the spectral index of the model $\alpha_{A,\mathrm{mod}}$ (a), and observed dissipation length $l_{d,\mathrm{obs}}$ as a function of the modeled one $l_{d,\mathrm{mod}}$ (b). . . 81

4.13 Exemplary intervals of group 4: Model and observation are in good agreement including matching spectral indices. The labeling is the same as in Figure 4.7. Solar wind plasma parameters are given at the top of each panel. 24.7% of 93 intervals belong to this group. 82

A.1 Same labeling as Figure 4.8. 91
A.2 Same labeling as Figure 4.8. 92
A.3 Same labeling as Figure 4.8. 93
A.4 Same labeling as Figure 4.8. 94
A.5 Same labeling as Figure 4.8. 95
A.6 Same labeling as Figure 4.8. 96
A.7 Same labeling as Figure 4.8. 97
A.8 Same labeling as Figure 4.8. 98
A.9 Same labeling as Figure 4.8. 99
A.10 Same labeling as Figure 4.8. 100
A.11 Same labeling as Figure 4.8. 101

A.12 Same labeling as Figure 4.8. 102

A.13 Power spectral densities for different field-to-flow angles and different realizations of critical balance for the same solar wind parameters as in Figure 4.1. The vertical dashed lines mark the ion and electron gyroradius for a field-to-flow angle of 90°. The darker line of each color gives the result of the exponential energy distribution (solid line), the Heaviside distribution (dotted line), and the Gaussian distribution (dashed line) without damping. The brighter line of each color gives the associated spectrum with KAW damping. Except for 0° and 1°, the power spectral densities for all three energy distributions fall approximately on the same line. The power spectral densities of the Dirac delta function are not shown here, because they have smaller amplitudes than the power spectral densities for the other distributions but follow similar scalings. 103

Bibliography

Abramowitz, M., & I. A. Stegun (1964), Handbook of Mathematical Functions: with Formulas, Graphs, and Mathematical Tables, Dover, New York.

Alexandrova, O., & V. Carbone (2008), Small-Scale Energy Cascade of the Solar Wind Turbulence, Astrophys. J., 674, 1153–1157.

Alexandrova, O., C. Lacombe, & A. Mangeney (2008), Spectra and Anisotropy of Magnetic Fluctuations in the Earth's Magnetosheath: Cluster Observations, Ann. Geophys., 26(11), 3585–3596, doi: 10.5194/angeo-26-3585-2008.

Alexandrova, O., J. Saur, C. Lacombe, A. Mangeney, J. Mitchell, S. Schwartz, & P. Robert (2009), Universality of Solar-Wind Turbulent Spectrum from MHD to Electron Scales, Phys. Rev. Lett., 103(16), 14–17, doi: 10.1103/PhysRevLett.103.165003.

Alexandrova, O., C. Lacombe, A. Mangeney, R. Grappin, & M. Maksimovic (2012), Solar Wind Turbulent Spectrum At Plasma Kinetic Scales, Astrophys. J., 760(2), 121, doi: 10.1088/0004-637X/760/2/121.

Alexandrova, O., S. D. Bale, & L. C (2013), Comment on "Evidence of a Cascade and Dissipation of Solar-Wind Turbulence at the Electron Gyroscale", 111, 149,001, doi: 10.1103/PhysRevLett.111.149001.

Bale, S. D., P. J. Kellogg, F. S. Mozer, T. S. Horbury, & H. Reme (2005), Measurement of the Electric Fluctuation Spectrum of Magnetohydrodynamic Turbulence, Phys. Rev. Lett., 94(21), 215,002/1–215,002/4, doi: 10.1103/PhysRevLett.94.215002.

Baumjohann, W., & R. A. Treumann (2012), Basic Space Plasma Physics: Revised Edition, Imperial College Press, London.

Belcher, J. W., & J. L. Davis (1971), Large-Amplitude Alfvén Waves in the Interplanetary Medium, J. Geophys. Res., 76(16), 3534–3563.

Beresnyak, A. (2011), Spectral Slope and Kolmogorov Constant of MHD Turbulence, Phys. Rev. Lett., 106(7), 075,001, doi: 10.1103/PhysRevLett.106.075001.

Bieber, J. (1996), Dominant Two-Dimensional Solar Wind Turbulence with Implications for Cosmic Ray Transport, J. Geophys. Res., 101, 2511–2522.

Biskamp, D. (1993), Nonlinear Magnetohydrodynamics, Cambridge University Press, Cambridge, doi: 10.1088/0029-5515/38/8/701.

Boldyrev, S., & J. C. Perez (2012), Spectrum of Kinetic Alfven Turbulence, Astrophys. J., 758, 1–5, doi: 10.1088/2041-8205/758/2/L44.

Briand, C. (2009), Plasma Waves above the Ion Cyclotron Frequency in the Solar Wind: A Review on Observations, Nonlinear Process. Geophys., 16, 319–329.

Bruno, R., & L. Trenchi (2014), Radial Dependence of the Frequency Break Between Fluid and Kinetic Scales in the Solar Wind Fluctuations, Astrophys. J., 787(2), L24, doi: 10.1088/2041-8205/787/2/L24.

Chen, C., S. Boldyrev, Q. Xia, & J. Perez (2013), Nature of Subproton Scale Turbulence in the Solar Wind, Phys. Rev. Lett., 225002, 1–5, doi: 10.1103/PhysRevLett.110.225002.

Chen, C. H. K., T. S. Horbury, A. A. Schekochihin, R. T. Wicks, O. Alexandrova, & J. Mitchell (2010), Anisotropy of Solar Wind Turbulence between Ion and Electron Scales, Phys. Rev. Lett., 104(25), 1–4, doi: 10.1103/PhysRevLett.104.255002.

Chen, C. H. K., A. Mallet, T. A. Yousef, A. A. Schekochihin, & T. S. Horbury (2011), Anisotropy of Alfvénic Turbulence in the Solar Wind and Numerical Simulations, Mon. Not. R. Astron. Soc., 415(4), 3219–3226, doi: 10.1111/j.1365-2966.2011.18933.x.

Chen, C. H. K., L. Leung, S. Boldyrev, B. A. Maruca, & S. D. Bale (2014), Ion-Scale Spectral Break of Solar Wind Turbulence at High and Low Beta, Geophys. Res. Lett., 41(22), 8081–8088, doi: 10.1002/2014GL062009.

Chen, F. F. (1974), Introduction to Plasma Physics and Controlled Fusion: Plasma Physics, vol. 1, Springer, New York.

Cho, J., & A. Lazarian (2004), The Anisotropy of Electron MHD Turbulence, Astrophys. J., 615(1), L41–L44, doi: 10.1086/425215.

Cho, J., A. Lazarian, & E. T. Vishniac (2002), Simulations of Magnetohydrodynamic Turbulence in a Strongly Magnetized Medium, Astrophys. J., 564, 291–301, doi: 10.1086/324186.

Coleman JR., P. J. (1968), Turbulence, Viscosity, and Dissipation in the Solar-Wind Plasma, Astrophys. J., 153, 371–388, doi: 10.1086/149674.

Corrsin, S. (1964), Further Generalization of Onsager's Cascade Model for Turbulent Spectra, Phys. Fluids, 7(10), 1156–1159, doi: 10.1063/1.1711355.

Denskat, K. U., H. J. Beinroth, & F. M. Neubauer (1983), Interplanetary Magnetic Field Power Spectra with Frequencies from 2.4×10^{-5} Hz to 470 Hz from HELIOS-Observations during Solar Minimum Conditions, J. Geophys., 54, 60–67.

Drake, R. P. (2006), High-Energy-Density Physics, Springer, Berlin.

Elsässer, W. M. (1950), The Hydromagnetic Equations, Phys. Rev., 79(1), 183, doi: 10.1103/PhysRev.79.183.

Feldman, W. C., J. R. Asbridge, S. J. Bame, & M. D. Montgomery (1973), Double Ion Streams in the Solar Wind, J. Geophys. Res., 78(13), 2017, doi: 10.1029/JA078i013p02017.

Fredricks, R. W., & F. V. Coroniti (1976), Ambiguities in the Deduction of Rest Frame Fluctuation Spectrums from Spectrums Computed in Moving Frames, J. Geophys. Res., 81(31), 5591–5595, doi: 10.1029/JA081i031p05591.

Fried, B. D., & S. D. Conte (1961), The Plasma Dispersion Function, Academic Press, New York.

Frisch, U. (1995), Turbulence - The Legacy of A.N. Kolmogorov, Cambridge University Press, New York.

Gary, P. S., & C. W. Smith (2009), Short-Wavelength Turbulence in the Solar Wind: Linear Theory of Whistler and Kinetic Alfvén fluctuations, J. Geophys. Res. Sp. Phys., 114(12), 1–7, doi: 10.1029/2009JA014525.

Goldreich, P., & S. Sridhar (1995), Toward a Theory of Interstellar Turbulence. 2: Strong Alfvénic Turbulence, Astrophys. J., 438, 763–775, doi: 10.1086/175121.

Goodrich, C. C., & A. J. Lazarus (1976), Suprathermal Protons in the Interplanetary Solar Wind, J. Geophys. Res., 81(16), 2750–2754, doi: 10.1029/JA081i016p02750.

He, J., E. Marsch, C. Tu, S. Yao, & H. Tian (2011), Possible Evidence of Alfvén-Cyclotron Waves in the Angle Distribution of Magnetic Helicity of Solar Wind Turbulence, Astrophys. J., 731(2), 85, doi: 10.1088/0004-637X/731/2/85.

He, J., C. Tu, E. Marsch, & S. Yao (2012), Do Oblique Alfvén/Ion-Cyclotron or Fast-Mode/Whistler Waves Dominate the Dissipation of Solar Wind Turbulence near the Proton Inertial Length?, Astrophys. J., 745(1), L8, doi: 10.1088/2041-8205/745/1/L8.

He, J., C. Tu, E. Marsch, S. Bourouaine, & Z. Pei (2013), Radial Evolution of the Wavevector Anisotropy of Solar Wind Turbulence Between 0.3 and 1 AU, Astrophys. J., 773(1), 72, doi: 10.1088/0004-637X/773/1/72.

Horbury, T. S., A. Balogh, R. J. Forsyth, & E. J. Smith (1996), The Rate of Turbulent Evolution over the Sun's Poles, Annu. Rev. Astron. Astrophys., 316, 333–341.

Horbury, T. S., M. Forman, & S. Oughton (2008), Anisotropic Scaling of Magnetohydrodynamic Turbulence, Phys. Rev. Lett., 101(17), 175,005/1–175,005/4, doi: 10.1103/PhysRevLett.101.175005.

Horbury, T. S., R. T. Wicks, & C. H. K. Chen (2012), Anisotropy in Space Plasma Turbulence: Solar Wind Observations, Space Sci. Rev., 172(1-4), 325–342, doi: 10.1007/s11214-011-9821-9.

Howes, G. G. (2015), A Dynamical Model of Plasma Turbulence in the Solar Wind, Phil. Trans. R. Soc. A, 373, doi: 10.1098/rsta.2014.0145.

Howes, G. G., S. C. Cowley, W. Dorland, G. W. Hammett, E. Quataert, & A. A. Schekochihin (2006), Astrophysical Gyrokinetics: Basic Equations and Linear Theory, Astrophys. J., 651(1), 590, doi: 10.1086/506172.

Howes, G. G., S. C. Cowley, W. Dorland, G. W. Hammett, E. Quataert, & A. A. Schekochihin (2008), A Model of Turbulence in Magnetized Plasmas: Implications for the Dissipation Range in the Solar Wind, J. Geophys. Res., 113(A5), A05,103, doi: 10.1029/2007JA012665.

Howes, G. G., J. M. Tenbarge, W. Dorland, E. Quataert, A. A. Schekochihin, R. Numata, & T. Tatsuno (2011), Gyrokinetic Simulations of Solar Wind Turbulence from Ion to Electron Scales, Phys. Rev. Lett., 107(3), 1–4, doi: 10.1103/PhysRevLett.107.035004.

Howes, G. G., S. D. Bale, K. G. Klein, C. H. K. Chen, C. S. Salem, & J. M. TenBarge (2012), The Slow-Mode Nature of Compressible Wave Power in Solar Wind Turbulence, Astrophys. J., 753(1), L19, doi: 10.1088/2041-8205/753/1/L19.

Howes, G. G., K. G. Klein, & J. M. TenBarge (2014), The Quasilinear Premise for the Modeling of Plasma Turbulence, arXiv Prepr.

Hundhausen, A. J., S. J. Bame, J. R. Asbridge, & S. J. Sydoriak (1970), Solar Wind Proton Properties: Vela 3 Observations from July 1965 to June 1967, J. Geophys. Res., 75, 4643, doi: 10.1029/JA075i025p04643.

Karimabadi, H., et al. (2013), Coherent Structures, Intermittent Turbulence, and Dissipation in High-Temperature Plasmas, Phys. Plasmas, 20(1), doi: 10.1063/1.4773205.

Kiyani, K. H., S. C. Chapman, Y. V. Khotyaintsev, M. W. Dunlop, & F. Sahraoui (2009), Global Scale-Invariant Dissipation in Collisionless Plasma Turbulence, Phys. Rev. Lett., 103(7), 2007–2010, doi: 10.1103/PhysRevLett.103.075006.

Kiyani, K. H., S. C. Chapman, F. Sahraoui, B. Hnat, O. Fauvarque, & Y. V. Khotyaintsev (2013), Enhanced Magnetic Compressibility and Isotropic Scale Invariance At Sub-Ion Larmor Scales in Solar Wind Turbulence, Astrophys. J., 763(1), 10, doi: 10.1088/0004-637X/763/1/10.

Kiyani, K. H., K. T. Osman, & S. C. Chapman (2015), Dissipation and Heating in Solar Wind Turbulence : from the Macro to the Micro and Back Again, Phil. Trans. R. Soc. A, 373, 1–10, doi: 10.1098/rsta.2014.0155.

Kolmogorov, A. N. (1941a), The Local Structure of Turbulence in Incompressible Viscous Fluid for Very Large Reynolds Numbers, Dokl. Akad. Nauk SSSR, 30, 299.

Kolmogorov, A. N. (1941b), On Degeneration of Isotropic Turbulence in an Incompressible Viscous Liquid, Dokl. Akad. Nauk SSSR, 31, 538.

Kolmogorov, A. N. (1941c), Dissipation of Energy in Locally Isotropic Turbulence, Dokl. Akad. Nauk SSSR, 32, 16.

Kolmogorov, A. N. (1941d), On the Logarithmically Normal Law of Distribution of the Size of Particles under Pulverization, Dokl. Akad. Nauk SSSR, 31, 99.

Kovasznay, L. S. G. (1948), The Spectrum of Locally Isotropic Turbulence, Phys. Rev., 73, 1115–1116, doi: 10.1103/PhysRev.73.1115.

Lacombe, C., O. Alexandrova, L. Matteini, O. Santolík, N. Cornilleau-Wehrlin, A. Mangeney, Y. de Conchy, & M. Maksimovic (2014), Whistler Mode Waves and the Electron Heat Flux in the Solar Wind: *Cluster* Observations, Astrophys. J., 796(1), 5, doi: 10.1088/0004-637X/796/1/5.

Leamon, R. J., C. W. Smith, N. F. Ness, W. H. Matthaeus, & H. K. Wong (1998a), Observational Constraints on the Dynamics of the Interplanetary Magnetic Field Dissipation Range, J. Geophys. Res., 103(A3), 4775–4787., doi: 10.1029/97JA03394.

Leamon, R. J., W. H. Matthaeus, C. W. Smith, & H. K. Wong (1998b), Contribution of Cyclotron-Resonant Damping to Kinetic Dissipation of Interplanetary Turbulence, Astrophys. J., (1), 181–184, doi: 10.1086/311698.

Leamon, R. J., C. W. Smith, N. F. Ness, & H. K. Wong (1999), Dissipation Range Dynamics: Kinetic Alfven Waves and the Importance of β_e, J. Geophys. Res, pp. 1–17.

Leamon, R. J., W. H. Matthaeus, C. W. Smith, G. P. Zank, D. J. Mullan, & S. Oughton (2000), MHD-Driven Kinetic Dissipation in the Solar Wind and Corona, Astrophys. J., 537, 1054–1062, doi: 10.1086/309059.

Li, G., B. Miao, Q. Hu, & G. Qin (2011), Effect of Current Sheets on the Solar Wind Magnetic Field Power Spectrum from the Ulysses Observation: From Kraichnan to Kolmogorov Scaling, Phys. Rev. Lett., 106(12), 125,001, doi: 10.1103/PhysRevLett.106.125001.

Lion, S., O. Alexandrova, & A. Zaslavsky (2016), Coherent Events and Spectral Shape At Ion Kinetic Scales in the Fast Solar Wind Turbulence, Astrophys. J., 824(1), 47, doi: 10.3847/0004-637X/824/1/47.

Luo, Q. Y., & D. J. Wu (2010), Observations of Anisotropic Scaling of Solar Wind Turbulence, Astrophys. J., 714(1), L138–L141, doi: 10.1088/2041-8205/714/1/L138.

Lysak, R., & W. Lotko (1996), On the Kinetic Dispersion Relation for Shear Alfvén Waves, J. Geophys. Res., 101(A3), 5085–5094.

Marsch, E., K.-H. Mühlhäuser, R. Schwenn, H. Rosenbauer, W. Pilipp, & F. M. Neubauer (1982), Solar Wind Protons: Three-Dimensional Velocity Distributions and Derived Plasma Parameters Measured between 0.3 and 1 AU, J. Geophys. Res., 87(1), 52–72, doi: 10.1029/JA087iA01p00052.

Matthaeus, W. H., & M. L. Goldstein (1982), Stationarity of Magnetohydrodynamic Fluctuations in the Solar Wind, J. Geophys. Res., 87(2), 347–354.

Matthaeus, W. H., & M. L. Goldstein (1986), Low-Frequency $1/f$ Noise in the Interplanetary Magnetic Field, Phys. Rev. Lett., 57(4), 495–498, doi: 10.1103/PhysRevLett.57.495.

Matthaeus, W. H., M. L. Goldstein, & C. Smith (1982), Evaluation of Magnetic Helicity in Homogeneous Turbulence, Phys. Rev. Lett., 48(18), 1256–1259, doi: 10.1103/PhysRevLett.48.1256.

Matthaeus, W. H., M. L. Goldstein, & D. A. Roberts (1990), Evidence for the Presence of Quasi-Two-Dimensional Nearly Incompressible Fluctuations in the Solar Wind, J. Geophys. Res., 95(A12), 673–683, doi: 10.1029/JA095iA12p20673.

Monin, A. S., & A. M. Yaglom (1975), Statistical Fluid Mechanics: Mechanics of Turbulence, vol. 2, MIT Press, Cambridge, MA.

Narita, Y. (2015), Non-Elliptic Wavevector Anisotropy for Magnetohydrodynamic Turbulence, Ann. Geophys., 33(11), 1413–1419, doi: 10.5194/angeo-33-1413-2015.

Narita, Y., & E. Marsch (2015), Kinetic Slow Mode in the Solar Wind and its Possible Role in Turbulence Dissipation and Ion Heating, Astrophys. J., 805(1), 24, doi: 10.1088/0004-637X/805/1/24.

Narita, Y., K. H. Glassmeier, & R. A. Treumann (2006), Wave-Number Spectra and Intermittency in the Terrestrial Foreshock Region, Phys. Rev. Lett., 97(19), 1–4, doi: 10.1103/PhysRevLett.97.191101.

Narita, Y., K. H. Glassmeier, F. Sahraoui, & M. L. Goldstein (2010), Wave-Vector Dependence of Magnetic-Turbulence Spectra in the Solar Wind, Phys. Rev. Lett., 104(17), 1–4, doi: 10.1103/PhysRevLett.104.171101.

Osman, K. T., & T. S. Horbury (2009), Multi-Spacecraft Measurement of Anisotropic Power Levels and Scaling in Solar Wind Turbulence, Ann. Geophys., 27(8), 3019–3025, doi: 10.5194/angeo-27-3019-2009.

Pao, Y.-H. (1965), Structure of Turbulent Velocity and Scalar Fields at Large Wavenumbers, Phys. Fluids, 8, 1063–1075, doi: 10.1063/1.1761356.

Perri, S., & A. Balogh (2010), Stationarity in Solar Wind Flows, Astrophys. J., 714(1), 937–943, doi: 10.1088/0004-637X/714/1/937.

Podesta, J. J. (2009), Dependence of Solar-Wind Power Spectra on the Direction of the Local Mean Magnetic Field, Astrophys. J., 698(2), 986–999, doi: 10.1088/0004-637X/698/2/986.

Podesta, J. J., J. E. Borovsky, & S. P. Gary (2010), A Kinetic Alfvén Wave Cascade Subject to Collisionless Damping cannot Reach Electron Scales in the Solar Wind at 1 AU, Astrophys. J., 712(1), 685–691, doi: 10.1088/0004-637X/712/1/685.

Richardson, L. F. (1922), Weather Prediction by Numerical Process, Cambridge University Press, Cambridge.

Roberts, O. W., X. Li, & B. Li (2013), Kinetic Plasma Turbulence in the Fast Solar Wind Measured by Cluster, Astrophys. J., 769(1), 58, doi: 10.1088/0004-637X/769/1/58.

Rönnmark, K. (1982), WHAMP-Waves in Homogeneous, Anisotropic, Multicomponent Plasmas.

Sahraoui, F., P. Robert, & Y. V. Khotyaintsev (2009), Evidence of a Cascade and Dissipation of Solar-Wind Turbulence at the Electron Gyroscale, Phys. Rev. Lett., 102(23), 1, doi: 10.1103/PhysRevLett.102.231102.

Sahraoui, F., M. L. Goldstein, G. Belmont, P. Canu, & L. Rezeau (2010), Three Dimensional Anisotropic k Spectra of Turbulence at Subproton Scales in the Solar Wind, Phys. Rev. Lett., 105(13), 131,101, doi: 10.1103/PhysRevLett.105.131101.

Sahraoui, F., G. Belmont, & M. L. Goldstein (2012), New Insight into Short-Wavelength Solar Wind Fluctuations from Vlasov Theory, Astrophys. J., 748(2), 100, doi: 10.1088/0004-637X/748/2/100.

Sahraoui, F., S. Y. Huang, G. Belmont, M. L. Goldstein, A. Rétino, P. Robert, & J. De Patoul (2013), Scaling of the Electron Dissipation Range of Solar Wind Turbulence, Astrophys. J., 777, 15, doi: 10.1088/0004-637X/777/1/15.

Salem, C., A. Mangeney, S. D. Bale, & P. Veltri (2009), Solar Wind Magnetohydrodynamics Turbulence: Anomalous Scaling and Role of Intermittency, Astrophys. J., 702(1), 537–553, doi: 10.1088/0004-637X/702/1/537.

Salem, C. S., G. G. Howes, D. Sundkvist, S. D. Bale, C. C. Chaston, C. H. K. Chen, & F. S. Mozer (2012), Identification of Kinetic Alfvén Wave Turbulence in the Solar Wind, Astrophys. J., 745(1), L9, doi: 10.1088/2041-8205/745/1/L9.

Schekochihin, A. A., S. C. Cowley, W. Dorland, G. W. Hammett, G. G. Howes, E. Quataert, & T. Tatsuno (2009), Astrophysical Gyrokinetics: Kinetic and Fluid Turbulent Cascades in Magnetized Weakly Collisional Plasmas, Astrophys. J. Suppl. Ser., 182(1), 310, doi: 10.1088/0067-0049/182/1/310.

Schekochihin, A. A., J. T. Parker, E. G. Highcock, P. J. Dellar, W. Dorland, & G. W. Hammett (2016), Phase Mixing versus Nonlinear Advection in Drift-Kinetic Plasma Turbulence, J. Plasma Phys., 82, doi: 10.1017/S0022377816000374.

Schreiner, A., & J. Saur (2017), A Model for Dissipation of Solar Wind Magnetic Turbulence By Kinetic Alfvén Waves at Electron Scales: Comparison with Observations, Astrophys. J., 3(2), 1, doi: 10.3847/1538-4357/835/2/133.

Shebalin, J., W. Matthaeus, & D. Montgomery (1983), Anisotropy in MHD Turbulence due to a Mean Magnetic Field, J. Plasma Phys., 29(3), 525–547, doi: 10.1017/S0022377800000933.

Smith, C. W., K. Hamilton, B. J. Vasquez, R. J. Leamon, & S. E. T. Al (2006), Dependence of the Dissipation Range Spectrum of Interplanetary Magnetic Fluctuations on the Rate of Energy Cascade, Astrophys. J., 645, 85–88.

Smith, C. W., B. J. Vasquez, & J. V. Hollweg (2012), Observational Constraints on the Role of Cyclotron Damping and Kinetic Alfvén Waves in the Solar Wind, Astrophys. J., 745(1), 8, doi: 10.1088/0004-637X/745/1/8.

Sridhar, S., & P. Goldreich (1994), Toward a Theory of Interstellar Turbulence. 1: Weak Alfvénic Turbulence, (1984), 612–621, doi: 10.1086/175121.

Stawicki, O., S. P. Gary, & H. Li (2001), Solar Wind Magnetic Fluctuation Spectra: Dispersion versus Damping, J. Geophys. Res., 106(A5), 8273–8281.

Stix, T. H. (1992), Waves in Plasmas, AIP, New York.

Taylor, G. I. (1938), The Spectrum of Turbulence, Proc. R. Soc. London. Ser. A-Mathematical Phys. Sci., 164, 476–490, doi: 10.1098/rspa.1983.0054.

TenBarge, J. M., & G. G. Howes (2012), Evidence of Critical Balance in Kinetic Alfvén Wave Turbulence Simulations, Phys. Plasmas, 19(5), doi: 10.1063/1.3693974.

TenBarge, J. M., & G. G. Howes (2013), Current Sheets and Collisionless Damping in Kinetic Plasma Turbulence, Astrophys. J., 771(2), L27, doi: 10.1088/2041-8205/771/2/L27.

Tessein, J. A., C. W. Smith, B. T. MacBride, W. H. Matthaeus, M. A. Forman, & J. E. Borovsky (2009), Spectral Indices for Multi-Dimensional Interplanetary Turbulence at 1 AU, Astrophys. J., 692(1), 684–693, doi: 10.1088/0004-637X/692/1/684.

Tu, C.-Y., & E. Marsch (1993), A Model of Solar Wind Fluctuations with Two Components: Alfvén Waves and Convective Structures, J. Geophys. Res., 98(A2), 1257, doi: 10.1029/92JA01947.

von Papen, M., & J. Saur (2015), Forward Modeling of Reduced Power Spectra from Three-Dimensional k-Space, Astrophys. J., 806(1), 116, doi: 10.1088/0004-637X/806/1/116.

Wan, M., W. H. Matthaeus, H. Karimabadi, V. Roytershteyn, M. Shay, P. Wu, W. Daughton, B. Loring, & S. C. Chapman (2012), Intermittent Dissipation at Kinetic Scales in Collisionless Plasma Turbulence, Phys. Rev. Lett., 109(19), 1–5, doi: 10.1103/PhysRevLett.109.195001.

Wang, X., C. Tu, J. He, E. Marsch, & L. Wang (2014), the Influence of Intermittency on the Spectral Anisotropy of Solar Wind Turbulence, Astrophys. J., 783(1), L9, doi: 10.1088/2041-8205/783/1/L9.

Wicks, R. T., T. S. Horbury, C. H. K. Chen, & A. A. Schekochihin (2010), Power and Spectral Index Anisotropy of the Entire Inertial Range of Turbulence in the Fast Solar Wind, Mon. Not. R. Astron. Soc. Lett., 407(1), doi: 10.1111/j.1745-3933.2010.00898.x.

Wu, P., S. Perri, K. Osman, M. Wan, W. H. Matthaeus, M. A. Shay, M. L. Goldstein, H. Karimabadi, & S. Chapman (2013), Intermittent Heating in Solar Wind and Kinetic Simulations, Astrophys. J., 763(2), L30, doi: 10.1088/2041-8205/763/2/L30.

Zhdankin, V., D. A. Uzdensky, J. C. Perez, & S. Boldyrev (2013), Statistical Analysis of Current Sheets in Three-Dimensional Magnetohydrodynamic Turbulence, Astrophys. J., 771(2), 124, doi: 10.1088/0004-637X/771/2/124.

Versicherung

Ich versichere, dass ich die von mir vorgelegte Dissertation selbständig angefertigt, die benutzten Quellen und Hilfsmittel vollständig angegeben und die Stellen der Arbeit - einschließlich Tabellen, Karten und Abbildungen -, die anderen Werken im Wortlaut oder dem Sinn nach entnommen sind, in jedem Einzelfall als Entlehnung kenntlich gemacht habe; dass diese Dissertation noch keiner anderen Fakultät oder Universität zur Prüfung vorgelegen hat; dass sie - abgesehen von unten angegebenen Teilpublikationen - noch nicht veröffentlicht worden ist, sowie, dass ich eine solche Veröffentlichung vor Abschluss des Promotionsverfahrens nicht vornehmen werde. Die Bestimmungen der Promotionsordnung sind mir bekannt. Die von mir vorgelegte Dissertation ist von Professor Joachim Saur betreut worden.

Köln, 17. Juli 2017

Anne Schreiner

Teilpublikation

Schreiner, A., & J. Saur (2017), A Model for Dissipation of Solar Wind Magnetic Turbulence By Kinetic Alfvén Waves at Electron Scales: Comparison with Observations, Astrophys. J., 3(2), 1, doi: 10.3847/1538-4357/835/2/133.

Lebenslauf

Persönliche Daten

Name	Anne Rita Schreiner
Geburtsdatum	06.06.1988
Geburtsort	Daun
Nationalität	Deutsch

Schulbildung und Studienverlauf

1994 - 1998	Grundschule Daun
1998 - 2007	Thomas-Morus-Gymnasium Daun
2007 - 2010	Bachelor of Science in Geophysik und Meteorologie, Universität zu Köln
2010 - 2013	Master of Science in Physics of the Earth and Atmosphere, Universität zu Köln
2013 - 2017	Promotion Geophysik, Universität zu Köln